UNIVERSIDAD POLITÉCNICA DE MADRID
Escuela Técnica Superior de Ingenieros de Caminos, Canales y Puertos

COMPUTATIONAL MODELLING OF HYPERELASTIC INCOMPRESSIBLE RESIDUALLY STRESSED CYLINDRICAL TUBES WITH APPLICATION TO INSTABILITIES IN ARTERIAL TISSUES

DOCTORAL THESIS

Submitted for the degree of Doctor by:

DARIEL DESENA GALARZA
Civil and Structural Engineer, M.Sc.

Madrid, 2024

UNIVERSIDAD POLITÉCNICA DE MADRID
Escuela Técnica Superior de Ingenieros de Caminos,
Canales y Puertos

Doctoral Degree in Engineering of Structures, Foundations and Materials

COMPUTATIONAL MODELLING OF HYPERELASTIC INCOMPRESSIBLE RESIDUALLY STRESSED CYLINDRICAL TUBES WITH APPLICATION TO INSTABILITIES IN ARTERIAL TISSUES

DOCTORAL THESIS

Submitted for the degree of Doctor by:

DARIEL DESENA GALARZA
Civil and Structural Engineer, M.Sc.

Under the supervision of:
Dr. JOSE MERODIO
Madrid, 2024

Title: Computational Modelling of Hyperelastic Incompressible Residually Stressed Cylindrical Tubes with Application to Instabilities in Arterial Tissues

Author: Dariel Desena Galarza

Doctoral Programme: Engineering of Structures, Foundations and Materials

Thesis Supervision:

Dr. José Merodio, Professor, Universidad Politécnica de Madrid (Supervisor)

External Reviewers:

Thesis Defense Committee:

Thesis Defense Date:

To my lovely family,

They are the engine that drives me forward.

Acknowledgement

This thesis document is the result of several years of study and efforts, with its downs and upturns.

I would like to thank my supervisor, Professor José Merodio for sharing his knowledge and vast experience with me, for his guidance and constant push forward in the right direction to allow this work is finished satisfactorily, I will always be soundly grateful to him. To my colleague Dr. Hamidreza Dehghani, for providing along with Prof. José Merodio a good collaboration environment during the beginning of my doctoral studies and for sharing his knowledge with me at that early stage.

I also want to express my deep gratefulness to my family for his unconditional support. To my parents, for believing in my capabilities anytime and from the beginning of this journey, supporting me in all the possible ways. To my wife and son, for their unconditional love and support, but more than anything for his patience because of the many stolen hours. They are the engine that drives me. Finally, I thank God for this marvelous opportunity he allows me to climb one more step in my personal and professional career.

Abstract

In this document, the mechanical modelling of a hyperelastic residually stressed thick-walled circular cylindrical tube under inflation and extension is performed from a numerical standpoint. The constitutive relation is derived for residually stressed solids using an invariant-based free energy approach. A three-dimensional residual stress field is introduced in the argument of the strain energy density function and compared with results from a planar residual stress field. This formulation is incorporated into a numerical procedure using the Finite Element Method (FEM), with the use of a nonlinear solution scheme via the modified Riks method in order to capture bifurcation and post-bifurcation of the tube. The FE implementation of the proposed formulation is carried out in the general-purpose code ABAQUS by means of user-defined capabilities. As the residually stressed hyperelastic incompressible material is not a built-in material a user material subroutine defining the Jacobian matrix and the deviatoric stress tensor is used and implemented for hybrid solid elements. A comprehensive analysis of the structural performance of the tube is conducted with special focus on the effect of the residual stresses on the bifurcation behavior. Results are analyzed mainly in the context of aneurysms formation and propagation in arterial wall tissues, although it has other applications such as in the context of venous tortuosity. Bulging and bending modes are obtained, and post-bifurcation is also captured. Results suggest that the onset and location of the bulge along the axis of the tube depend mainly on the axial stretch and on the residual stress field. Computations also show that for sufficiently large values of axial stretch the onset of bifurcation is bulging while for small values of axial stretch the onset of bifurcation is bending. Post-bifurcation behavior of this latter case gives rise to bulges on one side of the tube, which is an irregular shape that appears in the advancement of abdominal aortic aneurysms (AAA).

Resumen

En este documento, se realiza el modelado mecánico desde un punto de vista numérico de un tubo cilíndrico circular con tensiones residuales de espesor finito y material hiperelástico incompresible sometido a presión interna y estiramiento axial. La relación constitutiva se plantea para sólidos con tensiones residuales mediante una función de energía basada en invariantes. Un campo de tensiones residuales tridimensionales se introduce en el argumento de la función de energía de deformación y los resultados obtenidos son comparados con los correspondientes a un tensor de tensiones residuales bidimensional. Esta formulación se incorpora en un procedimiento numérico basado en el Método de los Elementos Finitos (MEF), considerando un procedimiento de análisis no lineal como lo es el método modificado de Riks, para poder capturar tanto la bifurcación como el comportamiento pos-bifurcación del tubo. La formulación propuesta es implementada en el software de elementos finitos ABAQUS, explotando sus capacidades en cuanto al uso de herramientas que pueden ser definidas por el propio usuario. Debido a que no hay alguna formulación integrada para un material hiperelástico incompresible con tensiones residuales, se utiliza una subrutina en la que se define el tensor de tensiones y la matriz Jacobiana implementada para elementos sólidos de formulación híbrida. Se realiza un análisis cualitativo del comportamiento estructural del tubo con especial énfasis en el efecto de las tensiones residuales en el comportamiento durante la bifurcación. Los resultados se interpretan en el contexto de la formación de aneurismas y su propagación los tejidos de las paredes arteriales, aunque también son aplicables a problemas relacionados con la tortuosidad venosa. Se consigue capturar la bifurcación por abombamiento y por flexión del tubo, así como también, el comportamiento pos-bifurcación. Los resultados sugieren que el inicio del abombamiento y su localización a lo largo del eje del tubo dependen principalmente del estiramiento axial y del campo de tensiones residuales aplicado. Los cálculos muestran que para valores relativamente grandes de estiramiento axial el inicio de la bifurcación está dado por un abombamiento del tubo, mientras que para valores suficientemente pequeños el inicio de la bifurcación está dado por un modo de flexión. En el comportamiento pos-bifurcación de este modo aparecen abombamientos en un lateral del tubo, formando una geometría irregular que aparece durante la progresión de aneurismas aórticos abdominales (AAA).

Table of Contents

List of Figures

List of Tables

Abbreviations and Acronyms

UPM	Universidad Politécnica de Madrid
FEM	Finite Element Method
AAA	Abdominal Aortic Aneurysms
PDE	Partial Differential Equation

1. Introduction

Mechanical modelling of materials from a numerical approach is useful for gaining greater insight into the behavior of a wide variety of material bodies with different geometries and loading conditions. Often, the application of constitutive theories to study a specific problem from a pure analytical approach involves the assumption of simplified states of the material body, as relating to geometries, acting loads and boundary conditions, to be able to demonstrate the capabilities of the analytical framework from a reasonably simplified scheme. The application of such analytical frameworks under much more complicated conditions many times could involve complex systems of partial differential equations (PDE) that its solution could be very time consuming involving sophisticated complex mathematical machinery.

One of the objectives of computational mechanics is to solve complex engineering and physics research problems related to material modelling and its structural mechanical behavior, through numerical simulations. Complex systems of PDEs can be solved by using numerical methods that solve equivalent systems of algebraic equations conducting to approximated solutions ([1], [2]). This is achieved by implementing mathematical models within numerical algorithms to obtain approximated but valid solutions. Nowadays, the method widely used for solving engineering and physics problems from a numerical approach is the Finite Element Method (FEM). It can be applied in a large variety of problems, such as in the field of structural analysis, fluid flow, heat transfer or electromagnetic potential. It is also suitable for studying Multiphysics interactions, such as thermo-mechanical problems and fluid-structure interactions [1]. It is a widely known and used method, so it is out of the scope of this work to go into the fundamentals of the method.

In this work a Boundary Value Problem is analyzed by using the FEM approach. An extended and then inflated circular cylindrical tube of hyperelastic incompressible material is modelled and qualitatively analyzed in the context of instabilities related to Arteries. The constitutive modelling is based on an invariant based strain energy potential for an incompressible isotropic material, which has been used in several investigations to interpret the results in terms of the mechanical behavior of arterial tissues (see for example [3]-[9]). Residual stresses, present in Arteries [6], modify their mechanical response, thus particular fields are introduced in the argument of the strain energy potential to account for its effects ([10], [11]).

It is known that under non-physiological conditions, arteries can develop localized bulging with a corresponding wall weakening, which has been analyzed in the context of Aneurysm formation and propagation in arterial walls ([3], [12]-[21]). It is also known that a bending buckling mode is possible prior to bulging under certain boundary conditions ([3], [18], [21]) and axial stretch. In this work both bifurcation modes are captured in several numerical simulations carried out in the widely used Finite Element (FE) commercial code Abaqus. The results are then analyzed in the context of Abdominal Aortic Aneurysms (AAA) and its post-bifurcation behavior.

The document is organized as follows. In this chapter 1 the motivation, objectives and methodology of the work are presented. Chapter 2 outlines a theoretical framework on the analytical analysis of circular cylindrical tubes made of incompressible hyperelastic material. In chapter 3 general applicable characteristics for the various implemented numerical models are described, such as the constitutive model and aspects of the computational models. In chapter 4, numerical results are presented for models considering a planar residual stress field, whereas in chapter 5 numerical results are presented for models in which the axial residual stress effect is incorporated. Chapter 6 shows further discussion and concluding remarks.

1.1. Motivation

Mechanics is a science aimed at describing the motion of a system or body subjected to certain forces. This is accomplished by determining the kinematics and the kinetics of the massed body or system. Biomechanics is a branch of Mechanics that consists of applying its laws and fundamentals to characterize the response of biological systems and materials subjected to forces and certain boundary conditions. According to [22], the earliest literature on this subject was probably written by Aristotle in his book "On the Parts of Animals", in which a description of internal organs is presented; and by Nei Jing in "Internal Classic" book, in which the concept of blood circulation is discussed. However, the development of Biomechanics as a science has been stimulated by medical and mathematical contributions.

A very important contribution was made by Galileo Galilei's research, who established a first method to determine the pulse rate in humans by using isochronous pendulums and relating its length when synchronized with the beat. This method of applying Mathematics to characterize the functioning of vital processes would boost other researchers to work in this field. William Harvey settled the theory of blood circulation from a theoretical approach after measuring the capacity of the heart and showing that the blood can only leave the ventricle in one direction. After this findings, Marcello Malpighi experimentally proved William Harvey's theory by discovering the capillaries which connect the Arteriole with the Veins, necessary network for blood circulation across the body.

Some other physicists and mathematicians like Giovanni A. Borelli and Robert Hooke also made important contributions on the study of living systems and its vital processes. Borelli successfully clarified the muscular movements and body dynamics, while R. Hooke gave us the relation between force and unitary deformation of elastic bodies and established the word Cell in biology [22]. Even though Newton did not publish works in the field of Biomechanics, its calculus was certainly fundamental for Mechanics and thus, Biomechanics. He settled the foundation of Classical Mechanics by his “Principia Mathematica”, his laws of motion and the constitutive equation for a viscous fluid. Regarding Arteries, Euler wrote on the propagation of pulse waves in 1775. Many other physicists and mathematicians accomplished important contributions in Mechanics and Biology. It would be a very extensive list, and it is not the aim of this work to do a review of the history of Biomechanics. The reader is referred to [22] for a more extensive and chronological description of the findings made on this context.

As it can be inferred from the brief ideas exposed in the previous paragraphs, from remote times humans have questioned the function of the human body and other living systems. These questions have allowed researchers to get fundamental findings which allow to explain the expected behavior of some vital body processes and so, its abnormal function. Many of these findings have been made from a classical physics investigation approach. These have advanced medicine in the context of diagnosis, surgery, prosthesis and have promoted the well-being of humanity regarding health [22].

However, many human biological processes still need to be better understood from a biomechanical and mechanobiological perspective, in order to precisely define the mechanical response of soft tissues when they function outside of typical homeostatic mechanisms, as well as their role in disease progression. Many important contributions to these fields have been made on recent years (see to name a few ([3], [4], [6], [17]-[19], [23]-[27]). On this context, a health issue regarding to arteries whose mechanical conditions is a topic that needs yet to be deeply studied is the development of Abdominal Aortic Aneurysms (AAA). An Aneurysm could be defined as an abnormal enlarged area localized in a blood vessel, frequently in the Aorta. The Aorta is the main Artery in the human body that carries blood from the heart to the abdominal area, and it is the largest blood vessel in the human body [28]. It is composed of three layers: the Intima, the Media and the Adventitia, with interfaces of elastic membranes, as can be seen from the figures below.

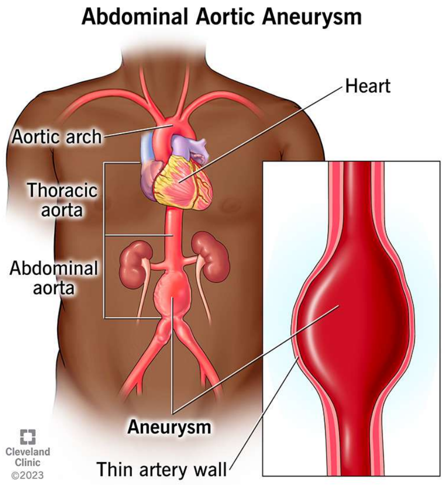

Figure 1.1: Schematic Representation of an Abdominal Aortic Aneurysm [29].

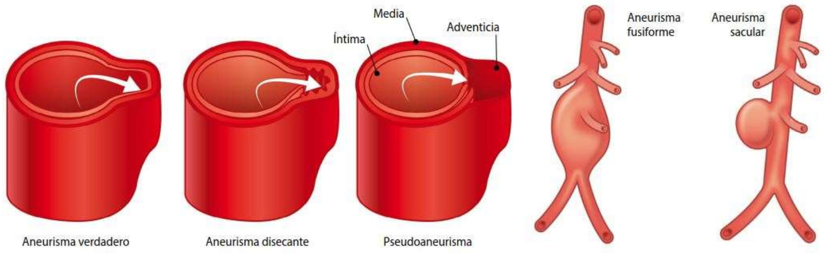

Figure 1.2: Scheme of Aneurysm types and shapes [28].

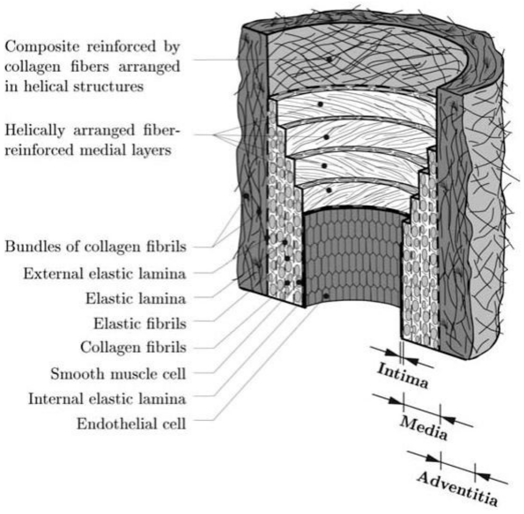

Figure 1.3: Artery wall structure showing its major components (see [30]).

It is many times asymptomatic, and its treatment is mainly aimed at controlling the growth rate. If an Aneurysm bursts and ruptures, the internal bleeding is life-threatening, and it shall be surgery as soon as possible. From a clinical standpoint, there are several conditions that indicate a person is more at risk of developing an Aortic Aneurysm [31]:

- To smoke
- To be male, aged 65 or more
- To have high blood pressure or high levels of cholesterol
- To have an artery disease as Atherosclerosis
- To have had a close relative who had developed an Aortic Aneurysm
- To have a condition, as the Marfan Syndrome

It is believed that the degradation of elastin triggers the formation of an aneurysm ([32]-[36]). Under this circumstance, the stress that is to be carried by collagen increases and collagen turnover is upregulated. Smooths muscle cell degradation may also play an important role. Stress is expected to be a homoeostatic target of the normal vessel. However, an aneurysm has a highly degenerative wall and the biological mechanisms to remodel towards a homoeostatic stress are heavily impaired. It then results in a continuous (pathological) remodeling of the structural proteins in the wall. High blood pressure (which is directly linked to wall stress) is known to be a risk factor of the formation of aneurysms, as mentioned before. However, there is no evidence, based on the best effort done for bibliographical research, relating high stress in the wall and an aneurysm. In this work the stress states at bifurcation that can trigger the formation of aneurysms are treated mainly from a theoretical point of view.

Instabilities from geometric signature have been analyzed in the last two decades especially due to the influence of such phenomena in the formation and propagation of aneurysms in arterial walls. Bulging and bending instabilities of inflated and extended tubes have been related to the formation and propagation of aneurysms (see for instance, [3], [4], [9], [13], [14], [18], [20], [21], [37] and the references therein). The formation of aneurysms involves several biomechanical factors including age, biochemical reactions, heterogeneity of the material, anisotropy, among many others, apart from the geometrical characteristics of the vessels. But the mechanical modulation of this mechanism plays a role that needs to be well understood to include, then, the biochemical processes.

Experimentally, different investigations in the literature have reported that when a non-loaded artery is cut along its radius it forms an open sector, which means that the artery is not unstressed in the absence of applied loads (see [6], [11], [22], [38], [39] and references therein). Residual stresses play an important role in homoeostasis which is a biological process that tends to conserve key regulated variables near different preferred values maintained by living systems. Mechanical homoeostasis exists at different levels including cellular and tissue levels in the cardiovascular system and is critical for both vessel maintenance and adaptations to disease progression, responses to injury, etc. [32]. It is well known that residual stresses in arterial walls arise due to growth and development [39].

Very recently, residual stresses have been included in different analyses using an invariant-based free energy approach. Such constitutive formulations can be seen in [7] and [40]. Within this framework, the instability of cylindrical tubes under torsion, which gives rise to helical buckling, was analyzed in [15], [41]. That formulation is used in this work, and it will be described in further sections. The formulation is employed to study bulging and bending bifurcation as well as post-bifurcation of tubes under inflation and extension.

Bifurcation analytical results provide great insight into the physical interpretation of the problem under study. For the problem at hand, several studies in this direction have indicated that the modes of bifurcation are the so-called prismatic mode, axisymmetric (bulging) mode, and composite mode ([3], [17], [40]). However, analytical approaches require sophisticated mathematical machinery and in addition analytical solutions are available only for relatively simple cases, which highlights the need to consider alternatives to these analytical formulations. The Finite Element Method has been exploited in several studies such as ([13], [14], [17], [21], [38], [42]). It is a framework that opens new perspectives not only in scientific works but also in professional practice, which is also one of the main goals of this work. Hopefully, this numerical approach shall be the base for analyzing more complete models representing the artery, including artery layers, its interaction (contact interphases), different distributions of residual stresses, the collagen fibers strain stiffening effect, hemodynamic, etc.

1.2. Methodology

The Finite Element Method is exploited to analyze the behavior of an axially stretched thick-walled circular cylindrical tube subjected to internal pressure including the effect of a two and three-dimensional residual stress fields. The general-purpose Finite Element software package Abaqus is used. The tube material is modelled as a hyperelastic fully incompressible material. This means that in a statement of a balance of external and internal energy, a strain energy potential can be considered for the work done (there is no dissipation) by the stresses generated during the deformation of the tube [6].

Therefore, it is used a strain energy density function W per unit volume of reference configuration that depends on the deformation gradient F, being W a scalar function indifferent to rigid body rotations, both, in the deformed and in the reference configurations. This prompts that W is objective and that the material is isotropic. Regarding the residual stresses (considering the nature of residual stresses as defined in [43]), they are included by defining a residual stress tensor $\boldsymbol{\sigma}_0$ included in the argument of W in the reference configuration of the tube. As the stresses can be then determined from W, the constitutive relation of the hyperelastic material is defined.

The constitutive law is introduced by exploiting the User Material Subroutine (UMAT) tool, as the constitutive relation including residual stresses is not a built-in material in Abaqus. This Abaqus tool gives the user the flexibility of defining any constitutive law corresponding to user-defined materials. This is implemented by establishing the relation between stress and strain and explicitly defining the Jacobian matrix for the material, making use of the FORTRAN programming language. The definition of the finite element model is done by writing down a Python based coding in an Abaqus Input File, in which the following variables are parametrized:

- Model geometry (length, wall thickness, cross sectional diameter)
- Model meshing (radial, azimuthal and longitudinal number of elements)
- Strength for the residual stress components
- Material shear modulus and internal pressure
- Axial stretch

For the elements, the hybrid incompressible solid element formulation is employed to avoid locking problems [44]. The analysis of the model is done by using the Modified-Riks Method, by which the evolution of the deformation of the tube can be followed as the internal pressure is incrementally applied. The magnitude of the applied pressure and the deformation are represented by the Load Proportionality Factor and the Arc-Length coefficients. This numerical procedure is implemented within Abaqus Standard, and it is suitable for nonlinear finite deformation problems, allowing to avoid snapping issues. The bifurcation modes are analyzed from an incremental displacement field approach [17]. More details on the numerical methodology are given in sections 3.4, 4.3 and 5.3.

1.3. Objectives

The main objective of this thesis work is to qualitatively characterize the mechanical behavior of hyperelastic incompressible residually stressed circular cylindrical tubes under axial stretch and internal pressure, in the context of soft biological tissues, by employing a nonlinear numerical approach based in the Finite Element Method. The following objectives are stated for pursuing the previously mentioned:

- To study the instability modes for thick-walled circular cylindrical tubes subjected to axial pre-stretch and internal pressure, including the effect of residual stresses in the constitutive law of the material.
- To employ a numerical methodology capable of capturing the bifurcation and post-bifurcation behavior of the tubes under the mentioned conditions.
- To characterize the expected bifurcation mode as a function of the applied axial pre-stretch.
- To qualitatively describe the post-bifurcation behavior of the tubes.
- To identify the internal stress state for the tubes at the occurrence of the captured bifurcation mode.

2. Theoretical Framework on Residual Stress and The Bifurcation of Extended and Inflated Circular Cylindrical Membranes.

2.1. Modelling of Residual Stresses in Elastic Materials

A residual stress is a stress field acting on a material body in the absence of external loads ([43], [45]). Characterizing the behavior of structural elements subjected to residual stresses is of great importance due to the influence they could have on its structural response. For hot-rolled steel profiles subjected to compression loads, the buckling failure could be reached before predicted if the additional compression due to residual stresses are not considered in the analysis. Even though for that case residual stresses could be relatively small, their consideration is important when it becomes necessary to include second order effects in the analysis of the member or structure.

Similarly, residual stresses influence the biomechanical behavior of soft biological tissues (see for instance [10], [45] and [46]). For example, it is known that residual stresses regulate that the azimuthal stress distribution along the thickness of the artery walls be close to uniform at normal physiological blood pressure ([6], [47]). This prompts the study of the behavior of soft biological tissues should not be done excluding the effect of residual stresses.

Y. C. Fung questioned the “zero-stress state” of blood vessels as a necessary question to be answered to derive a constitutive relation for soft tissues. This reasoning guided his experimental work in which he characterized the “in vivo”, "no-load" and "zero-stress states" for an artery. The "in vivo" state represented a fixed rat's artery at normal physiological blood pressure, the "no-load" condition represented a non-extended nor inflated excised section of the same artery and the "zero-stress" state represented a small excise of the previous section, which was cut transversally as a ring and then, radially [22].

It has been demonstrated that for the radial cuts the ring springs open, showing that even though no loads are applied the ring is stressed and that the stresses are (assumed) then relieved ([22], [48], [49]). After the radial cut the ring forms an open sector that is characterized by its opening angle, defined as the angle between two lines drawn from the middle of the open sector inner wall to the tips (it should be noted that different definitions for the opening angle are given in the literature, see for example [6], [22] and [49]. The residual stresses present are estimated by the equivalent stresses computed to re-form (close) the intact ring to reach the "no-load" configuration. Several researchers have studied the distribution of the residual stresses from an experimental and analytical approach by using this opening angle method, which gives estimates but adequate insight into the residual stresses present in blood vessels ([11], [22], [30], [38], [45], [46]). For example, it is known that in the circumferential direction, compressive residual stress acts in the intima – media region and tensile residual stress acts in the adventitia region. However, a detailed understanding of the influence of residual stress in the artery mechanics is yet to be developed [47].

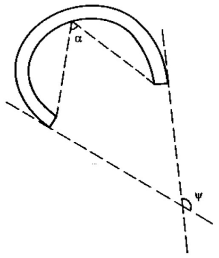

Figure 2.1: Opening angle representation for a blood vessel sector [22].

Several researchers have studied how these residual stresses affect the elastic response of materials (see, for instance [6], [7], [11], [15], [39], [40], [42], [43], [45]-[47], and [50]-[53]). An elastic material for which its properties can be characterized in terms of a strain energy function defined per unit volume in the reference configuration, is said to be a Hyperelastic material [6]. There are several formulations for characterization of hyperelastic materials, which have been exploited for researching on a wide range of applications ([8], [37], [54]-[65]). For an incompressible material the nominal stress tensor $\boldsymbol{S}$ is defined as [6] [40]:

$$\boldsymbol{S} = \frac{\partial W}{\partial \boldsymbol{F}} - p\boldsymbol{F}^{-1} \quad det\boldsymbol{F} = 1 \tag{2-1}$$

Where p is a Lagrange multiplier associated with the incompressibility condition, referred to as an arbitrary hydrostatic pressure. It is recalled the relation between the nominal and the Cauchy stress tensor, to define the latter in terms of the strain energy function ([6], [47]):

$$J\boldsymbol{\sigma} = \boldsymbol{FS} = J^{-1}\boldsymbol{F}\left(\frac{\partial W}{\partial \boldsymbol{F}} - p\boldsymbol{F}^{-1}\right) \tag{2-2}$$

$$\boldsymbol{\sigma} = \boldsymbol{F}\frac{\partial W}{\partial \boldsymbol{F}} - p\boldsymbol{I} \tag{2-3}$$

When a reference configuration $\boldsymbol{B_r}$ is stress free (in an unconstrained) material, then, its strain energy in that natural configuration is described by equation (2-4) [47]. If the stress does not vanish in that configuration $\boldsymbol{B_r}$, the material is said to be residually stressed. That state would be equivalent to the unloaded state mentioned in previous paragraphs. As no surface tractions exists in that state, the residual stress must vanish on the boundary of the body ∂B_r, meaning that these stresses are inhomogeneous in nature and thus, geometry dependent.

$$W(\boldsymbol{I}) = 0 \quad \frac{\partial W}{\partial \boldsymbol{F}}(\boldsymbol{I}) = \boldsymbol{O} \tag{2-4}$$

If the strain energy function is measured from the residually stressed configuration $\boldsymbol{B_r}$, then $W(\boldsymbol{F} = \boldsymbol{I}) = 0$ is satisfied. As the reference configuration is already stressed with a residual stress tensor $\boldsymbol{\sigma_0}$, and the deformation is measured from $\boldsymbol{B_r}$ there is no distinction between the Cauchy and the Nominal stress tensors $\boldsymbol{\sigma}$ and $\boldsymbol{S}$, so $\boldsymbol{S} = \boldsymbol{\sigma} = \boldsymbol{\sigma_0}$. It is considered that there are not intrinsic couple stresses, so $\boldsymbol{\sigma_0}$ is symmetric ($\boldsymbol{\sigma_0}^T = \boldsymbol{\sigma_0}$). The residual stress must satisfy the equilibrium condition in the reference configuration $\boldsymbol{B_r}$ and the boundary condition:

$$Div\, \boldsymbol{\sigma_0} = \boldsymbol{0} \tag{2-5}$$

$$\boldsymbol{\sigma_0 N} = 0 \; on \; \partial B_r \tag{2-6}$$

Here, $\boldsymbol{N}$ is the unit outward vector normal to the boundary ∂B_r. The previous equations implies that there are no surface tractions nor body forces. These conditions validate the non-uniform distribution of the residual stress, which means inhomogeneous elastic response of the material. In section 3.2.2 the specific constitutive framework to be considered in this work is exposed.

2.2. Bifurcation of Circular Cylindrical Tubes Subjected to Axial Extension and Internal Pressure

The bifurcation conditions for circular cylindrical membrane tubes under axial loading and internal inflation pressure have been studied from both analytical and numerical approaches. Analytical approaches are fundamental to understanding the mechanisms that govern the structural instabilities of this kind of problems. Although they imply more complex mathematical machinery (than numerical methods), the results and insights obtained from the development of such analytical methods constitute the basis for numerical results validation. The boundary for passing from an analytical to a numerical method seems to be when the problem at hand includes the interaction of so many variables that the solution of the resulting system of PDEs becomes impractical or not possible to be derived.

2.2.1. Geometry and Deformation Description

In the reference configuration of a circular cylindrical membrane tube $\boldsymbol{B_r}$, the geometry in cylindrical coordinates (R, Θ, Z) is defined as:

$$R = \frac{D}{2}, \quad 0 \leq \Theta \leq 2\pi, \quad 0 \leq Z \leq L, \tag{2-7}$$

where D is the tube diameter. For every material point of the body in the reference configuration, the position vector can be written as:

$$\boldsymbol{X} = R\boldsymbol{E_R}(\Theta) + Z\boldsymbol{E_Z} \tag{2-8}$$

$\boldsymbol{E_R}$ and $\boldsymbol{E_Z}$ are the unit vectors in R and Z directions. On the other hand, in the deformed configuration $\boldsymbol{B}$, the geometry and position vector of each point in the cylindrical tube are:

$$r = \frac{d}{2}, \quad 0 \leq \theta \leq 2\pi, \quad 0 \leq z \leq l \tag{2-9}$$

$$\boldsymbol{x} = r\boldsymbol{e}_r(\theta) + z\boldsymbol{e}_z \tag{2-10}$$

Similarly, $\boldsymbol{e}_r$ and $\boldsymbol{e}_z$ are unit vectors in the radial and axial directions, respectively, and d is the tube diameter in the deformed configuration. It is assumed that the tube remains a circular cylinder after the deformation takes place. It is recalled that the deformation of a material point A at position X of the body in the reference configuration $\boldsymbol{B_r}$ is defined by the response to the deformation at time t of a small neighborhood of the point [61]. The change of local geometry in the neighborhood of X as it moves to **x**, being **x** the position of point A in the deformed configuration $\boldsymbol{B}$, is represented by the tensor **F**, which is the linear mapping of each line element dX radiating in direction **N** from the position X in the reference configuration $\boldsymbol{B_r}$ into the line element d**x** radiating in direction **n** from the position **x** in the deformed configuration $\boldsymbol{B}$.

If the position of a point in the deformed configuration is $\boldsymbol{x} = \chi(\boldsymbol{X})$ (here, the attention is focused on quasi-static deformations), then by the previous definition, the deformation gradient **F** is ([5], [6], [61]):

$$\boldsymbol{F} = \left[\frac{\partial\, \chi(\boldsymbol{X})}{\partial \boldsymbol{X}}\right] = Grad\; \chi(\boldsymbol{X}) = Grad\; \boldsymbol{x} \tag{2-11}$$

For the cylindrical tube the deformation gradient **F** is symmetric [6] and has components diag$(\lambda_r, \lambda_\theta, \lambda_z)$, where $\lambda_\theta = {}^{r}/_{R}$ is the azimuthal principal stretch and $\lambda_z = {}^{l}/_{L}$ is the axial stretch. As the material is incompressible, the radial principal stretch can be defined as a function of the other two principal stretches as $\lambda_r = {\lambda_\theta}^{-1}{\lambda_z}^{-1}$.

2.2.2. Material Model

Several material models for artery walls have been developed and implemented in the literature, for a sound study and comparison between them refer to [30]. For modelling of extended and inflated circular cylindrical tubes in the context of soft tissues, a hyperelastic behavior of the material is typically considered. This imposes the need of a strain energy function W to derive the relation between stress and strain. For a homogeneous incompressible nonlinearly elastic isotropic material, the strain energy function depends only on the two independent invariants of $\boldsymbol{C}$ (or $\boldsymbol{B}$), which are the following ($I_3 = \det(\boldsymbol{F}) = 1$):

$$\begin{gathered} I_1 = tr(\boldsymbol{C}) = {\lambda_1}^2 + {\lambda_2}^2 + {\lambda_3}^2 \\ I_2 = \frac{1}{2}[(tr\boldsymbol{C})^2 - tr(\boldsymbol{C}^2)] = {\lambda_1}^2{\lambda_2}^2 + {\lambda_1}^2{\lambda_3}^2 + {\lambda_2}^2{\lambda_3}^2 \end{gathered} \tag{2-12}$$

$\boldsymbol{C} = \boldsymbol{F}^T\boldsymbol{F}$ is the right Cauchy-Green deformation tensor, $\boldsymbol{F}$ is the deformation gradient tensor, tr means the trace of a second order tensor and λ_i are the principal stretches, that in cylindrical coordinates are equivalent to $\lambda_1 = \lambda_r$, $\lambda_2 = \lambda_\theta$ and $\lambda_3 = \lambda_z$. The artery wall can be modelled as a composite material formed by a solid matrix and (collagenous) fibers reinforcement. Since the effect due to the fibers is beyond the scope of the present work, we embraced the simplified Neo-Hookean strain energy function given below [30]:

$$W = \frac{\mu}{2}(I_1 - 3) \tag{2-13}$$

This form of the strain energy provides adequate approximation for this context, as upturns of the stress-strain behavior (as strain stiffening) is not expected because it is mainly responsibility of the collagen fibers collaboration during deformation ([17], [26], [30]). In the literature, various authors have considered this model in this context to represent the behavior of the solid matrix of the artery walls, producing good insights in this research field (see [18], [23], [26], [30], [40], [41] and [65]).

The principal Cauchy stresses (in components form) can then be written as:

$$\sigma_{ii} = \lambda_i \frac{\partial W}{\partial \lambda_i} + q \tag{2-14}$$

Where $i = r, \theta, z$, q represents the arbitrary pressure related to the incompressibility constraint and $W = W(\lambda_r, \lambda_\theta, \lambda_z)$. For a membrane $\sigma_{rr} = 0$, so the remaining principal components of Cauchy stress are defined as:

$$\begin{aligned} \sigma_{\theta\theta} &= \lambda_\theta \frac{\partial \widehat{W}}{\partial \lambda_\theta} \\ \sigma_{zz} &= \lambda_z \frac{\partial \widehat{W}}{\partial \lambda_z} \end{aligned} \tag{2-15}$$

Where $\widehat{W}(\lambda_\theta, \lambda_z) = W({\lambda_\theta}^{-1}{\lambda_z}^{-1}, \lambda_\theta, \lambda_z)$ is introduced. By using the membrane approximation, the inflation pressure of the membrane tube P may be defined as ([3], [6], [17]):

$$p = \frac{H\widehat{W}_{\lambda_\theta}}{R\lambda_\theta \lambda_z} \tag{2-16}$$

Where H is the undeformed thickness of the membrane and $\widehat{W}_{\lambda_\theta}$ denotes ${\partial \widehat{W}}/{\partial \lambda_\theta}$. Similar notation is used such as $\widehat{W}_{\lambda_z}, \widehat{W}_{\lambda_\theta \lambda_\theta}$, with equal meaning as defined previously.

2.2.3. Bifurcation of Thin-Walled Tubes

In the context of instabilities of thin-walled tubes, the bifurcation conditions for the possible modes on cylindrical tubes under inflation pressure and axial loading are analyzed in detail in [3] and [17]. The theoretical framework followed in [3] is based on the incremental equations' method, a theory initially published by Biot [66]. A less time-consuming approach is presented in [17], derived from the equilibrium of infinitesimal volume elements.

The bifurcation conditions, and specifically for bulging bifurcation have been studied by several authors for tubes under different geometry and boundary conditions, including from numerical approaches for thick-walled tubes (see, for instance [3], [13], [17], [27], [67]-[73]). For the present work, the bifurcation conditions derived in [17] will be followed. It constitutes a different approach from that presented in [3] but drives to the same result scenarios ([17]).

For the cylindrical coordinates system, the incremental displacement field is of the form [17]:

$$\delta \boldsymbol{u} = \delta u_r(\theta,z)\boldsymbol{e}_r + \delta u_\theta(\theta,z)\boldsymbol{e}_\theta + \delta u_z(\theta,z)\boldsymbol{e}_z \qquad (2\text{-}17)$$

Where δu_r, δu_θ and δu_z are the incremental displacements with respect to the deformed or current configuration of the body in equilibrium. From the definition of displacement increments, the bifurcation modes are described as follows.

Prismatic mode. For this mode the cylinder remains prismatic, but the cross sections become non-circular. The incremental displacement is assumed to be independent of z.

$$\delta \boldsymbol{u} = \delta u_r(\theta)\boldsymbol{e}_r + \delta u_\theta(\theta)\boldsymbol{e}_\theta \tag{2-18}$$

By establishing equilibrium in an infinitesimal volume element and after mathematical manipulations (for details see [17]), the following equilibrium equation can be written:

$$\widehat{W}_{\lambda_\theta \lambda_\theta} \frac{\partial \delta \lambda_\theta}{\partial \theta} = 0 \tag{2-19}$$

The condition can be true if there is no variation of the incremental azimuthal stretch ($\delta\lambda_\theta$ is uniform) or, if:

$$\widehat{W}_{\lambda_\theta \lambda_\theta} = 0 \tag{2-20}$$

An important result regarding this condition is given by means of equation (2-16). The critical pressure values can be derived as [17]:

$$\mathrm{p} = \frac{H\widehat{W}_{\lambda_\theta \lambda_\theta}}{R\lambda_z} \tag{2-21}$$

Bulging Mode. Under this bifurcation mode the cylindrical tube remains circular but at cross-section it bulges [3]. The incremental displacements are assumed to be independent of θ. Under this condition, the displacement is axisymmetric, which can be written as:

$$\delta \boldsymbol{u} = \delta u_r(z)\boldsymbol{e}_r + \delta u_z(z)\boldsymbol{e}_z \tag{2-22}$$

From equilibrium in the axial and radial directions for an infinitesimal volume element, the following equations are derived [17]:

$$\frac{\partial}{\partial z}(\delta(\sigma_{zz}hr))d\theta dz - prd\theta dz\frac{\partial \delta u_r}{\partial z} = 0 \tag{2-23}$$

$$\delta(pr)d\theta dz - \delta(\sigma_{\theta\theta}h)d\theta dz + \frac{\partial}{\partial z}\left(\sigma_{zz}hrd\theta\frac{\partial \delta u_r}{\partial z}\right)dz = 0 \tag{2-24}$$

After several mathematical manipulations and considering inflation pressure in the tube, (according to [17]) for a tube of infinite length the bulging criterion is:

$$f(\widehat{W}, \lambda_\theta, \lambda_z) = 0 = {\lambda_z}^2\widehat{W}_{\lambda_z\lambda_z}\left({\lambda_\theta}^2\widehat{W}_{\lambda_\theta\lambda_\theta} - \lambda_\theta\widehat{W}_{\lambda_\theta}\right) - (\lambda_\theta\lambda_z\widehat{W}_{\lambda_\theta\lambda_z} - \lambda_\theta\widehat{W}_{\lambda_\theta})^2 \tag{2-25}$$

From this condition it is concluded that turning points of pressure (where it reaches a maximum, defined by (2-16) and (2-21)) obey $f \leq 0$ because the left term of the right hand side of the equation is zero. Equation (2-25) is also $f \leq 0$ for turning points of the axial load:

$$\widehat{W}_{\lambda_z\lambda_z} = 0 \tag{2-26}$$

It follows that the initiation of bulging bifurcation is prior to the pressure turning point [17].

Bending Mode. The combination of the prismatic and bulging modes can be interpreted in terms of bending [3]. Bending is more likely to occur in long tubes than in short tubes. Understanding this type of bifurcation behavior is of great importance because bending bifurcation may lead to the development of tortuous shapes of the blood vessels, which could be associated with hypertension, diabetes, retinopathy, and axial extension reduction ([74]-[77]). When the artery shows significant bending, saccular aneurysms seem to appear ([21], [78]). The numerical analysis of this bifurcation mode will be guided by the analytical solution for the membrane case with no residual stress.

For an axial stretch to be maintained during the tube inflation, the axial load N > 0, which means that both ends of the cylinder should be fixed [3]. If N = 0 then axial shortening accompanies the inflation, as $\lambda_\theta {\lambda_z}^2 = 1$, being $\lambda_\theta > 1$ (inflation) and axial stretch necessarily $\lambda_z < 1$ [79]. Now, if the cylinder axis is subjected to radial displacements $\delta {u_r}^0$ (because, for example, due to applied residual stress) the moment equilibrium $\mathcal{M}$ is written as [17]:

$$\mathcal{M} \;=\; N\delta {u_r}^0 - p\pi r^2 \delta {u_r}^0 \tag{2-27}$$

By using $N = 2\pi r h \sigma_{zz}$ and $p = \frac{\sigma_{\theta\theta} h}{r}$, equation (2-27) can express stable equilibrium as:

$$\mathcal{M} \;=\; \sigma_{\theta\theta} \;-\; 2\sigma_{zz} = 0 \tag{2-28}$$

Then, unstable configurations obey $\mathcal{M} > 0$, as it is detailed in [17] and was also given in [3].

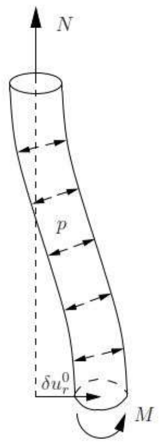

Figure 2.2: Balance of forces for an inflated and extended membrane tube ([17]).

3. Basis of the Computational Methodology for Non-Linear Analysis of Extended and Inflated Circular Cylindrical Tubes with Residual Stresses

3.1. Introduction

As has been exposed in previous sections, the inflation and extension of circular cylindrical tubes has been studied in the context of mechanics of arteries from a theoretical approach. Specifically, analytical equations have been developed for the kinematics and response characterization of thick-walled and thin-walled circular cylindrical tubes (see, for instance [6]). By using the membrane theory, a good approximation of the behavior for isotropic and anisotropic tubes showing inflation while subjected to internal pressures is set. However, with the membrane theory framework is not possible to consider the stress distribution through the wall thickness and thus, the effect of residual stresses present in the artery walls cannot be represented.

The nature of a residual stress field and its effect on elastic response has also been studied from an analytical framework ([6], [40], [43]). It has been demonstrated that the response of elastic bodies with such residual stress fields is geometry dependent and, thus, inhomogeneous, as in the boundary of an infinitesimal material volume the surface tractions shall be zero. This means that isotropic elastic materials cannot support residual stresses, and that soft tissues response is necessarily anisotropic ([43], [45], [80]).

The analytical formulations considering residual stresses are based in some simplifications, as for example, neglecting the dependence of residual stresses on the axial direction. This means that only radial and circumferential residual stresses are considered, but it is well known that arteries are subjected to axial residual stress ([6], [11], [39], [80], [81]). Also, no geometric imperfections are typically considered for circular cylindrical models. Nevertheless, a great research effort has been (and is being made) on the effects of residual stresses in the context of biological tissues, with important results on the behavior of nonlinearly elastic solids, so it is important to remark this here (see [82]-[87]).

In this chapter, the mathematical framework for the geometry and deformation description of a circular cylindrical tube is presented in section 3.2. It is important to recall that the interest in this configuration is associated with the main applications herewith described concerning the instability of cylindrical bodies with special impact in biomechanics. Also, in that section the constitutive law of the material including residual stress is defined. The possible bifurcation modes for a thick-walled circular cylindrical tube are stated based on an incremental displacement field in section 3.3. A finite element model is structured in the commercial software Abaqus, which geometry and meshing configuration, material model implementation and analysis procedure are explained in section 3.4. These topics are common for the simulations carried out and presented in both, chapter 4 and chapter 5, with some exceptions that are specified at their corresponding sections.

3.2. Mathematical Description of the Problem

Let $\boldsymbol{B_r} \subset R^3$ be a (fixed) reference configuration of the continuous body of interest (assumed to be residually stressed) whereas current configuration is denoted as $\boldsymbol{B} \subset R^3$. The nonlinear deformation mapping describes the mapping of material points $\boldsymbol{X} \in \boldsymbol{B_r}$ onto the current configuration $\boldsymbol{x} \in \boldsymbol{B}$. Accordingly, the deformation gradient denoted by $\boldsymbol{F}$ relates the one-to-one mapping of line vectors from the reference to the current placements.

With these ingredients at hand, the symmetric and positive definite right Cauchy–Green tensor is given by $\boldsymbol{C} := \boldsymbol{F}^T\boldsymbol{F}$ and the left Cauchy–Green tensor renders $\boldsymbol{b} := \boldsymbol{F}\boldsymbol{F}^T$.

3.2.1. Geometry and Deformation

Consider a circular cylindrical tube of radius R, thickness T, and length L, whose geometry in the reference configuration $\boldsymbol{B_r}$ can be described in terms of cylindrical polar coordinates (R, Θ, Z) as ([3], [9], [16], [21]):

$$A \leq R \leq B, \quad 0 \leq \Theta \leq 2\pi, \quad 0 \leq Z \leq L, \tag{3-1}$$

where A and B are the internal and external radii, respectively. In that reference configuration the position vector of any material point can be written in parametric form as:

$$\boldsymbol{X} = \boldsymbol{R}\boldsymbol{E_R}(\Theta) + Z\boldsymbol{E_Z} \tag{3-2}$$

Where $\mathbf{E}_R$, $\mathbf{E}_\Theta$ and $\mathbf{E}_Z$ are the basis vectors in the indicated directions. The reference thickness of the tube is simply T = B − A. The cylinder is inflated and extended so that it remains a circular tube. The inflating pressure is denoted by p and the axial load by N. Thus, in the deformed configuration $\boldsymbol{x} \in \boldsymbol{B}$ the geometry and the position vector can be described as:

$$a \leq r \leq b, \quad 0 \leq \theta \leq 2\pi, \quad 0 \leq z \leq l \tag{3-3}$$

$$\boldsymbol{x} = r\boldsymbol{e}_r(\theta) + z\boldsymbol{e}_z \tag{3-4}$$

Here, r, θ and z are cylindrical polar coordinates and $\mathbf{e}_r$, $\mathbf{e}_\theta$, $\mathbf{e}_z$ are unit vectors in the deformed configuration, whereas the deformed length of the cylinder is identified by l. Referring to the cylindrical coordinate system, the associated deformation gradient tensor F can be represented as:

$$\mathbf{F} = \begin{bmatrix} \lambda_r & 0 & 0 \\ 0 & \lambda_\theta & 0 \\ 0 & 0 & \lambda_z \end{bmatrix} \tag{3-5}$$

The deformation is isochoric because of the incompressibility of the material, which means that:

$$\det(\boldsymbol{F}) = \lambda_r \lambda_\theta \lambda_z = 1 \tag{3-6}$$

$$\lambda_r = {\lambda_\theta}^{-1} {\lambda_z}^{-1} \tag{3-7}$$

The azimuthal principal stretch is $\lambda_\theta = \frac{r}{R} > 0$, and the axial stretch is $\lambda_z = \frac{l}{L}$ ([6], [41]).

3.2.2. Equilibrium and Constitutive Model with Residual Stress

In line with [21] [41], the description of the modelling framework for the treatment of residual stresses in deformable bodies is discussed in what follows for the case of hyperelastic materials. The physical assumption involves the postulation of a free-energy density function W defined per unit volume of the reference configuration that admits as primary fields both the deformation gradient $\boldsymbol{F}$ and the residual stress field $\boldsymbol{\sigma}_0$. A plausible generalization is given by:

$$W = W(\boldsymbol{F}, \boldsymbol{\sigma}_0) \tag{3-8}$$

It is assumed that the constitutive law is characterized by the existence of a residual stress field $\boldsymbol{\sigma}_0$ in the reference configuration $\boldsymbol{B_r}$. Note that this study relies on the hypothesis stating that the residual field is a prescribed quantity. Residual stress is considered to exist inside the material body $\boldsymbol{B_r}$ in the absence of body forces and surface tractions on the boundary $\partial\boldsymbol{B_r}$. Accordingly, the residual stress field is characterized by a non-uniform, symmetric second order tensor that satisfies the balance of linear and angular momentum, i.e. (see section 2.1):

$$\boldsymbol{\sigma}_0 = {\boldsymbol{\sigma}_0}^T \tag{3-9}$$

The tensor $\boldsymbol{\sigma_0}$ is unaffected by rotations in the deformed configuration $\boldsymbol{B}$ and W depends on the deformation gradient $\boldsymbol{F}$ only via the right Cauchy–Green deformation tensor $\boldsymbol{C} = \boldsymbol{F}^T\boldsymbol{F}$, which is symmetric and positive definite ([21], [41]). Then, W is automatically objective. Furthermore, in the absence of any intrinsic material symmetry W is an isotropic function of the combination of $\boldsymbol{C}$ and $\boldsymbol{\sigma}_0$ and the following symmetry statement holds for any orthogonal tensor Q in $\boldsymbol{Br}$:

$$W(Q\boldsymbol{F}Q^T, Q\boldsymbol{\sigma}_0 Q^T) = W(\boldsymbol{F}, \boldsymbol{\sigma}_0) \tag{3-10}$$

It follows that W may be defined by an invariant formulation, which is based on the invariants of $\boldsymbol{C}$, $\boldsymbol{\sigma}_0$ and their combination. For an incompressible isotropic material, the strain energy depends on the following two independent invariants of $\boldsymbol{C}$:

$$I_1 = tr(\boldsymbol{C}) \tag{3-11}$$

$$I_2 = \frac{1}{2}[(tr\boldsymbol{C})^2 - tr(\boldsymbol{C}^2)] \tag{3-12}$$

For an incompressible hyperelastic residually stressed material in a three-dimensional analysis the invariant formulation constitutes a set of nine independent quantities. Please refer to [40] for the complete invariant formulation under these conditions. In this study, it is considered the dependence of W on $\boldsymbol{C}$ and $\boldsymbol{\sigma}_0$ through the invariants I_1, I_5 and I_6. The general form of the considered strain energy density function is as follows:

$$W(I_1, I_5, I_6) = \frac{\mu}{2}(I_1 - 3) + \frac{f}{2}(I_5 - tr\boldsymbol{\sigma}_0) + \frac{1-f}{4}(I_6 - tr\boldsymbol{\sigma}_0) \tag{3-13}$$

Where μ is the shear modulus of the material in the reference configuration and the weighting factor for the invariants I_5 and I_6 is taken as $f = \{0,1\}$. The above indicated invariants are defined as:

$$I_1 = tr\boldsymbol{C} \tag{3-14}$$

$$I_5 = tr(\boldsymbol{\sigma}_0\boldsymbol{C}) \tag{3-15}$$

$$I_6 = tr(\boldsymbol{\sigma}_0\boldsymbol{C}^2) \tag{3-16}$$

It should be noted that if the residual stress tensor vanishes, the formulation corresponds to the strain energy of a Neo-Hookean material. As W is represented as a function of the deformation invariants, the Cauchy stress tensor takes the following form:

$$\boldsymbol{\sigma} = 2W_1\boldsymbol{b} + 2W_5\boldsymbol{\Sigma} + 2W_6(\boldsymbol{\Sigma b} + \boldsymbol{b\Sigma}) - q\boldsymbol{I} \tag{3-17}$$

The notation W_i has been introduced to follow the dependence of W on the invariants as:

$$W_i = \frac{\partial W}{\partial I_i} \quad i = 1, 5, 6 \tag{3-18}$$

The factor q is a Lagrange multiplier representing the (arbitrary) hydrostatic pressure due to the incompressibility constraint, $\boldsymbol{b} = \boldsymbol{FF}^T$ is the left Cauchy-Green deformation tensor and the notation for the Eulerian tensor $\boldsymbol{\Sigma} = \boldsymbol{F\sigma_0F}^T$ (which is the transformation of $\boldsymbol{\sigma}_0$ from $\boldsymbol{B}_r$ to $\boldsymbol{B}$) has been introduced. In absence of body forces and surface tractions, the Cauchy ($\boldsymbol{\sigma}$) and the Nominal Stress tensor (S) in every point in the body satisfy the equilibrium equations:

$$div\boldsymbol{\sigma} = \mathbf{0} \tag{3-19}$$

$$Div\boldsymbol{S} = \mathbf{0} \tag{3-20}$$

where div and Div are the divergence operators in the deformed $\boldsymbol{B}$ and the reference configuration $\boldsymbol{B}_r$, respectively. The nominal stress tensor (transpose of the first Piola–Kirchhoff) is related to Cauchy stress by the following relation:

$$\boldsymbol{J\sigma} = \boldsymbol{FS} \tag{3-21}$$

Recalling that because of the incompressibility constraint $J = det(\boldsymbol{F}) = 1$,

$$\boldsymbol{\sigma} = \boldsymbol{FS} \tag{3-22}$$

Furthermore, the residual stress field must satisfy the equilibrium equations $Div\boldsymbol{\sigma}_0 = \mathbf{0}$ and the condition $\boldsymbol{\sigma}_0\boldsymbol{N} = \mathbf{0}$ on the boundary $\partial\boldsymbol{B}_r$ with $\mathbf{N}$ denoting the outer normal vector in the reference configuration. Note that to obey these conditions the residual stress field is necessarily non-homogeneous and generally induces anisotropy on the mechanical response.

In this work it is considered the dependence of W on either I_5 or I_6. To consider the dependence of W just on I_6, the weighting factor must take the value $f = 0$, in which case the strain energy density function and the Cauchy stress tensor are reduced to the following terms:

$$W(I_1, I_6) = \frac{\mu}{2}\,(I_1 - 3) + \frac{1}{4}\,(I_6 - tr\boldsymbol{\sigma}_0) \tag{3-23}$$

$$\boldsymbol{\sigma} \;=\; 2W_1\boldsymbol{b} \;+\; 2W_6(\boldsymbol{\Sigma}\boldsymbol{b} \;+\; \boldsymbol{b}\boldsymbol{\Sigma}) - q\boldsymbol{I} \tag{3-24}$$

$$W_i \;= \frac{\partial W}{\partial I_i} \qquad i \;=\; 1, 6 \tag{3-25}$$

Similarly, to consider just the influence of the invariant I_5, the weighting factor must take the value of $f = 1$:

$$W(I_1, I_5) = \frac{\mu}{2}\,(I_1 \;-\; 3) + \frac{1}{2}(I_5 - tr\boldsymbol{\sigma}_0) \tag{3-26}$$

$$\boldsymbol{\sigma} = 2W_1\boldsymbol{b} + 2W_5\boldsymbol{\Sigma} - q\boldsymbol{I} \tag{3-27}$$

$$W_i \;= \frac{\partial W}{\partial I_i} \qquad i \;=\; 1, 5 \tag{3-28}$$

In chapters 4 and 5, the residual stress fields applied for the different simulations and compatible with these conditions will be defined.

3.3. Bifurcation Modes for Thick-Walled Tubes

To investigate the possible bifurcation modes of the inflated cylinder an incremental displacements approach is followed (as described in section 2.2.3). For the cylindrical coordinates system, the incremental displacement field is of the form [17]:

$$\delta\boldsymbol{u} = \delta u_r(r,\theta,z)\boldsymbol{e}_r + \delta u_\theta(r,\theta,z)\boldsymbol{e}_\theta + \delta u_z(r,\theta,z)\boldsymbol{e}_z \tag{3-29}$$

Where δu_r, δu_θ and δu_z are the incremental displacements with respect to the deformed or current configuration of the body in equilibrium. Following [17] essentially three distinct possible bifurcation modes can be obtained:

- Prismatic mode, for which the incremental displacement field is assumed to be independent of z.

$$\delta\boldsymbol{u} = \delta u_r(r,\theta)\boldsymbol{e}_r + \delta u_\theta(r,\theta)\boldsymbol{e}_\theta \tag{3-30}$$

- Bulging mode, for which the incremental displacements are assumed to be independent of θ. Under this condition, the cross sections of the tube retain its circular shape and the displacement is axisymmetric, which can be written as (see Figure 3.1):

$$\delta\boldsymbol{u} = \delta u_r(r,z)\boldsymbol{e}_r + \delta u_z(r,z)\boldsymbol{e}_z \tag{3-31}$$

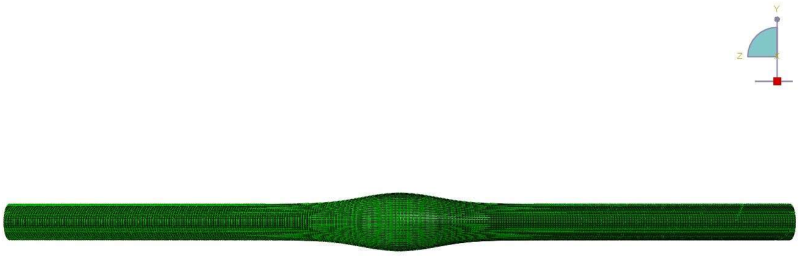

Figure 3.1: Bulging bifurcation mode of a cylindrical tube with axial stretch $\lambda_z = 1.40$, $\bar{\alpha}_d = -40$, $\bar{\alpha}_c = 0.5$, and considering the contribution of I_5 invariant.

- Bending or composite mode, which is the general case and no assumptions about the incremental displacement components of $\delta\boldsymbol{u}$ is considered, this is, the incremental displacement field described by equation (3-29) is taken (see Figure 3.2).

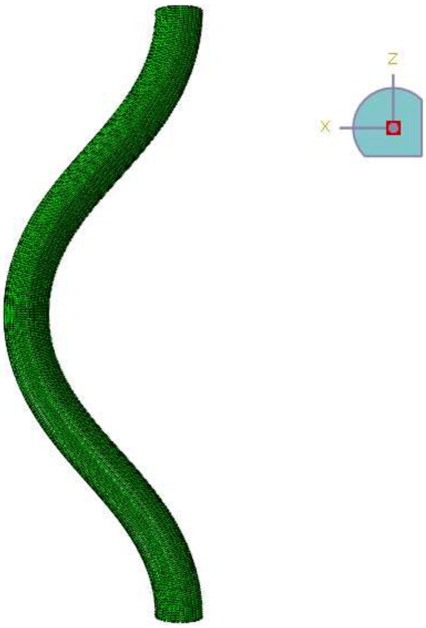

Figure 3.2: Bending bifurcation mode of a cylindrical tube with axial stretch $\lambda_z = 1.00$, $\bar{\alpha}_d = 40$, $\bar{\alpha}_c = 0.5$, and considering the contribution of I_5 invariant.

3.4. Computational Modelling

The Finite Element approach is used to face the problem at hand, Abaqus software is used for modelling and analysis. The Finite Element Method is a numerical methodology that allows to solve complex problems that from an analytical point of view would be very time consuming or that would have no analytical solution. Nowadays, it is a well-known and extended numerical approach and it is not the aim of this work to explain the fundamentals of the method. The reader is referred to ([1], [2]) for a deep dive into the fundamental concepts of the method.

3.4.1. Geometry and Discretization

A cylindrical tube is considered with the following geometrical relations:

- L/D = 20
- T/D = 0.05

Where,

L is the tube length;

D is the tube diameter;

T is the tube thickness;

The tube dimensions are taken as L = 50mm, D = 2.5mm and T = 0.125 mm. An imperfection at the center of the tube with a maximum deviation of $1 \cdot 10^{-3}B$ with respect to the undeformed configuration is introduced. This avoids a strict numerical bifurcation, this is, it allows to capture a smooth behavior of the structure as it reaches the bifurcation point. It also reduces computational time as it drives the analysis method to reach the bifurcation point in the simulation ([13], [14], [21]). The tube is meshed with three-dimensional hybrid linear solid elements (C3D8RH in the Abaqus notation) for the spatial discretization of the geometry. As the material type implies incompressible elastic finite deformation behavior, the hybrid (mixed) formulation available in Abaqus software is used. Otherwise, a purely hydrostatic pressure could be applied to the elements without any change in the nodal displacements and the resulting stresses could not be computed from a displacement history-based formulation. Thus, in Abaqus, mixed formulation elements are used with both, displacement and stress variables, in which for the latter a Lagrange multiplier is introduced in the constitutive law as an independently interpolated basic solution variable coupled with the displacement solution (coupled pressure-displacement), representing the pressure stress. This formulation in Abaqus also avoids volume strain locking problems, which occurs when the finite element mesh cannot properly represent incompressible deformations [44].

Different discretization schemes are employed in the current investigation ranging from 200 to 900 elements in the axial direction depending on the magnitude of axial stretch. This discretization relies on previous analysis[21] done by running several simulations for each value of axial stretch in the considered range ($1 \leq \lambda_z \leq 1.8$). For bulging analyses (i.e. imposed zero azimuthal displacements along the tube length), 32 elements in the circumferential direction are usually taken. This value increases to 80 elements in the case of general analyses not restricted to bulging, which includes bending bifurcation. Along the thickness direction, to capture the residual stress, a discretization of 5–7 elements is required for a proper representation and to avoid locking issues in bending deformation patterns.

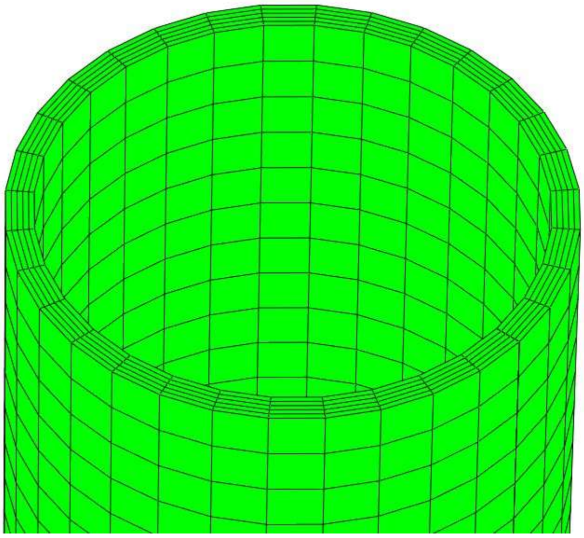

Figure 3.3: Spatial discretization of the model.

3.4.2. Material Model Implementation

The material model has been implemented in Abaqus as a subroutine to be used for incompressible hybrid elements. The UMAT (User Material) tool in Abaqus allows to define any material constitutive law, which is very powerful for these kinds of problems where the corresponding mechanical constitutive behavior is not represented by any built-in material. Only the deviatoric parts of the stress tensor and the Jacobian matrix need to be defined for a fully incompressible material response through user subroutine UMAT. Abaqus automatically accounts for the pressure stress based on a Lagrange multiplier. When using a hybrid element with user subroutine UMAT, Abaqus Standard replaces the pressure stress calculated from the stress tensor returned by the user subroutine with that derived from the Lagrange multiplier and modifies the Jacobian appropriately [44], [88].

The UMAT is coded using FORTRAN based programming language. The interface provided by Abaqus Documentation [44] is the starting point for any UMAT coding. In Abaqus Standard, an analysis can be carried out by defining the analysis procedure within a time step, which is discretized in time increments for performing iterations until equilibrium is reached. When equilibrium is achieved for an iteration, the next time increment of the step starts. This is repeated until the total number of time increments defined for the step is reached unless equilibrium is not achieved after several iterations within a time increment, then Abaqus Standard finishes the analysis.

Within the step in which the bifurcation analysis is carried out, the UMAT is called at the start of time increments. Some variables are passed into the UMAT for information, such as the strain tensor and the strain increments array, the size of the stress and strain component array, the number of solution-dependent state variables associated with the material, the material constants, the current coordinates matrix associated with each point, the deformation gradient matrix at the beginning and at the end of the increment, and others. The stress tensor at the end of the previous increment is also passed in at the beginning of each new increment. In case that initial conditions, such as residual stresses have been defined, the stress tensor passed at the beginning of the first time-increment of the analysis contains these pre-defined field.

After initialization of the UMAT the initial stiffness matrix relative to the configuration at the beginning of the time increment is assembled, and based on the applied loads, the displacements and strains are computed. The right Cauchy-Green deformation tensor $\boldsymbol{C}$ is calculated and the stress tensor which depends on the strain energy potential, as defined by the constitutive law of the material, is computed and updated. The consistent Jacobian matrix $\boldsymbol{J} = \frac{\partial \Delta \boldsymbol{\sigma}}{\partial \Delta \boldsymbol{\varepsilon}}$ is also computed and any state variable updated. As this is a finite strain problem, Abaqus provides deformation as logarithmic strain components [44]. Then, the internal forces are compared with the externally applied forces to check equilibrium convergence. If convergence is achieved, the updated stiffness matrix is used as the initial stiffness matrix at the beginning of the next increment.

The following scheme constitutes the coding interface provided in Abaqus Documentation [88], in which the stress tensor STRESS and consistent Jacobian matrix DDSDDE equations need to be defined to construct the UMAT:

```
“SUBROUTINE UMAT(STRESS,STATEV,DDSDDE,SSE,SPD,SCD,
   1 RPL,DDSDDT,DRPLDE,DRPLDT,
   2 STRAN,DSTRAN,TIME,DTIME,TEMP,DTEMP,PREDEF,DPRED,CMNAME,
   3 NDI,NSHR,NTENS,NSTATV,PROPS,NPROPS,COORDS,DROT,PNEWDT,
   4 CELENT,DFGRD0,DFGRD1,NOEL,NPT,LAYER,KSPT,JSTEP,KINC)
C
    INCLUDE 'ABA_PARAM.INC'
C
    CHARACTER*80 CMNAME
    DIMENSION STRESS(NTENS),STATEV(NSTATV),
   1 DDSDDE(NTENS,NTENS),DDSDDT(NTENS),DRPLDE(NTENS),
   2 STRAN(NTENS),DSTRAN(NTENS),TIME(2),PREDEF(1),DPRED(1),
   3 PROPS(NPROPS),COORDS(3),DROT(3,3),DFGRD0(3,3),DFGRD1(3,3),
   4 JSTEP(4)

    user coding to define DDSDDE, STRESS, STATEV, SSE, SPD, SCD
    and, if necessary, RPL, DDSDDT, DRPLDE, DRPLDT, PNEWDT

    RETURN
    END’
```

3.4.3. Modified Riks Method. General Description

The numerical procedure used in the analysis step within the Abaqus simulations is the Riks method. It is generally used to study geometrically nonlinear collapse of a structure [44]. In Abaqus the nonlinear material behavior and boundary conditions can be accounted for within this analysis procedure. It is useful to speed convergence on ill-conditioned problems and avoids snap-through problems. This method can be used when the loads are represented by a single scalar (as the inflation pressure) and the loading can be proportional. This analysis procedure should be implemented when the material and geometrical nonlinearity are present before buckling or if unstable response after buckling is expected.

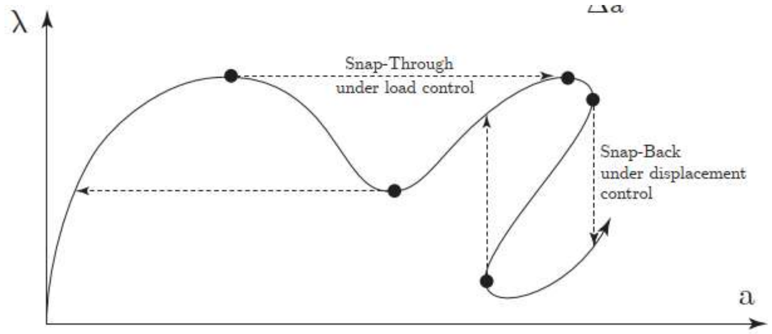

Figure 3.4: Snap-through possible in unstable system under displacement and load control [89].

The load defined (internal pressure) is ramped up from an initial value to the specified load reference value. The load magnitude is an unknown along with the displacements, so to measure the evolution of the solution, Abaqus uses the arc length parameter along the static equilibrium path in load-displacement space. The load magnitude at a current state is defined as:

$$\mathrm{P} = P_0 + \lambda(P_{ref} - P_0) \tag{3-32}$$

Where P is the total load at a current state, P_0 is any load passed from previous abaqus analysis steps (if it is not redefined in the current analysis step) and that is treated as a dead load, P_{ref} is the predefined load value and λ is the load proportionality factor (LPF). In this procedure, the user has no control on the load applied because this parameter is automatically computed in each increment and iteration, excepting the initial load proportion that is to be applied $\Delta\lambda_{in}$, which is a user input. Minimum and maximum arc length increments can be defined and used to control the automatic incrementation [44].

This method works better when the load-displacement path is smooth. To analyze the post-buckling behavior, a strict numerical bifurcation must be avoided. This can be done by introducing an imperfection to the model in order to follow a smooth response of the structure before reaching a critical (collapse) load. For a more detailed review on this method and these features, see [13]. The Riks method then introduces two concepts, the load proportionality factor, which indicates the load applied on the structure at each time increment within the Abaqus analysis step, and the arch length, which is an indicator of the evolution of the deformation of the structure (see [44], [89] for the theoretical methodology and the numerical implementation of the method). A typical profile of the LPF vs arc length parameter is shown in Figure 4.6.

4. Computational Bifurcation Analysis for Thick-Walled Circular Cylindrical Tubes with the Influence of a Plane Residual Stress Field

4.1. Introduction

In this section results of the bifurcation analysis carried out for a thick-walled circular cylindrical tube subjected to a plane residual stress field are presented. Only radial and azimuthal components of the residual stress tensor are considered to affect the hyperelastic incompressible material body. Several numerical simulations are carried out considering different values for the residual stress coefficients. For a model with a specific value of strength of residual stress, several simulations are run varying the applied axial stretch to evaluate its influence on the bifurcation mode and its post-bifurcation behavior. Firstly, the stresses state along the cylinder is analyzed and the moment equilibrium condition for cylinders with no bending stiffness is used to get a rough but fair prediction on the expected bifurcation mode. Secondly, the bifurcation pressures as a function of the axial stretch for the different numerical models are compared and assessed. These results and the related analysis are explained in more detail in [21].

4.2. Residual Stress Field

A residual stress tensor that complies with the conditions indicated in section 3.2.2 is defined forth:

$$\boldsymbol{\sigma_0} = \begin{bmatrix} \sigma_{0RR} & 0 & 0 \\ 0 & \sigma_{0\Theta\Theta} & 0 \\ 0 & 0 & 0 \end{bmatrix} \qquad (4\text{-}1)$$

$$\sigma_{0RR} = \alpha_c(R - A)(R - B) \tag{4-2}$$

$$\sigma_{0\Theta\Theta} = \alpha_c[3R^2 - 2(A + B)R + AB] \tag{4-3}$$

The planar residual stress tensor $\boldsymbol{\sigma_0}$ has only radial and azimuthal non-zero stress components, thus it is considered that there is no shear stress. Recalling from section 3.2.2, this residual stress tensor satisfies the equilibrium equation and the boundary condition:

$$Div\boldsymbol{\sigma}_0 = \mathbf{0} \tag{4-4}$$

$$\boldsymbol{\sigma}_0\boldsymbol{N} = \mathbf{0} \text{ on the boundary } \partial\boldsymbol{B}_r \tag{4-5}$$

As the component $\sigma_{0ZZ} = 0$, the non-trivial solution of the equilibrium equation is the radial equation:

$$\frac{d\sigma_{0RR}}{dR} + \frac{1}{R}(\sigma_{0RR} - \sigma_{0\Theta\Theta}) = 0 \tag{4-6}$$

It should be noticed that $\sigma_{0RR} = 0$ on $R = A \text{ or } B$. Also, if σ_{0RR} is known, then the azimuthal component can be derived by applying the product (derivative) rule:

$$\sigma_{0\Theta\Theta} = \frac{d}{dR}(R\sigma_{0RR}) \tag{4-7}$$

The parameter α_c is the strength of the planar residual stress with units of stress per square length. It can be expressed in the following normalized form, in which the magnitude of the residual stress is controlled by the non-dimensional factor $\bar{\alpha}_c$:

$$\alpha_c = \frac{\mu\bar{\alpha}_c}{2BT} \tag{4-8}$$

The stress values obtained in the simulations will be normalized with respect to the material constant $\frac{\mu}{2}$. There is no reliable data on residual stresses in the context of studying Abdominal Aortic Aneurysms, however, these expressions for the residual stress components follow a behavior that is consistent with that obtained from the opening angle method [10], and so, they are suitable for carrying out a qualitative study of its effects on the material body response. Please, refer to [90] for specific values of residual stress. Two values for $\bar{\alpha}_c$ are considered. These values controlling the planar residual stresses are chosen such that they are neither very high to take the model near any instability nor very low to have negligible effects, their distribution is shown in Figure 4.1 and Figure 4.2. After a few preliminary computations and through performing a careful sensitivity analysis, the values for this parameter are taken as $\bar{\alpha}_c \in \{0.5,\ 0,\ -0.5\}$.

From Figure 4.1 can be appreciated that the boundary condition $\boldsymbol{\sigma}_0\boldsymbol{N} = \boldsymbol{0}$ on $\partial\boldsymbol{B_r}$ is satisfied, as the radial residual stress is zero at the inner and outer surfaces of the tube. Furthermore, as it is shown in Figure 4.2 (b), a positive value of $\bar{\alpha}_c$ introduces tensile hoop residual stress in the outer surface of the cylindrical tube, whereas at the inner surface of the tube there is compressive hoop residual stress. The opposite effect is expected for a negative value of $\bar{\alpha}_c$, as it can be appreciated from Figure 4.2 (c). From both Figure 4.1 and Figure 4.2, the independence of the residual stress on the axial direction of the tube can be acknowledged.

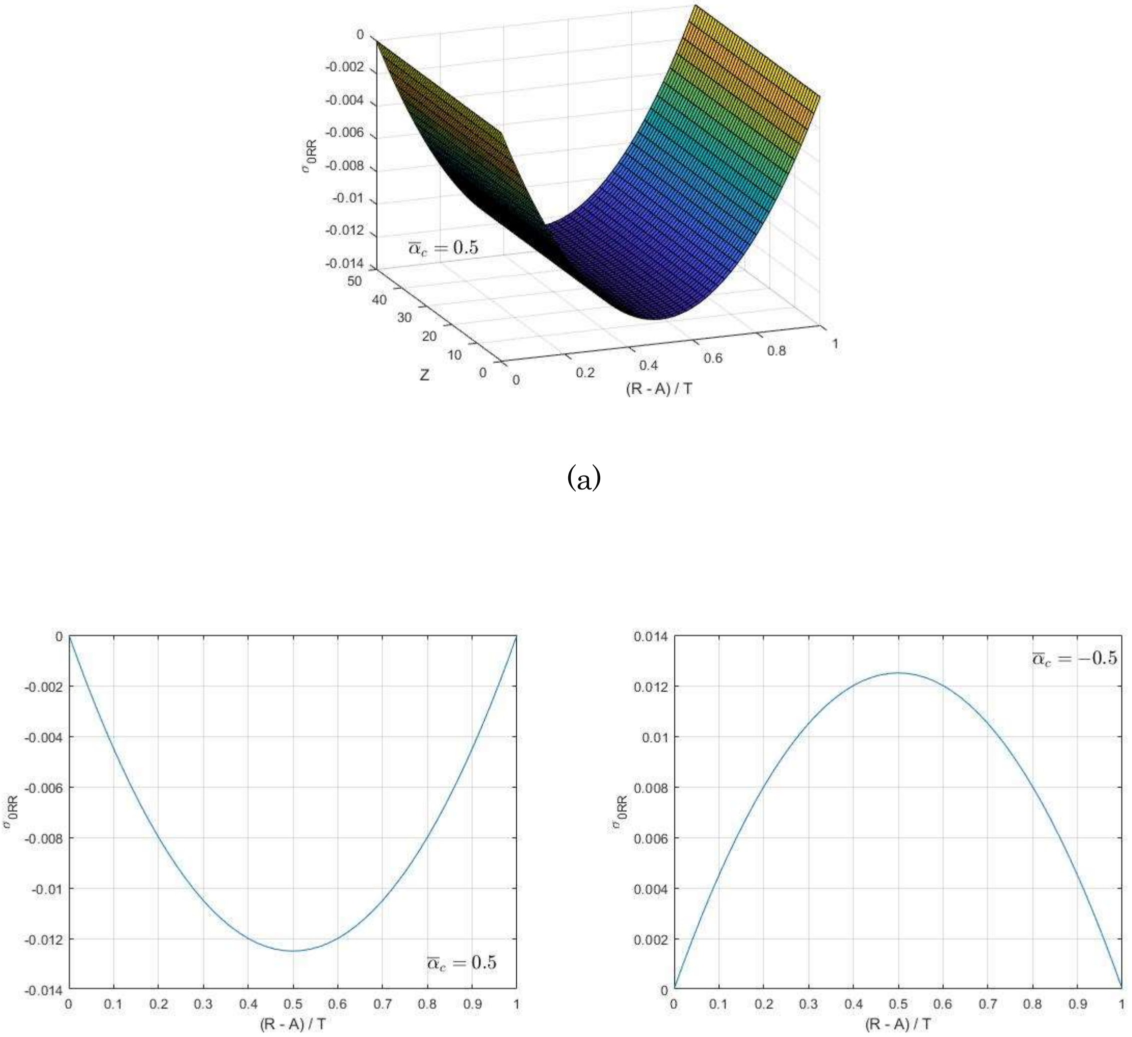

(a)

(b)

(c)

Figure 4.1: Residual stress component σ_{0RR} variation for a cylindrical tube with inner radius A and thickness T: (a) shows its independence on axial coordinate Z; (b) and (c) show the radial residual stress distribution along the thickness for both, $\bar{\alpha}_c = 0.5$ and $\bar{\alpha}_c = -0.5$.

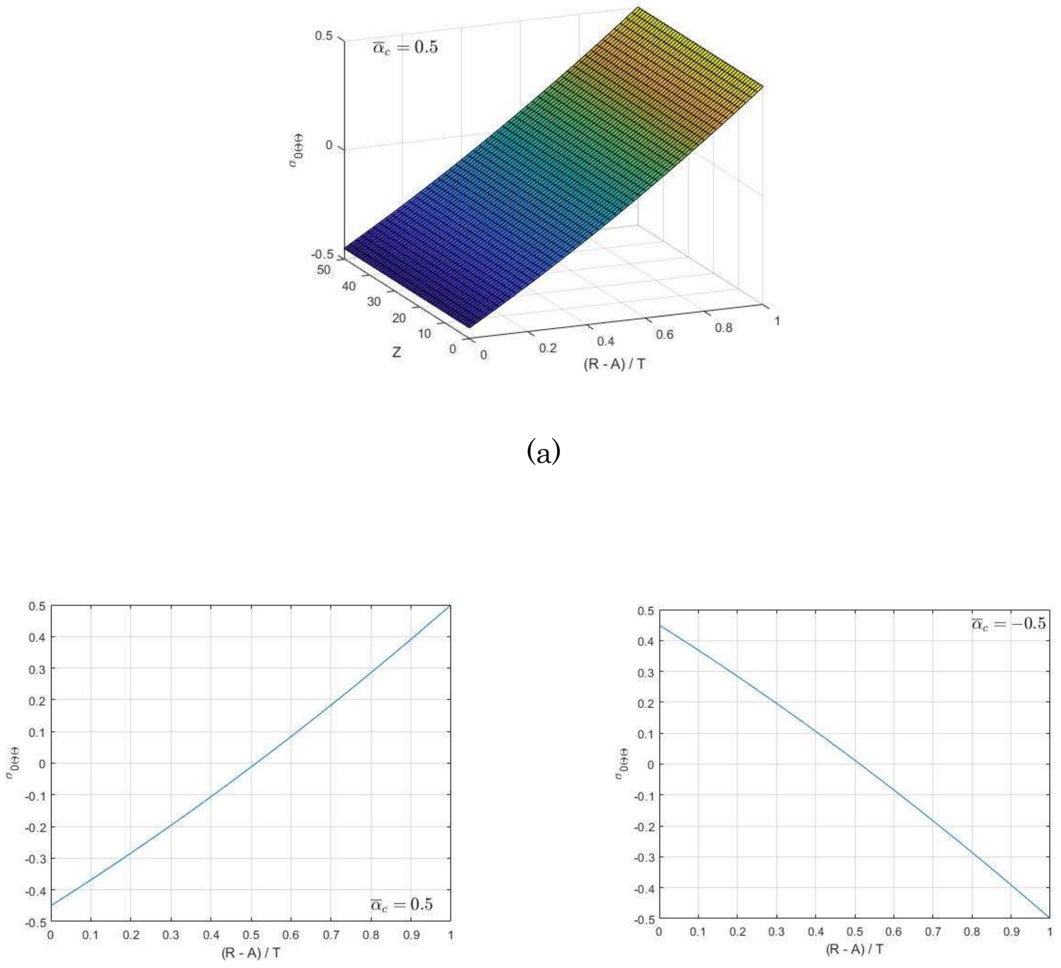

(a)

(b)

(c)

Figure 4.2: Residual stress component $\sigma_{0\Theta\Theta}$ variation for a cylindrical tube with inner radius A and thickness T: a) shows its independence on axial coordinate Z; b) and c) show the azimuthal residual stress distribution along the thickness for both, $\bar{\alpha}_c = 0.5$ and $\bar{\alpha}_c = -0.5$.

4.3. Numerical Procedure

In Abaqus, each numerical simulation is carried out in three steps. In the first step of the simulation, residual stresses are introduced into the model via the use of the routine SDVINI that assigns initial field values to the elements of the model (see equations (4-2) and (4-3). In Figure 4.3 it is shown the distributions obtained from a numerical simulation for a tube with $\bar{\alpha}_c = 0.5$. It can be appreciated that comparing with the analytical values derived from equations (4-2) and (4-3) the values from both solutions follow similar profiles and they almost coincide.

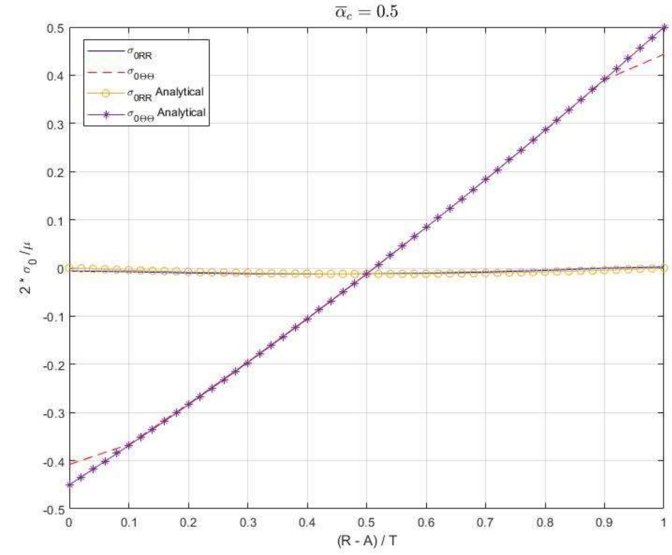

Figure 4.3: Normalized radial and azimuthal residual stress components. Results at the middle cross-section of a tube from a numerical simulation with $\bar{\alpha}_c = 0.5$ are compared with the values obtained by the analytical equations (4-2) and (4-3).

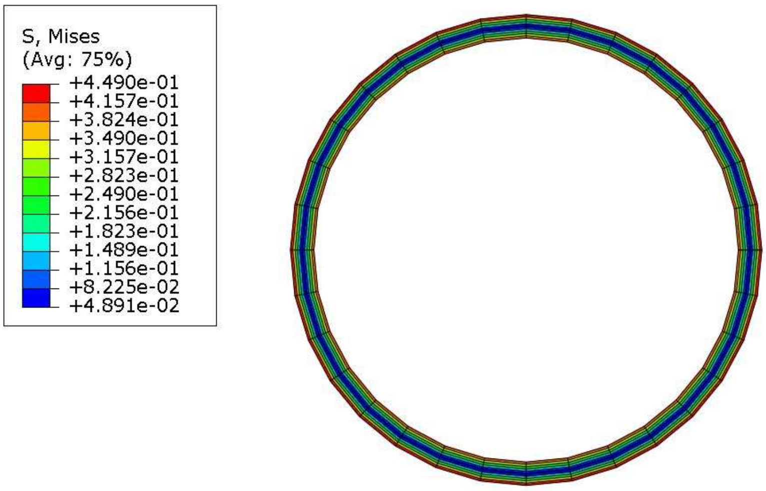

Figure 4.4: Contour plot of Von Mises stress showing its distribution in the middle cross section for the model with $\bar{\alpha}_c = 0.5$.

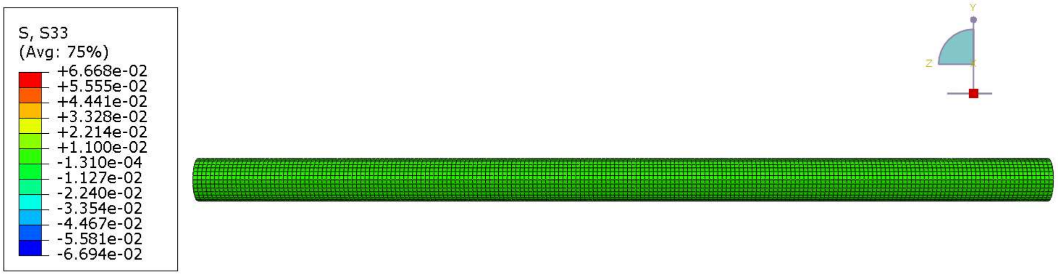

(a) Contour plot of the axial stress component showing no residual stress along the tube length.

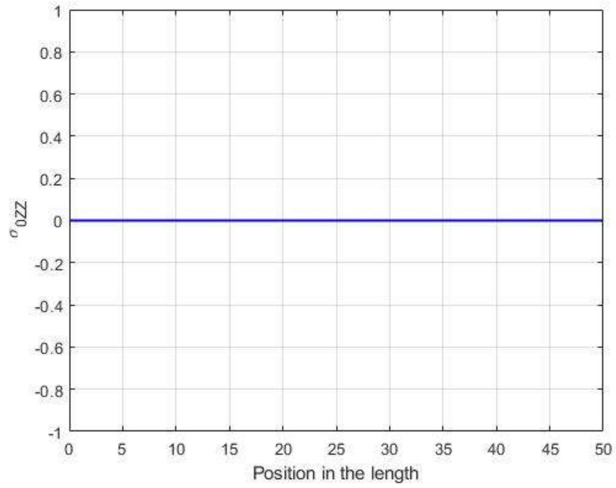

(b) Plot of average axial stress at each cross-section of the tube.

Figure 4.5: Axial residual stress component along the longitudinal axis for the model with $\bar{\alpha}_c = 0.5$, showing negligible values, consistent with a planar $R - \Theta$ residual stress field.

In the second step, the axial stretch is applied imposing axial displacements at one end while keeping zero axial displacements at the other end. Hoop displacements should be prevented at both ends of the cylinder during the first and second step to keep the perfect circular cylindrical shape.

In the last step, an internal pressure of magnitude ($p = 10\,\mu\,T/D$) is applied on the inner surface of the cylinder. Then, a non-linear analysis is carried out by means of the Riks-Modified Method. As it has been mentioned in previous sections, this methodology introduces two parameters, namely, the load proportional factor (LPF), which is an indicator of the applied load, and the arc length, which is an indicator of the evolution of the deformation. To be able to capture any possible instability mode during this step, only hoop and axial displacements at the ends of the cylinder are restricted. However, when the aim of the analysis is to capture just bulging bifurcation, especially in those models where bending bifurcation can occur prior to bulging, hoop displacements should be prevented along the cylinder length for the three steps, imposed in a cylindrical coordinate system. Typical layout of the curves obtained through the Riks-Modified Method are presented in Figure 4.6.

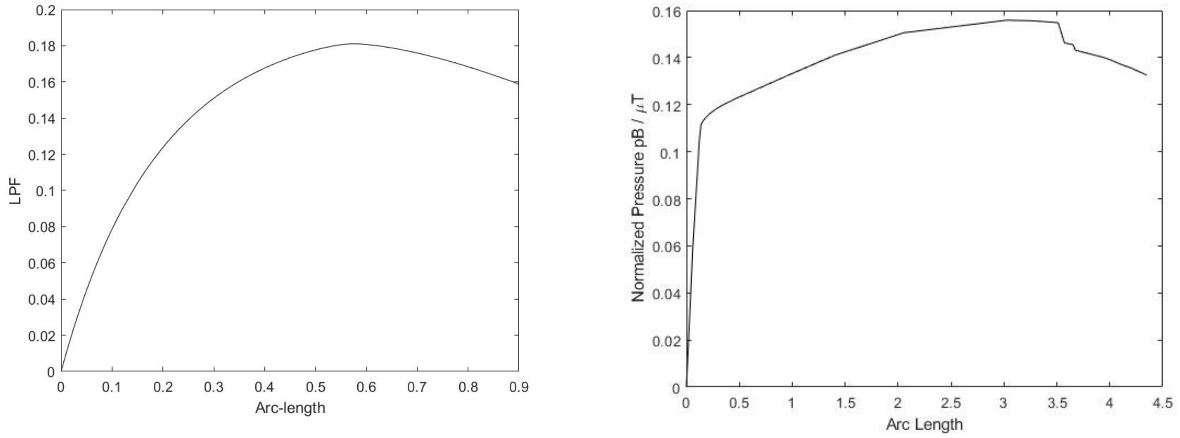

(a)

(b)

Figure 4.6: (a) Typical profile of the Load Proportionality Factor vs. Arc length parameter resulting from an analysis by Riks-modified method for an arbitrary model; (b) Values of normalized inflation pressure vs. Arc length for a model with $\bar{\alpha}_c = 0.5$, $\lambda_z = 1.02$ and $f = 1$ (I_5 invariant).

The curve profile in Figure 4.6 (b) exhibits two critical points at which the tendency changes dramatically. There is a first branch of the curve that follows an almost proportional path until a first bifurcation from the so far followed behavior occurs. At this first “break point” in the curve, large displacements are developed under a geometrical nonlinear behavior characteristic of bending buckling. The cylindrical tube, in subsequent motion can sustain more pressure load up to a second derivation from the so far followed behavior occurs. At this moment localized deformation in the form of a bulge starts to develop, growing radially with a continuous loss of stiffness.

The numerical analysis conducted in this work follows the guidelines given in [16], [21] and [91]. To capture bulging, the evolution of the azimuthal stretch of two points, one inside the bulge and another out of that place is tracked. The bulging bifurcation point is determined when the profiles of these two points separate from each other.

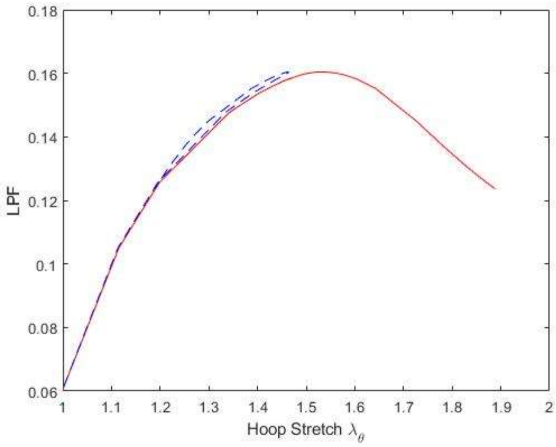

a) Load Proportional Factor vs azimuthal stretch.

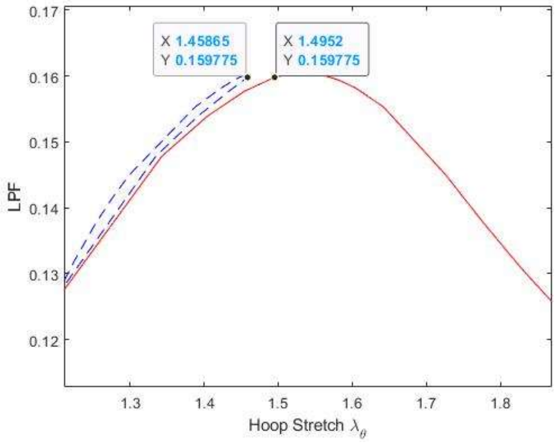

b) Widened frame from figure a) identifying the azimuthal stretch of the two points at the bifurcation.

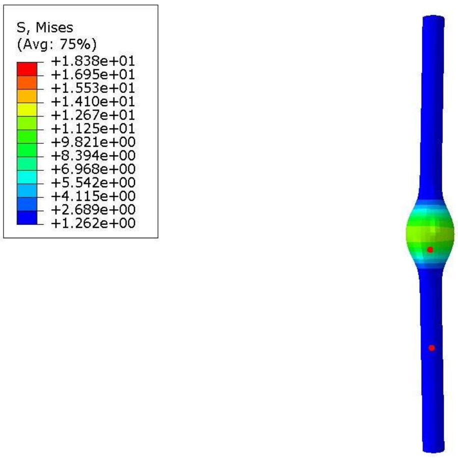

c) Location of the points (highlighted in red color) on the tube.

Figure 4.7: Load Proportional Factor vs azimuthal stretch for two points of a model with applied axial stretch $\lambda_z = 1.2$, $\bar{\alpha}_c = -0.5$ and I_5 invariant identifying bulging bifurcation occurrence. The point inside the bulge (continuous red line in figures a) and b) and the point outside the bulge (dashed blue line in figures a) and b) present the same azimuthal stretch before diverging and following different paths. The point outside the bulge reverses its path (showing deflation) whereas the point inside the bulge continues to inflate.

More in particular, the bifurcation point is taken when the deviation of the azimuthal stretches of these two points is a small fraction of the azimuthal stretch average computed from both points (for instance, 1% or 2%). As inflation continues, the azimuthal stretch of the point inside the bulge increases, whereas at the other point outside the bulge the azimuthal stretch decreases. This behavior can be seen in Figure 4.7. Following this criteria and although the results obtained throughout this work are analyzed from a qualitative standpoint, for the previous plot generated for a model with axial stretch of $\lambda_z = 1.2$, $\bar{\alpha}_c = -0.5$ and considering the I_5 invariant, the bulging bifurcation point can be set as where the Load Proportional Factor reaches a value of 0.1597 (see Figure 4.7 (b)). For this relative load value, the deviation of the azimuthal stretches of the points from their mean value is:

PARAMETER	POINT INSIDE BULGE	POINT OUTSIDE BULGE
λ_θ	1.4952	1.4587
Mean value	1.4769	
Deviation (ABS %)	1.23%	1.23%

Table 4.1: Inflation values for two points of a circular cylindrical model with an applied axial stretch $\lambda_z = 1.2$, $\overline{\alpha}_c = -0.5$ and considering the I_5 invariant, at bulging bifurcation instant.

It is noted that the bifurcation occurs before the maximum pressure is reached, but very close to this value (maximum LPF value is 0.1604).

To predict the onset of bending bifurcation in a simulation, two procedures can be described as follows. Firstly, from the membrane analysis, the condition of moment instability $\mathcal{M} > 0$ (see section 2.2) along the tube can be checked. It is emphasized that this condition states that the bending instability is reached when the resultant moment with respect to the center of each circular cross section is greater than zero (see [3], [17]), and by defining the axial force and the internal pressure in terms of the internal stresses it drives to the condition $\mathcal{M} = \sigma_{\theta\theta} - 2\sigma_{zz} > 0$. Under the current conditions, as the model is a thick-walled tube, average stresses at cross-sections of the tube should be considered for this purpose. Secondly, the combined azimuthal and radial displacements can be followed and identify a lateral movement, which suggests the initiation of bending bifurcation. It is important to note that although there could be different bending modes [3], only the first one (m=1, see Figure 4.8) is analyzed which is the expected one under the conditions at hand [17].

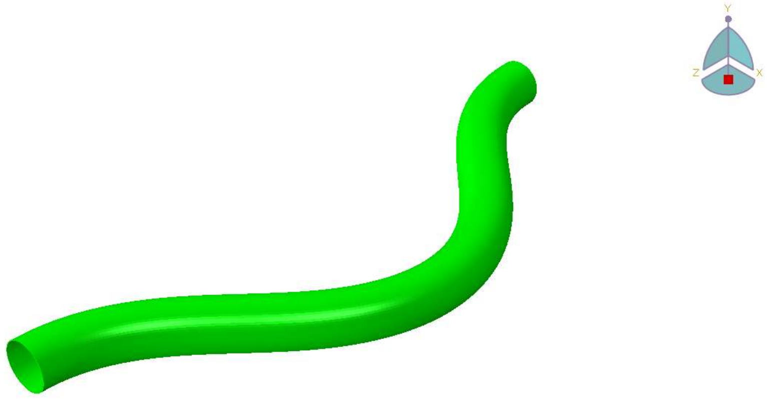

Figure 4.8: Bending bifurcation mode m=1.

The following description distinguishes the two possible bifurcation scenarios presented in Figure 4.9. Consider simulations which are affected by a plane residual stress field ($\overline{\alpha}_{\mathrm{d}} = 0$) with $\overline{\alpha}_{\mathrm{c}} = 0.5$ and $f = 1$ (I_5). In that figure values of $\sigma_{\theta\theta} - 2\sigma_{zz}$ vs arc length are presented for a model i) with $\lambda_z = 1.08$. The same plot is added for a model ii) with $\lambda_z = 1.4$. The values of $\sigma_{\theta\theta}$ and σ_{zz} are average stresses of the tubes' middle cross-sections.

For the simulation with $\lambda_z = 1.4$, it is shown that $\sigma_{\theta\theta} - 2\sigma_{zz} < 0$ (dashed line), which can be taken as a sign that bending is not expected to give the onset of bifurcation. In fact, the numerical simulation gives bulging. On the other hand, on the same figure there are values obeying $\sigma_{\theta\theta} - 2\sigma_{zz} > 0$ for the simulation with $\lambda_z = 1.08$ (continuous line). This gives an indication that bending may give the onset of bifurcation although this is not enough to establish the bifurcation scenario, thus, in the following section the bending bifurcation point will be illustrated for these two simulations.

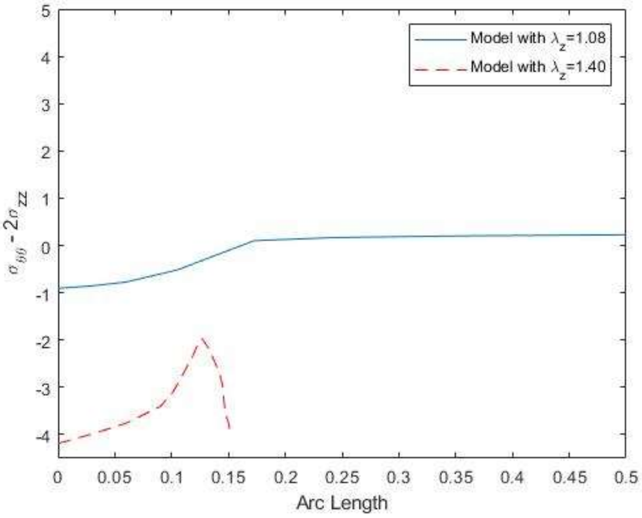

Figure 4.9: Average stress values $\sigma_{\theta\theta} - 2\sigma_{zz}$ at the middle cross-section of two models with axial stretches i) $\lambda_z = 1.08$ represented by the continuous line, and ii) $\lambda_z = 1.4$ represented by the dashed line, both for $\overline{\alpha}_c = 0.5$ and (I_5) $f = 1$.

4.4. Numerical Results

In this section, numerical results are presented for simulations in which a planar residual stress field has been considered. Models' behavior with a specific residual stress field is studied for different values of applied axial stretch. Axial stretches considered are defined in the range of $1 \leqslant \lambda z \leqslant 1.8$. In this section, results for the residual stress field with $\bar{\alpha}_c = 0.5$, for the invariant I_5 $(f = 1)$, will only be presented (see Table 4.2). A complete analysis considering all the possible combinations of the residual stress strength parameters and invariants has been carried out and published in [21]. It should be noted that the results presented here are consistent with the behavior of all those cases analyzed in [21].

It is pointed out that the presented stress values throughout this work are normalized with respect to the material constant $\mu/2$ and it is indicated here in order not to repeat it along the following sections. As a reference, it is recalled that the following combinations of the residual stress parameters are possible for a planar residual stress state, considering either $f = 0$ (I_6) or $f = 1$ (I_5) in equation (3-13):

CASE	$\bar{\alpha}_c$	$\bar{\alpha}_d$
1	0	0
2	0.5	0
3	-0.5	0

Table 4.2: Values of residual stress constitutive parameters for the different numerical simulations with planar $R - \Theta$ residual stress.

The results obtained by the numerical simulations show that for the considered thick-walled circular cylindrical tube under the conditions at hand the bifurcation mode is either bending or bulging, and that the expected bifurcation mode is influenced by the magnitude of axial stretch applied to the cylinder. This agrees with the results shown in [3], in which it was already demonstrated that either a bending or an axisymmetric bifurcation mode may occur in a cylinder of incompressible elastic material represented by a strain energy function W that is first extended and then, inflated. In that research it was also pointed out that for certain range of deformations in a very long tube, bifurcation into a buckling (bending) type mode becomes possible prior to the onset of a symmetric mode. The results shown in [3], as most of the analytical solutions dealing with this boundary value problem, start from assuming the membrane theory.

It is important to specify how bending bifurcation onset is identified. Normalized inflation pressure vs arc length is presented in Figure 4.10 for two simulations of a model with $\bar{\alpha}_c = 0.5$, $f = 1$, and with an applied axial stretch of $\lambda_z = 1.08$ (model i in the previous section). As it has been pointed out in section 3.3, to capture the bending bifurcation mode no restrictions on the azimuthal displacement field should be imposed, as well as on the radial and axial displacement fields, along the tube length. However, if azimuthal displacements are prevented along the tube, bulging mode gives the onset of bifurcation. The curves in Figure 4.10 are constructed from two simulations run for the same model: one simulation with azimuthal displacements restricted along the tube length, and another without this restriction. It is shown that the maximum pressure values differ even though they have been subjected to the same magnitude of axial stretch and the same residual stress field.

The results obtained for the model without azimuthal displacement restrictions are represented by the curve with a dashed line, whereas the curve with a continuous line represents the results of the model with azimuthal displacements restriction. The maximum inflation pressure in the latter curve is greater than the maximum inflation pressure reached in the model without azimuthal displacement restriction. In this last case, a first bifurcation is captured as it is presented by the first tendency change in the profile of the dashed line (associated with bending bifurcation), while the pressure values keep monotonically increasing in the continuous line. This indicates that bending is associated with the initial bifurcation and therefore that the onset of bifurcation is not bulging. Furthermore, bending bifurcation occurs when the dashed line remarkably changes its path and clearly separates from the behavior of the model represented by the solid line. The maximum point of the dashed line is associated with the formation of a bulge (after bending), which will be explained later in detail.

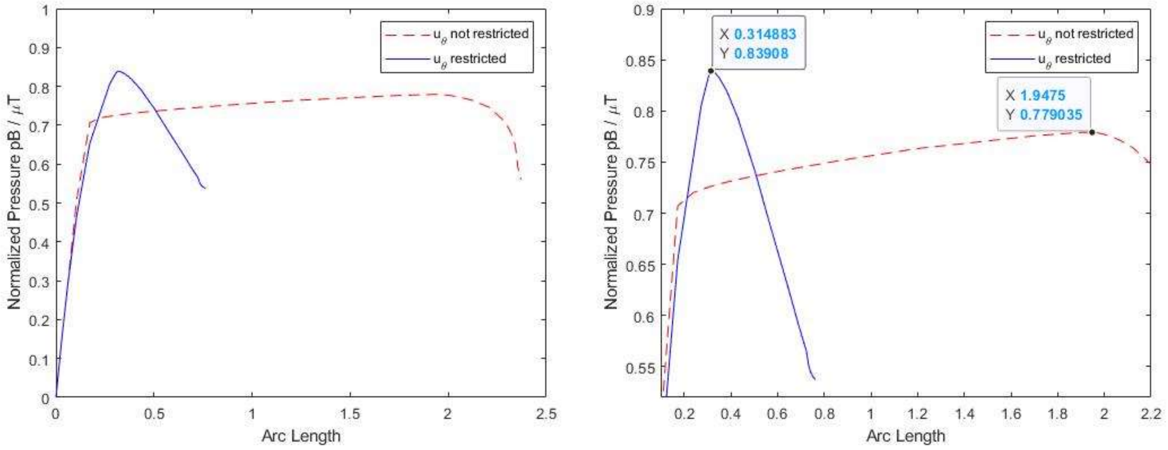

(a) (b)

Figure 4.10: (a) Values of normalized inflation pressure vs. Arc length for two models with $\overline{\alpha}_c = 0.5$, $f = 1$ and $\lambda_z = 1.08$. Azimuthal displacements are prevented to occur along the tube for the model represented by the continuous line (associated with bulging bifurcation), whereas they are not restricted for the model represented by the dashed line (associated with bending bifurcation). (b) Figure (a) showing the maximum pressure values.

For models in which bending fix the onset of bifurcation this is the expected behavior. It can be illustrated by the history of deformed configurations associated with the bending mode, depicted in Figure 4.11. Configurations (1) and (2) represent the cylinder at the beginning of loading and the onset of bending bifurcation, respectively. Subsequent post-bifurcation behavior is depicted by configurations (3) and (4), which show the bulging instability occurring after bending. It is to be noticed that a non-azimuthally symmetric bulge appears after bending bifurcation, which was previously anticipated by the profile of the dashed line shown in Figure 4.10. It is important to highlight that this bulge appears at a smaller pressure value than the pressure one associated with the onset of bulging when azimuthal displacements are restricted, which can also be appreciated in this last figure. Configuration (5) gives the end of the analysis.

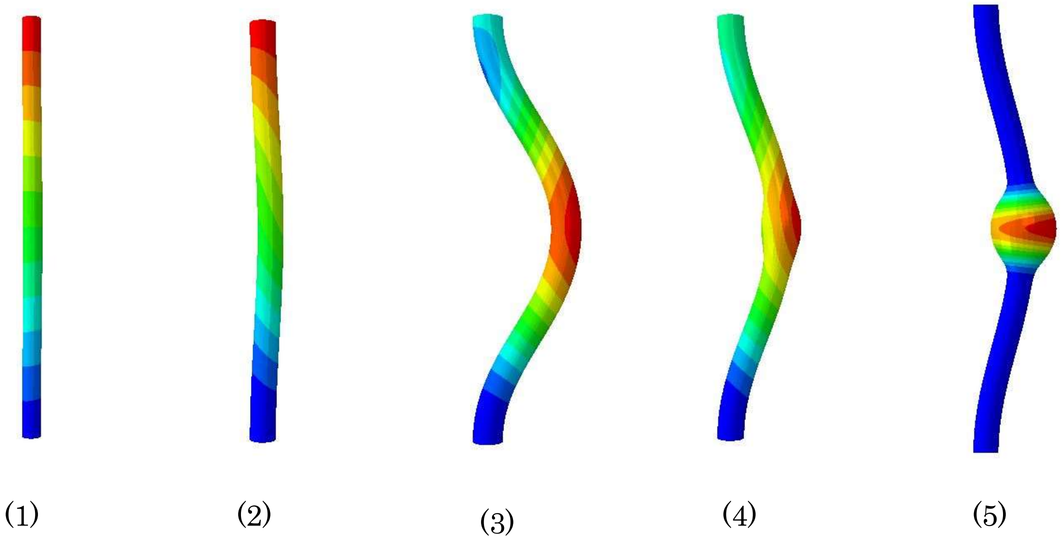

Figure 4.11: History of deformed configurations for a model with $\overline{\alpha}_c = 0.5$, $f = 1$ and $\lambda_z = 1.08$. (1) is the beginning of the analysis, (2) is the bending bifurcation, (3) gives further development of bending, (4) shows the irregularly shaped bulge and (5) is the end of the simulation.

On the other hand, for the simulation of the same model in which the azimuthal displacements along the tube length are restricted, the associated bifurcation mode is bulging. The history of deformed configurations for this simulation is depicted in Figure 4.12.

The initiation of the analysis with the application of internal inflation pressure is represented by configuration (1), bulging bifurcation takes place, which is associated with an axisymmetric displacement field and a radial propagation of the bulge ([13], [14]) (configurations (2), (3) and (4)).

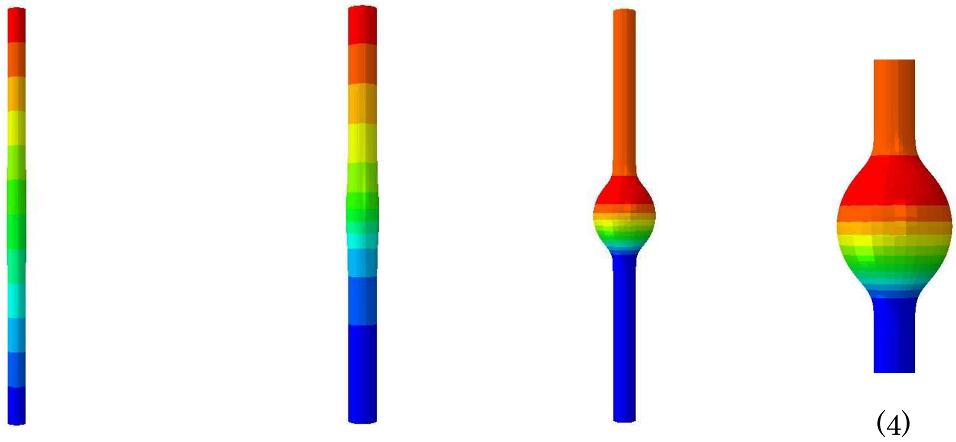

(1) (2) (3) (4)

Figure 4.12: History of deformed configurations for the case with $\overline{\alpha}_{\mathrm{c}} = 0.5$, $f = 1$ and $\lambda_z = 1.08$, with azimuthal displacements restricted (solid line in Figure 4.10), where (1) is the beginning of the analysis, (2) is the bulging bifurcation, (3) gives further development with radial expansion of the bulge, and (4) shows a zoomed picture of the bulge at the end of the simulation.

Based on several simulations which show the same behavior as the presented in the previous plots and as concluded in [21], it can be suggested that for small values of applied axial stretch the bifurcation mode for the models with the boundary conditions at hand is a bending buckling and not a localized axisymmetric bulging. In order to further develop on these results and to narrow down the expected bifurcation mode depending on the applied axial stretch, normalized inflation pressure values at the bifurcation are extracted for models with different axial stretch but subjected to the same residual stress field ($\overline{\alpha}_{\mathrm{c}} = 0.5$ and $f = 1$). As indicated at the beginning of this section, the values considered for the application of the axial stretch are in the range of $1 \leqslant \lambda z \leqslant 1.8$.

The analysis done through Figure 4.10 is extended to these two models by running two sets of simulations: one set with azimuthal displacements restricted along the tube, and another set without these displacements restriction, one simulation for each value of λ_z. Maximum pressure values are extracted from each simulation and plotted in Figure 4.13. Regarding to bending bifurcation, the instability point is set as the one for which the normalized pressure vs arc length curve dramatically changes its path and separates from the corresponding model with azimuthal displacements restricted, as identified in Figure 4.10.

In Figure 4.13 models with azimuthal displacements restricted along the tube are represented by the continuous line. The dot-dashed and dashed lines represent the inflation pressures at bending bifurcation and at bent-bulge formation after bending bifurcation, respectively. In this figure the three curves describe the two expected bifurcation modes (bending and bulging) and the post-bifurcation behavior (formation of the non-symmetrical bulge). The two set of simulations carried out have different behavior each other for the range of values of axial stretch $\lambda_z \approx [1, 1.18]$. For this range of values, bending bifurcation sets the instability mode (prior to bulging) for the models without azimuthal displacements restriction along the tube. This is clearly identified by the dot dashed line in Figure 4.13 as the pressure values are lower than for the two other curves. If azimuthal displacements are restricted along the tube, then the incremental displacement field is of the form of (3-31) and bulging mode impose over bending.

Furthermore, the normalized inflation pressure values associated with the formation of the non-azimuthally symmetric bulge at the post-bifurcation behavior show that they are lower than the pressure values related to the simulations in which azimuthal displacements are restricted and just bulging bifurcation is obtained. For sufficiently large values of axial stretch (approximately 1.16-1.18), the simulations align and exhibit equal results showing that bulging bifurcation is the expected instability mode. It follows that for sufficiently large values of applied axial stretch the bulging mode is the one which sets the bifurcation and the post-bifurcation behavior.

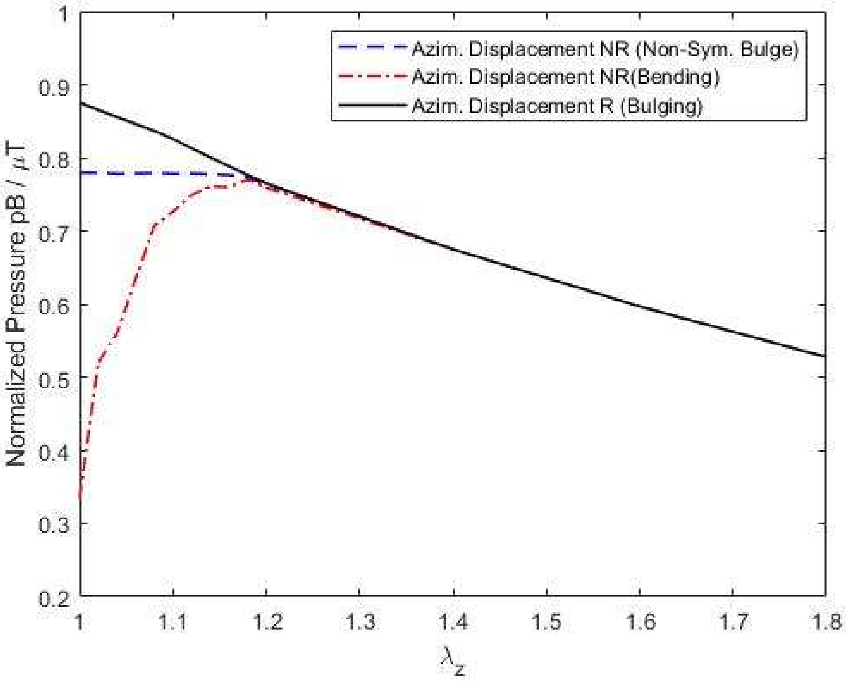

Figure 4.13: Normalized inflation pressure at the bifurcation vs axial stretch λ_z for the case with $\overline{\alpha}_c = 0.5$ and $f = 1$. The dot-dashed line represents pressures at bending bifurcation, while the dashed line represents pressures at post-critical behaviour corresponding with the formation of a non-symmetrical bulge, which is consistent with the development of abdominal aortic aneurysms (AAA). The continuous line represents models with azimuthal displacements restricted along the tube, in which bulging mode imposes over bending for $\lambda_z \approx [1, 1.8]$.

Figure 4.14: Contours plot for a model with $\overline{\alpha}_c = 0.5$, $f = 1$ and $\lambda_z = 1.40$ showing a bulge at the post-bifurcated shape, which is the expected bifurcation mode for this level of axial stress.

Although it is an approximation, the moment equilibrium for a membrane can be used to analyze the expected bifurcation mode for each simulation and the previous results have just validated this criterion. As it was shown in Figure 4.9 the values of $\mathcal{M} = \sigma_{\theta\theta} - 2\sigma_{zz}$ suggested that for a model with a low value of axial stretch the onset of bifurcation could be related to a bending instability.

In Figure 4.15 average stress values of $\sigma_{\theta\theta}$ and σ_{zz} are presented for a model with $\overline{\alpha}_c = 0.5$, $f = 1$ and $\lambda_z = 1$. Profiles of the curves show the average stresses along the tube length just before the bifurcation, which in the simulation is bending (see Figure 4.16). Subsequently, if these values of stress are plot as $\mathcal{M} = \sigma_{\theta\theta} - 2\sigma_{zz}$, as shown in Figure 4.17, all values are $\mathcal{M} > 0$, suggesting that bending bifurcation is expected to occur in this simulation. It is recalled that as it was presented by the dashed line in Figure 4.9, negative values of $\mathcal{M}$ can also be obtained. By repeating this process for each simulation carried out with the different axial stretch values in the range of $\lambda_z = [1, 1.8]$ and taking out the maximum (or minimum) values of $\mathcal{M}$, the Figure 4.18 can be drawn.

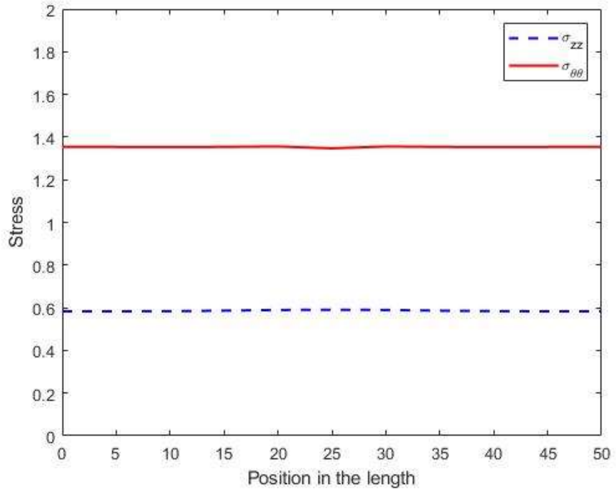

Figure 4.15: Average values of stress $\sigma_{\theta\theta}$ and σ_{zz} just before bifurcation time for each cross-section along the tube longitudinal axis, for a model with value of $\lambda_z = 1.0$, $\overline{\alpha}_c = 0.5$ and $f = 1$ (I_5 invariant).

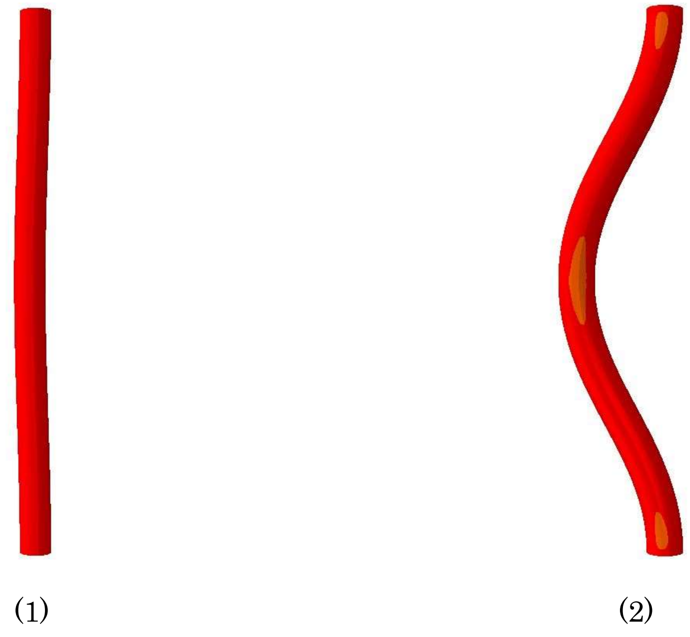

Figure 4.16: Bending deformation patterns for simulation with $\overline{\alpha}_c = 0.5$, $f = 1$ and $\lambda_z = 1.0$.

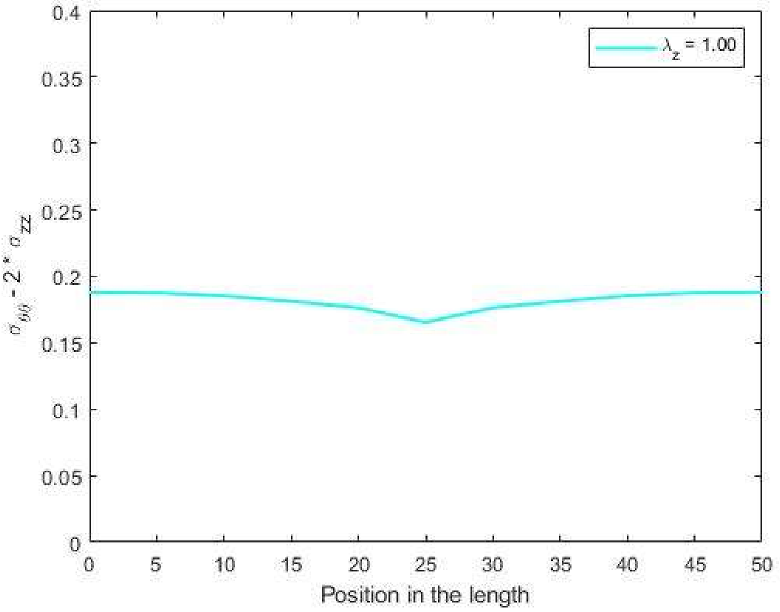

Figure 4.17: Bending condition $\mathcal{M} = \sigma_{\theta\theta} - 2\sigma_{zz}$ for a model with $\lambda_z = 1.0$, $\overline{\alpha}_c = 0.5$, and $f = 1$ (I_5 invariant).

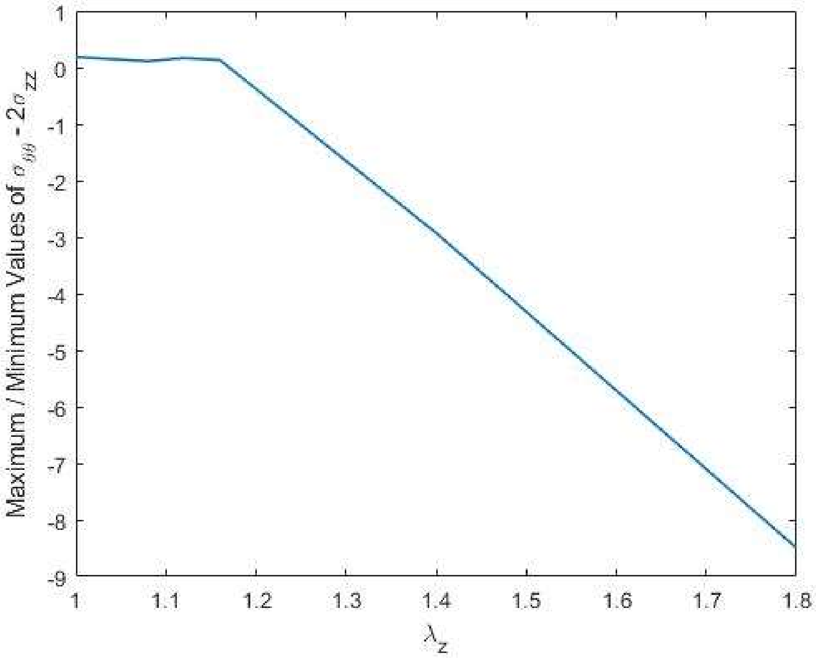

Figure 4.18: Maximum values of $\mathcal{M} = \sigma_{\theta\theta} - 2\sigma_{zz}$ against axial stretch for case with $\overline{\alpha}_c = 0.5$ and $f = 1$. Positive values suggests that the onset of bifurcation is associated with bending instability, whereas negative values indicates that bending bifurcation is not expected and thus, that bulging may give the onset of bifurcation.

This last figure follows a similar shape as Figure 4.13, and shows a very important result as it provides a general picture about the expected bifurcation mode for each simulation, each one of them run for a specific value of axial stretch. It is anticipated that for small values of axial stretch the bifurcation mode is related to bending prior to bulging instability, whereas for sufficiently large values of axial stretch bulging gives the onset of bifurcation.

5. Computational Bifurcation Analysis for Thick-Walled Circular Cylindrical Tubes with the Influence of a Three-Dimensional Residual Stress Field

5.1. Introduction

The initial stress imposed in previous analyses was a plane one independent of the axial position (axial coordinate) inside the tube and, furthermore, there was no residual shear stress. In addition, the axial stretch is regarded as a given constant for the tube at hand. It follows that bulging initiation can be analyzed but the position of the bulge along the axial direction cannot be studied. Under those conditions, since a planar state for the residual stress field was adopted, the position of the bulge is independent of the altitude in the given tube.

In this chapter, it is analyzed the effect of a 3-D residual stress field on bifurcation of a cylindrical tube under extension and inflation. It is built upon the phenomenological (plane) model outlined in [41] (and used in the previous chapter) and include now axial and shear components for the residual stress tensor. During the analysis the magnitude of the axial stretch is also considered a constant but the dependence of the residual stress field on the altitude of the tube makes it possible to locate the bulge in different positions along the tube axis.

Following [21] and the methodology presented in previous chapters, the finite element method (FEM) is used. This means that it is employed the built-in arc length procedure of Abaqus in which the solution is controlled using the so-called arc length parameter. Based on the previous discussion, one of the goals of this section is to strengthen the constitutive formulation that includes a prescribed residual stress field within the conventional hyperelastic framework.

For avoidance of being repetitive, some of the chapter's sections present summarized information and they are organized as follows. Residual stress is provided in Section 5.2, the numerical procedure is summarized in section 5.3 and the numerical results are presented in section 5.4.

The dependence of bifurcation of hyperelastic tubes under the described loading on residual stresses is illustrated and compared with results when there is a planar or no residual stress. Results highlight the effects of the 3D residual stress. Three effects are important. Firstly, for sufficiently small values of the axial stretch bending is the onset of bifurcation. This was already concluded from the results of the previous chapter, but it is demonstrated here including more numerical results. On the other hand, for sufficiently large values of the axial stretch bulging gives the onset of bifurcation. Secondly, regardless of the axial stretch the location of the bulge along the length of the tube is affected by the axial stress component of the residual stress. Values of compression of this component at the outer boundary, together with values of traction at the inner boundary, of the middle cross sections of the tube are related with bulges at the ends of the tube regardless of the value of the axial stretch. Conversely, values of traction of this component at the outer boundary, together with values of compression at the inner boundary, of the middle cross sections of the tube are associated with the development of a bulge at the middle of the tube, in line with cases with planar residual stresses or no residual stress since in these cases there is no dependence on the altitude of the tube. Thirdly, by analyzing various models it has been shown that the inflation pressure associated with bifurcation is qualitatively affected by both the axial stretch and the residual stress field. As the axial stretch increases, the inflation pressure associated with bifurcation decreases more rapidly for cases with a non-planar residual stress field in the strain energy function of the material than for cases without this residual stress field.

5.2. Residual Stress Field

In [21] a plane residual stress tensor with just non-zero components σ_{0RR} and $\sigma_{0\Theta\Theta}$ was considered assuming no dependence on Θ. Even though there are no reliable data on residual stresses in aneurysms it was pointed out in [10] that those expressions considered in [21], which are the ones presented in section 4.2 are consistent with residual stresses arising from the opening angle method ([11]). Based on those results, it is adopted the following stress tensor (on a cylindrical system):

$$\begin{aligned}
\sigma_{0RR} &= \alpha_c(R - A)(R - B) \\
\sigma_{0R\Theta} &= 0 \\
\sigma_{0RZ} &= \frac{\alpha_d}{R}\left[(R - A)(R - B)(4Z^3 - 6Z^2L + 2ZL^2)\right] \\
\sigma_{0\Theta\Theta} &= \alpha_c\left[3R^2 - 2(A + B)R + AB\right] + \alpha_d\left[(R - A)(R - B)(12Z^2 - 12ZL + 2L^2)\right] \\
\sigma_{0\Theta Z} &= 0 \\
\sigma_{0ZZ} &= \frac{-\alpha_d}{R}\left[(2R - A - B)(Z(L - Z))^2\right]
\end{aligned} \tag{5-1}$$

It is easy to check that this tensor satisfies the conditions to be considered a residual stress tensor. The coefficients α_c and α_d can be also expressed in normalized form by taking $\alpha_c = \mu\bar{\alpha}_c / 2BT$ and $\alpha_d = \mu\bar{\alpha}_d / 2L^4$, respectively. The strength of the residual stresses is then controlled by the non-dimensional parameters $\bar{\alpha}_c$ and $\bar{\alpha}_d$.

In the previous chapter, it was considered that $\alpha_d = 0$, as equation (4-1) describes a plane residual stress field in which the only non-zero components of the residual stress tensor (σ_{0RR} and $\sigma_{0\Theta\Theta}$) depended only on R. Now, according to the residual stress field given by the expressions in (5-1), there is dependence on both R and Z. Therefore, one of the goals of the present stress distribution is to incorporate in the constitutive framework the dependency along the Z direction, which also gives rise to shear stress components.

The analyses done will also be focused on tubes for which the length is much greater than its radius. Recalling from section 3.4.1, a cylindrical tube with ratio $\frac{T}{D} = 0.05$, with length L = 50, diameter D = 2.5 and thickness T of 0.125 is considered for all the simulations to be carried out. To obtain a qualitative behavior of the residual stress field, plots of the different components of the residual stress tensor are shown in Figure 5.1 for different values of $\bar{\alpha}_c$ and $\bar{\alpha}_d$. In particular, in Figure 5.1, (a) to (c) are for the case with $\bar{\alpha}_d = 40$ and $\bar{\alpha}_c = 0.5$, (d) to (f) are for the case with $\bar{\alpha}_d = -40$ and $\bar{\alpha}_c = 0.5$ and (g) is for the case with $\bar{\alpha}_d = -40$ and $\bar{\alpha}_c = -0.5$. Values of $\sigma_{0\Theta\Theta}$ in Figure 5.1 (b), (e) and (g) are for $Z = L/2$. It is important to remark that $\sigma_{0\Theta\Theta}$ depends on both R and Z, but it should be noted the term multiplying α_d in $\sigma_{0\Theta\Theta}$ is zero for $R = B$ (also for $R = A$) regardless of the value of Z. Furthermore, for a given R, $\bar{\alpha}_d$ and $\bar{\alpha}_c$, the values of $\sigma_{0\Theta\Theta}$ are indistinguishable for any Z. For that reason, $\sigma_{0\Theta\Theta}$ in Figure 5.1 (b), (e) and (g) are shown for $Z = L/2$. Values of stresses are normalized with respect to the material constant $\mu/2$ in all cases.

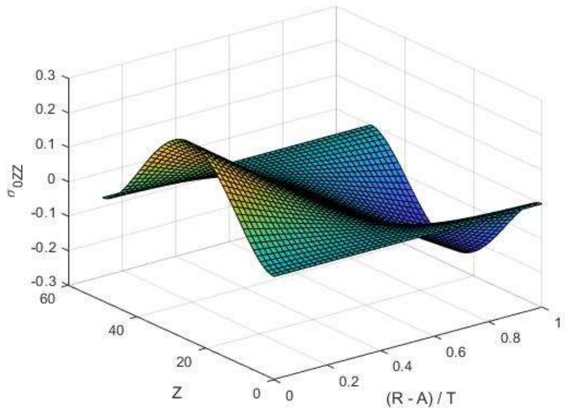

(a) σ_{0Z} for $\bar{\alpha}_d = 40$ and $\bar{\alpha}_c = 0.5$

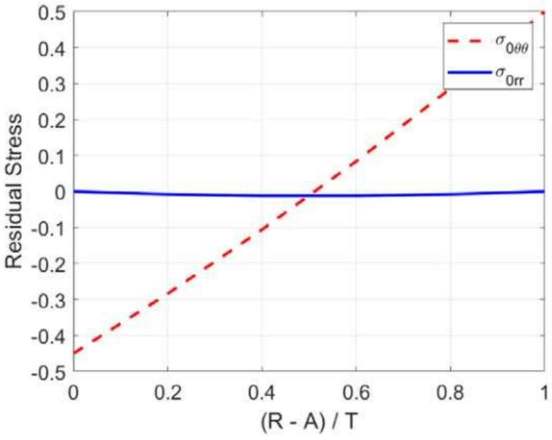

(b) $\sigma_{0\Theta\Theta}$ and σ_{0RR} for $\bar{\alpha}_d = 40$ and $\bar{\alpha}_c = 0.5$

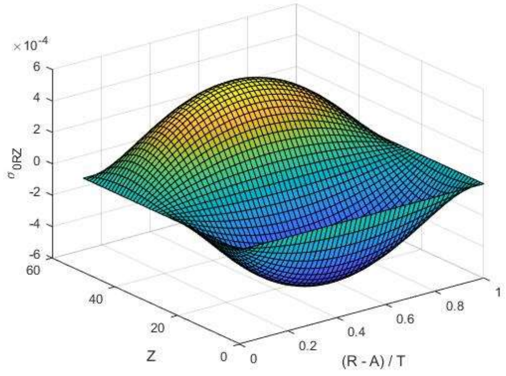

(c) σ_{0RZ} for $\bar{\alpha}_d = 40$ and $\bar{\alpha}_c = 0.5$

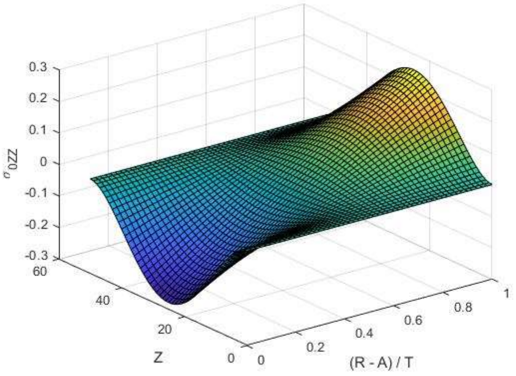

(d) σ_{0ZZ} for $\bar{\alpha}_d = -40$ and $\bar{\alpha}_c = 0.5$

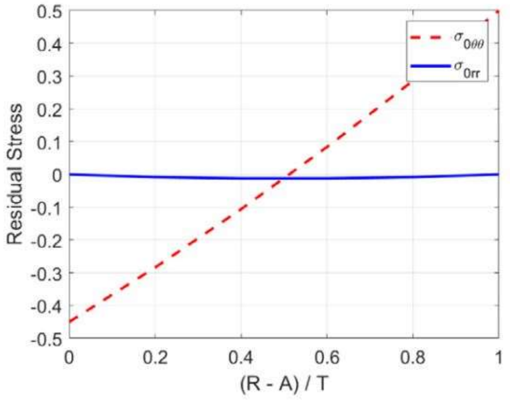

(e) $\sigma_{0\Theta\Theta}$ and σ_{0RR} for $\bar{\alpha}_d = -40$ and $\bar{\alpha}_c = 0.5$

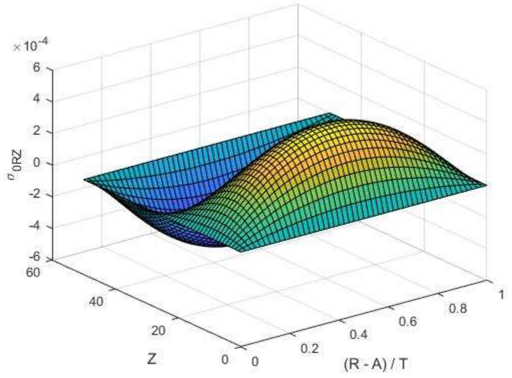

(f) σ_{0RZ} $\bar{\alpha}_d = -40$ and $\bar{\alpha}_c = 0.5$

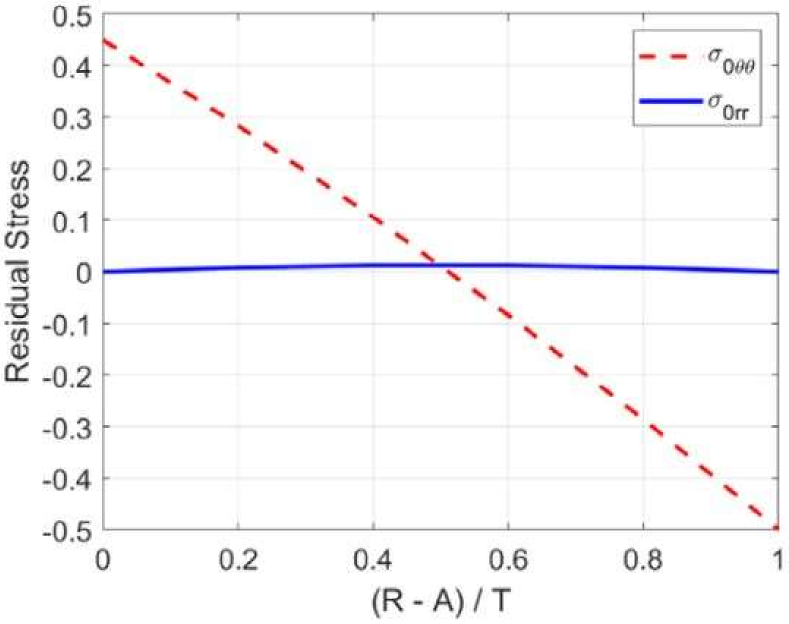

(g) $\sigma_{0\Theta\Theta}$ and σ_{0RR} for $\bar{\alpha}_d = -40$ and $\bar{\alpha}_c = -0.5$

Figure 5.1: Plot of the different components of the residual stress against the axial direction Z and the normalized thickness $\frac{(R-A)}{T}$ where A is the internal radius: (a) to (c) are for the case with $\bar{\alpha}_d = 40$ and $\bar{\alpha}_c = 0.5$, (d) to (f) are for the case with $\bar{\alpha}_d = -40$ and $\bar{\alpha}_c = 0.5$, and (g) is for the case with $\bar{\alpha}_d = -40$ and $\bar{\alpha}_c = -0.5$.

It should also be pointed out that the radial component of stress σ_{0RR} is only affected by α_c while σ_{0RZ} and σ_{0ZZ} are only affected by α_d. The azimuthal stress component $\sigma_{0\Theta\Theta}$ is affected by both α_c and α_d. Comparing Figure 5.1 (c), for instance, with Figure 5.1 (a) and (b), it is clear that the order of magnitude of the stress values for σ_{0R} (10^{-4}) is much smaller than the order of magnitude of the other stress components. In addition, the considered values of $\bar{\alpha}d$, either positive or negative, have very little effect on the numerical values of $\sigma_{0\Theta\Theta}$. It follows that the values of $\sigma_{0\Theta\Theta}$ in figures (b) and (e) are practically identical.

The value of $\sigma_{0\Theta\Theta}$ is also affected by α_c. It can be appreciated that values of $\sigma_{0\Theta\Theta}$ in Figure 5.1 (b) are just the negative ones of Figure 5.1 (g). Note also that σ_{0RZ} and σ_{0Z} change sign with the sign of $\bar{\alpha}d$ while σ_{0R} and $\sigma_{0\Theta\Theta}$ change sign with the sign of $\bar{\alpha}c$. Regarding to σ_{0ZZ} it is shown by Figure 5.1 (a) that values of compression of this component at the outer boundary, together with values of traction at the inner boundary, of the middle cross sections of the tube are related with values of $\bar{\alpha}_d > 0$. Conversely, values of traction of this component at the outer boundary, together with values of compression at the inner boundary, of the middle cross sections of the tube are related with values $\bar{\alpha}_d < 0$, see Figure 5.1 (d). Finally, it is remarked the symmetry of the residual stress field along the length of the tube with respect to the middle cross section, as it is shown for the different components of stress. It follows that as loading is applied the deformation of the tube is expected to maintain a similar pattern with respect to the middle cross section of the tube.

5.3. Numerical Procedure

The numerical procedure in Abaqus is basically equal to the presented in section 4.3. In this section, it is briefly presented as it was already detailed there. The analysis captures the deformation of an inflated cylindrical tube under various axial stretches, characterized by λ_z, and different residual stress fields characterized by the parameters $\bar{\alpha}_c$ and $\bar{\alpha}_d$. Unlike the residual stress field presented in the previous chapter, the residual stress in the axial direction is nonzero. Additional to the deformation, stresses inside the tube are also computed. The current framework is implemented into the general-purpose FE package Abaqus using the user-defined material routine UMAT in combination with SDVINI for the insertion of the residual stress field. The finite element model employs the so-called hybrid elements to prevent locking pathologies and to account for material incompressibility behavior. The reader is referred to ([15], [41]) for further details on the numerical implementation in compact form, and to [44] for further details on the hybrid formulation implementation in Abaqus.

Each numerical simulation is carried out in three steps (the word Step refers to the analysis steps carried out in Abaqus) as follows:

In the first step of the simulation, residual stresses are introduced into the model. It is recalled that, after running several simulations and sensitivity analyses, the residual stress parameters that control the magnitude of these stresses were chosen such that they are neither very high to take the model near any instability nor very low to have negligible effects. These parameters values are set as $\bar{\alpha}_d \in \{-40,\ 0,\ 40\}$ and $\bar{\alpha}_c \in \{0.5, 0, -0.5\}$. It should be noted that the values of $\bar{\alpha}_c$ are the same as presented in the previous chapter. Figure 5.2 shows the Von Mises stress contour plot at the middle section of a cylinder whereas Figure 5.3 shows the axial stress σ_{0ZZ} distribution along the length of the cylinder at the end of this first step, which agrees with the ones given in Figure 5.1 (a).

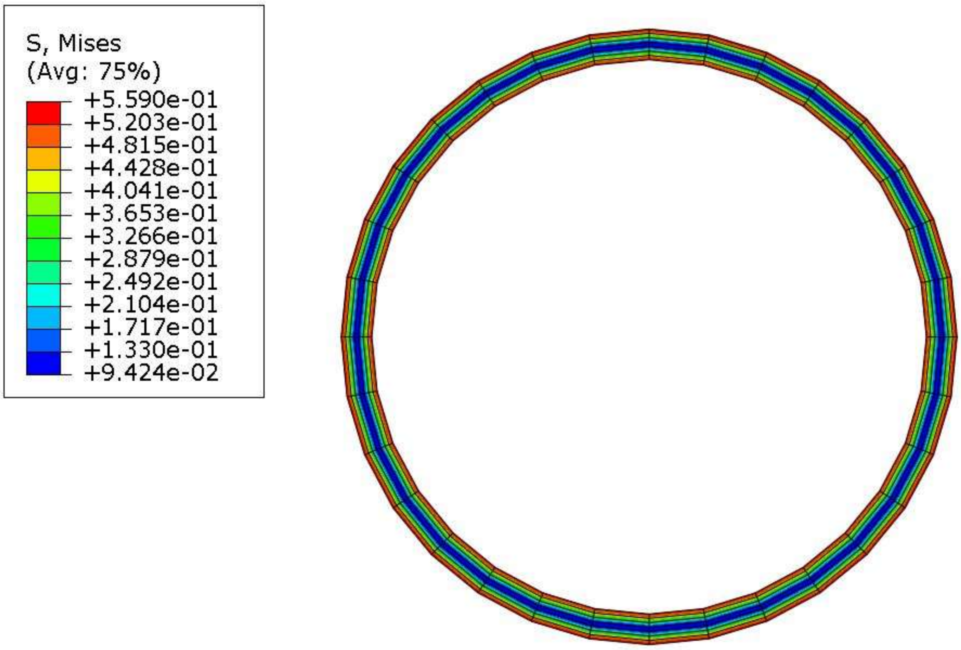

Figure 5.2: Typical contour plot of Von Mises stress derived from applying the three-dimensional residual stress field, shown at the middle section of the tube

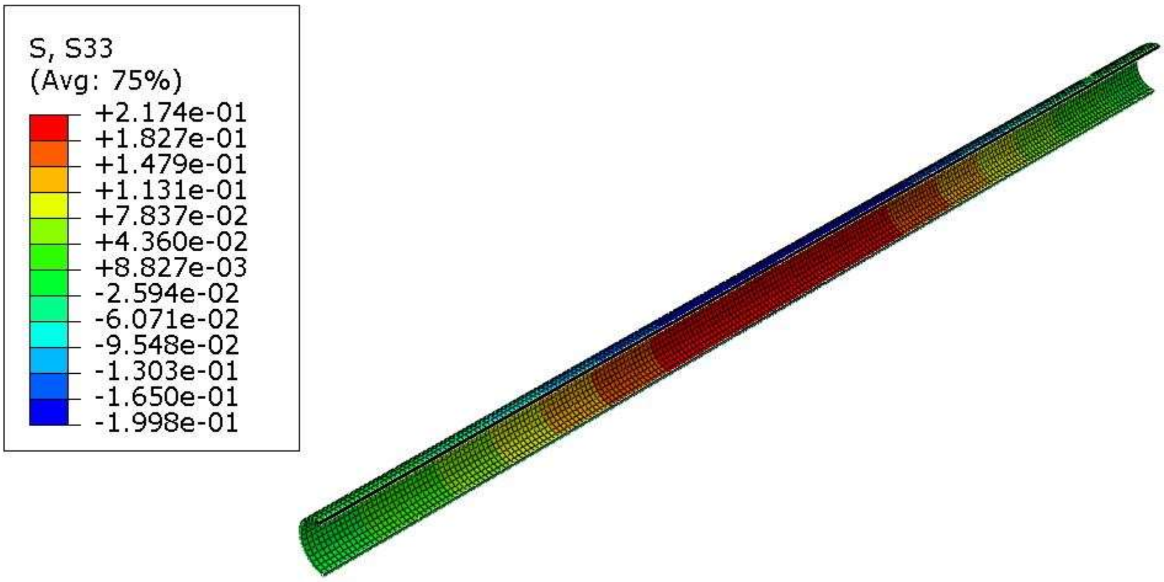

Figure 5.3: Contour plot of σ_{0Z} showing its distribution in the body of the model with $\bar{\alpha}_d = 40$ and $\bar{\alpha}_c = 0.5$, which agrees with the analytical plot of this stress shown in Figure 5.1 (a).

In the second step, the axial stretch is applied imposing axial displacements at one end while keeping zero axial displacements at the other end. At both ends hoop displacements are prevented during the first and the second analysis step. In the last step, the internal pressure of magnitude p = 10 μ T/D is applied on the inner surface of the cylinder using the modified Riks analysis procedure. In this last step, hoop and axial displacements are restricted at both ends of the tube. Additionally, if the aim is to capture bulging bifurcation, hoop displacements should be prevented along the tube length during the three steps. On the contrary, if the aim is to capture the bifurcation mode that is first triggered, no restrictions along the tube length should be imposed.

Regarding capturing or identifying the bifurcation points, the methodology set in section 4.3 can also be followed and applied for these analyses. By summarizing the procedures exposed in that section, the following can be said:

- For bulging bifurcation: the azimuthal stretch of two points (one inside and another outside the bulge) can be followed, bulging bifurcation point is determined when the values of these diverge by 1% or 2% from their average value (see Figure 4.7 (b)).

- For bending bifurcation: various verifications can be done. The first one is to follow the analytical bending stability condition for a membrane $\mathcal{M} = 0$ as stated in section 2.2.3. This criterion is implemented aiming at identifying the expected bifurcation mode. Additionally, a combined azimuthal and radial displacement taking the tube's cross-sections out of its longitudinal axis can be followed to identify a lateral movement, characteristic of a bending buckling. As it has been stated in section 4.3, the profile of the normalized inflation pressure vs Arc Length curve of a model with an axial stretch for which bending bifurcation is expected to set the primary bifurcation mode shows a characteristic path with a clear proportional limit (point A in the continuous profile of Figure 5.4) from which the evolution of the deformation starts to increase rapidly as loading keeps increasing, but with a stiffness loss. This point is related to the onset of bending bifurcation captured in the corresponding simulation. The other curve profile is given from a simulation for the same model, but in which the azimuthal displacements have been restricted along the tube length (dashed line). This restriction avoids any lateral displacement to occur yet allowing the tube to inflate under perfectly circular cross-section configurations. It can be appreciated how the dashed line surpasses point A, and the loading continues monotonically increasing until point C, which shows a maximum related to bulging bifurcation mode. The proportional limit A is the point from which the two models diverge and can be set as the bending bifurcation point. Point B is related to the occurrence of bulging after bending with an irregular shape, which will be treated later in detail.

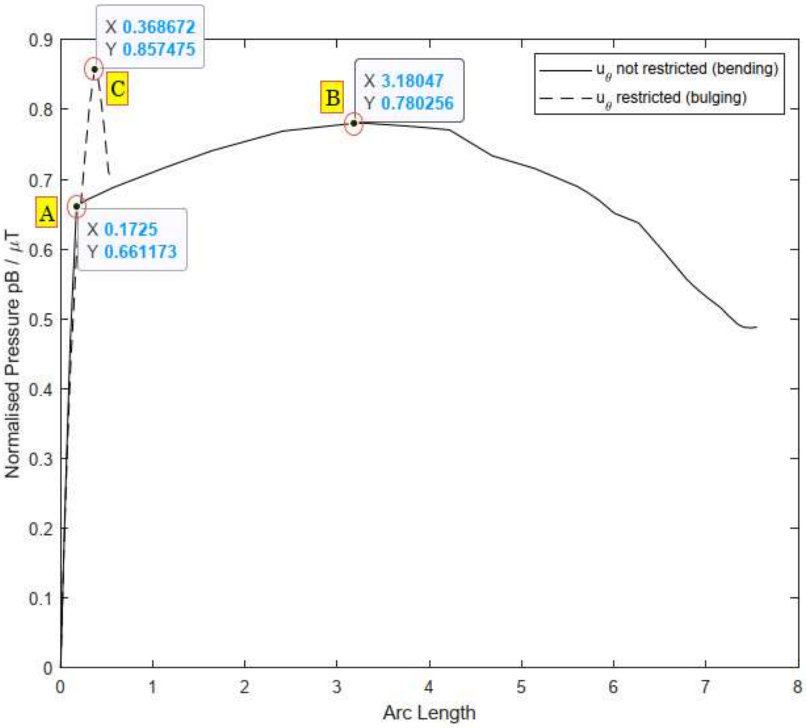

Figure 5.4: Normalized inflation pressure against Arc Length for two models with $\lambda_z = 1.08$, with the following conditions: (a) a model with azimuthal displacements restricted along the tube length (dashed line) and (b) a model with azimuthal displacements allowed along the tube length (continuous line).

5.4. Numerical Results

In this section, numerical results are presented for the cases analyzed, which have different values of residual stress constitutive parameters, see Table 5.1. The model behavior representing each case is studied for different values of axial stretch and applied internal pressure. Axial stretches considered are defined in the range of $1 \leqslant \lambda z \leqslant 1.8$. Results show different stress components, and their values are normalized with respect to the material constant $\mu/2$.

CASE-I5, I6	$\bar{\alpha}_d$	$\bar{\alpha}_c$
1	40	0.5
2	40	-0.5
3	-40	0.5
4	-40	-0.5
5	40	0
6	-40	0
7	0	0
8	0	0.5
9	0	-0.5

Table 5.1: Values of residual stress constitutive parameters for the different numerical simulations

In order to identify bifurcation conditions, it is followed among other aspects the conditions associated for a membrane as it has been described in section 2.2.3. The numerical results show that the onset of bifurcation is either bulging or bending and the mode of instability (bending or bulging) depends mainly on the axial stretch of the cylinder. Furthermore, the onset of bending is associated with the mode m=1.

The cases in Table 5.1 are identified by either CASE-I5 or CASE-I6 to identify the invariant (I_5 or I_6) that is being considered. Focusing on the strain energy density function defined by (3-32) to distinguish the two bifurcation scenarios, the following description can be given. Consider CASE-I6 1 in Table 5.1 and two simulations: (i) one with $\lambda_z = 1$ and (ii) other with $\lambda_z = 1.4$. Values of $\sigma_{\theta\theta} - 2\sigma_{zz}$ vs arc length are plotted in Figure 5.5 to get a first approximation of the bifurcation scenario in each computation. The values $\sigma_{\theta\theta} - 2\sigma_{zz}$ are average stresses of the tube middle cross-section. For simulation (ii), i.e. $\lambda_z = 1.4$, Figure 5.5 also shows that $\sigma_{\theta\theta} - 2\sigma_{zz} < 0$ (solid line), which can be taken as a sign that bending is not expected to give the onset of bifurcation. In fact, the numerical solution gives bulging. On the other hand, in Figure 5.5 there are values obeying $\sigma_{\theta\theta} - 2\sigma_{zz} = 0$ for simulation (i), dashed line. This gives an indication that bending may give the onset of bifurcation although this is not enough to establish the bifurcation scenario.

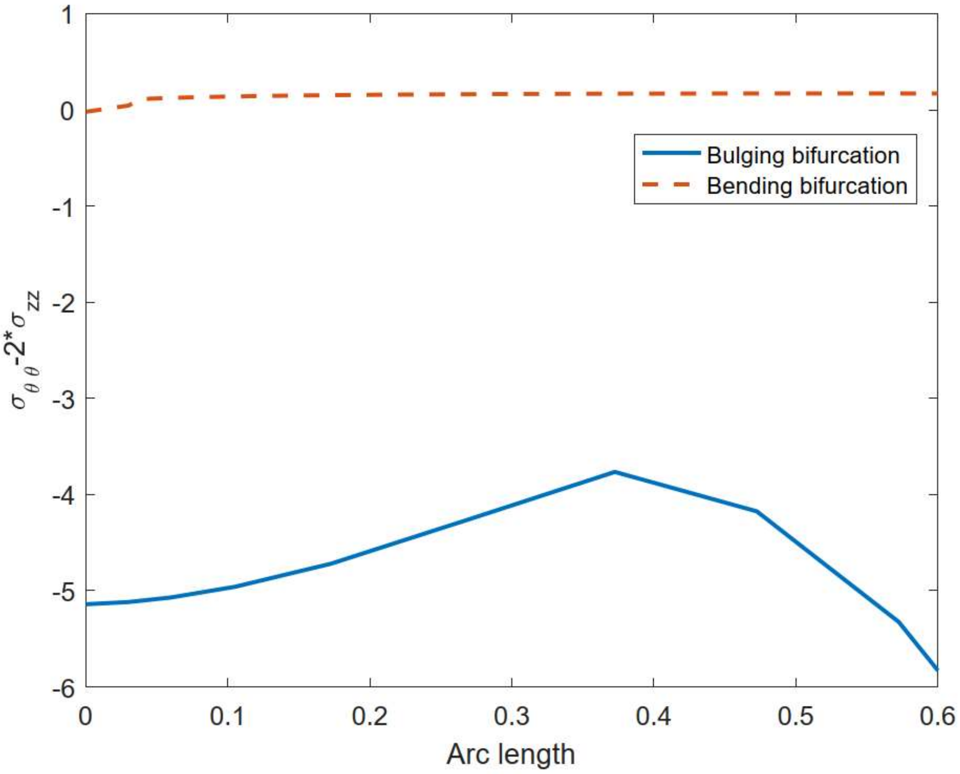

Figure 5.5: Values of $\sigma_{\theta\theta} - 2\sigma_{zz}$, where stresses are average stresses of the tube middle cross-section vs arc length for CASE-I6 1 with $\lambda_z = 1$, dashed line, and with $\lambda_z = 1.4$, solid line. For the former case, the curve shows values obeying $\sigma_{\theta\theta} - 2\sigma_{zz} > 0$, which indicates that bending may be the associated onset of bifurcation. On the other hand, for the latter case the curve shows that $\sigma_{\theta\theta} - 2\sigma_{zz} < 0$, which indicates that bending bifurcation mode is not expected under these conditions and furthermore that bulging is the onset of bifurcation.

Thus, attention is turned to the following procedure explained in the previous section of this chapter. Values of normalized inflation pressure vs Arc Length for simulation (i) are shown in Figure 5.6, dashed line. Additionally, as it is explained in the previous section one can restrict the analysis to capture just bulging and the simulation (i) is considered under those circumstances. The corresponding values of normalized inflation pressure vs Arc Length for this simulation are also shown in Figure 5.6, continuous (solid) line. As it was indicated in the previous section bending is associated with initial bifurcation for simulation (i), and therefore the onset of bifurcation is not bulging. The maximum point of the dashed line is associated with the formation of bulging (after bending). The dashed curve behavior is consistent with deformed shapes in Figure 5.7.

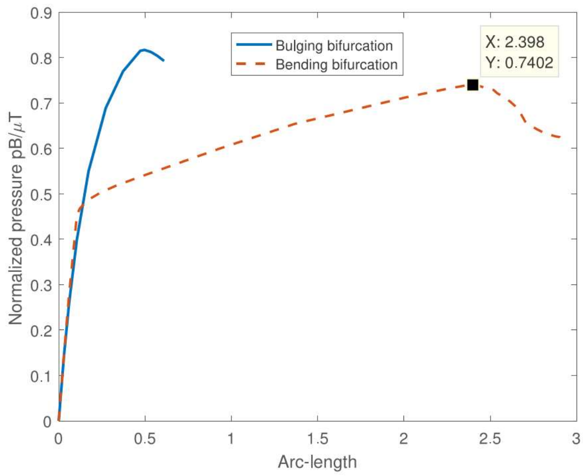

Figure 5.6: Values of normalized inflation pressure vs Arc Length for CASE-$_{\text{I6}}$ 1 with $\lambda_z = 1$ under two simulations: (a) the continuous line is for a simulation that does not allow azimuthal displacements and therefore is restricted to capture just bulging and (b) the dashed line is for a simulation without that restriction (incremental displacements described by Eq. (3-29)) and bending is captured. The onset of bending bifurcation is identified when the two curves separate. The maximum point of the dashed line is associated with the formation of one-sided bulges after bending. This means that the structure after bending can resist more loading until the onset of bulging. The maximum point in both curves is associated with bulging bifurcation and is catastrophic because the structure does not support more loading.

History of deformed configurations associated with the bending mode is depicted in Figure 5.7, including bifurcation and post-bifurcation. Configurations (1) and (2) represent the cylinder at the beginning of loading and the onset of bending bifurcation, respectively. Subsequent post-bifurcation behavior is depicted by configuration (3) and (4), which shows the bulging instability occurring after bending. It is to be noticed that two non-azimuthally symmetric bulges appear after bending bifurcation, which was previously anticipated by the profile of the dashed line shown in Figure 5.6. It is important to highlight that these bulges appear at a smaller pressure value than the pressure one associated with the onset of bulging when azimuthal displacements are restricted, which can be also appreciated in Figure 5.6. Configuration (5) gives the end of the analysis.

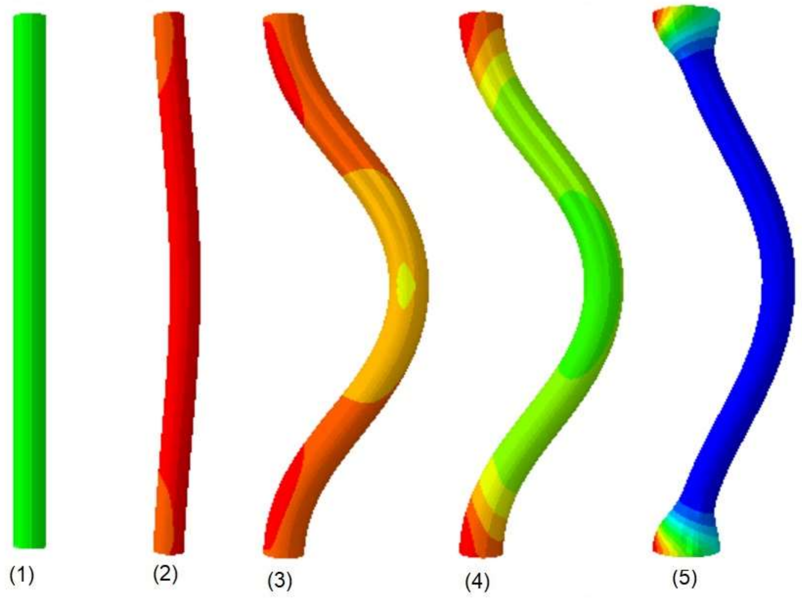

Figure 5.7: History of deformed configurations for CASE-I6 1 with $\lambda_z = 1$ and no azimuthal displacement restrictions (dashed line in Figure 5.6), where (1) is the beginning of the analysis, (2) is the bending bifurcation, (3) gives further development of bending, (4) shows the irregularly-shaped bulge and (5) is the end of the simulation.

The previous simulation has shown that two bulges can appear. On the other hand, for a simulation with parameters from CASE-I6 3 in Table 5.1 with $\lambda_z = 1.4$ is associated with bulging and only one bulge appears. The history of deformed configurations for this simulation is depicted in Figure 5.8. The initiation of the analysis with the application of internal inflation pressure is represented by configurations (1) and (2), bulging bifurcation takes place, which is associated with an axisymmetric displacement field and a radial propagation of the bulge [14] (configurations (3), (4) and (5)).

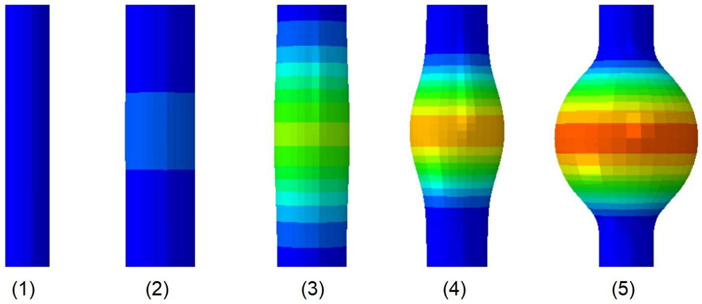

Figure 5.8: History of deformed configurations for CASE-I6 3 in Table 5.1 with $\lambda_z = 1.4$, where (1) is the beginning of the analysis and (3) is the bulging bifurcation; (4) and (5) show post-bifurcation behaviour.

In view of these results, attention turns to the analysis of the location of the bulge along the length of the tube. The next set of results concerns to the model given by CASE-I6 1 in Table 5.1. Firstly, it is worth noting that bending bifurcation is not expected to occur for this model with axial stretch $\lambda_z = 1.4$, as it is suggested by the profile of the solid line in Figure 5.5 since $\mathcal{M} < 0$. In order to analyse this latter condition, average values of $\sigma_{\theta\theta}$ and σ_{zz} are plotted in Figure 5.9 (a) for each cross section along the length of the tube prior to the occurrence of the structural instability, which is bulging. The distribution of stresses shows that higher values of azimuthal and axial stresses develop at both ends, and that bulges develop at both ends of the tube. This profile of stresses distribution with maximum stresses values at the ends of the cylinder is maintained for models with $\bar{\alpha}_d > 0$.

This can be seen by comparing Figure 5.9, Figure 5.10, Figure 5.11 and Figure 5.12. For the model given by CASE-I6 3 in Table 5.1 with axial stretch $\lambda_z = 1.4$, Figure 5.9 (b) depicts the distribution of azimuthal and axial stresses along the cylinder length prior to bifurcation, which is bulging. Analyzing this graph, it is identified that the maximum values are located at the central region of the cylinder, and the bulge develops at this last location (see Figure 5.9 (d)). This case has a negative value of $\bar{\alpha}_d$. It seems that with the change of the sign of $\bar{\alpha}_d$, the bulge location can be shifted either at the middle or at both ends of the cylinder. It is recalled that for a positive value of $\bar{\alpha}_d$, the axial residual stress component σ_{0ZZ} is shown by Figure 5.1 (a), and it introduces values of axial compression at the outer boundary, together with values of axial traction at the inner boundary, of the middle cross sections of the tube. On the contrary, values of traction of this component at the outer boundary, together with values of compression at the inner boundary, of the middle cross sections of the tube are related with values $\bar{\alpha}_d < 0$ (see Figure 5.1 (d)).

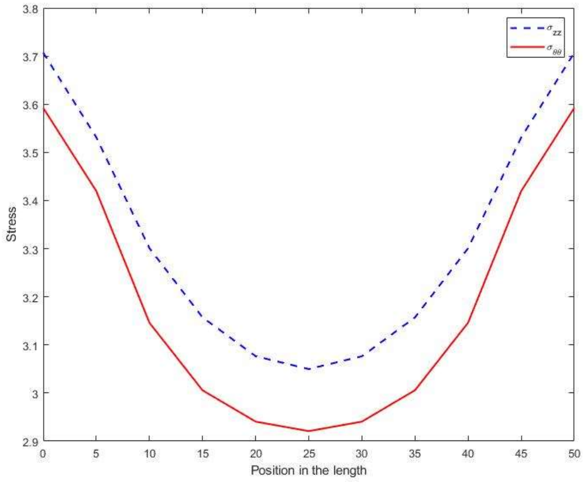

(a) Values of axial and azimuthal average stresses on the cross-sections along the tube length for $\bar{\alpha}_d = 40, \bar{\alpha}_d = 0.5$ and $\lambda_z = 1.4$ just before bulging. Maximum values at both ends of the cylinder where bulges appear.

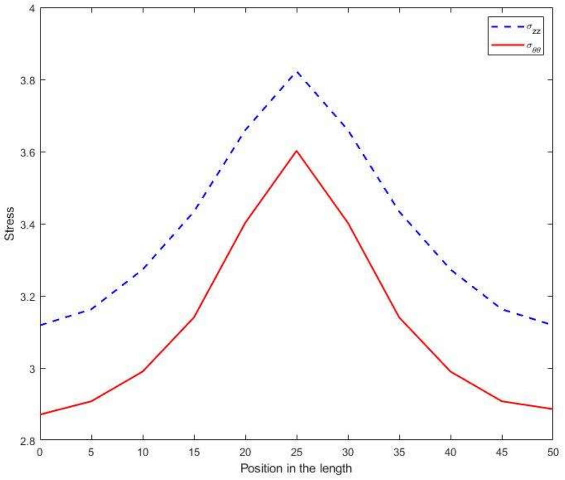

(b) Values of axial and azimuthal average stresses on the cross-sections along the tube length for $\bar{\alpha}_d = -40, \bar{\alpha}_d = 0.5$ and $\lambda_z = 1.4$ just before bulging. Maximum values at the center of the cylinder where the bulge appears.

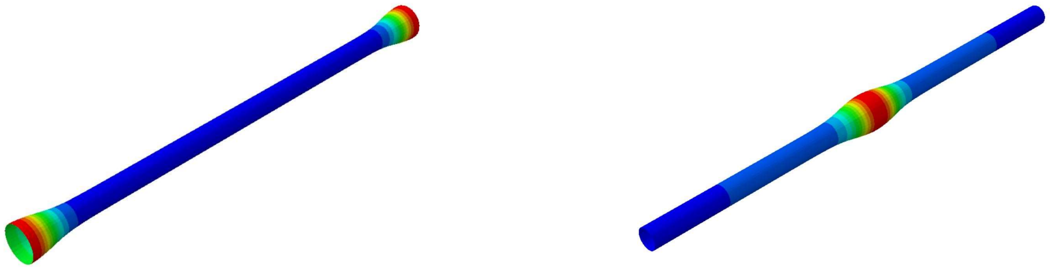

(c) Bulging instability occurring at both ends of the cylinder, associated with figure (a).

(d) Bulging instability appearing at the middle of the cylinder, associated with figure (b).

Figure 5.9: Different bulge locations along the tube for cases with different residual stress constitutive parameters.

Furthermore, current numerical simulations also show that maximum values of stresses for bulging bifurcation are predicted to occur at the middle of the cylinder for CASE-$_{\text{I6}}$ 3, 4 and 6 through 9, for which $\bar{\alpha}_d$ is non positive. This bulging location behaviour along the length of the tube does not depend upon the axial stretch for the domain of values studied in this work, as is shown in what follows.

Attention has been paid to sufficiently large values of λ_z for which the onset of bifurcation is bulging. Now the focus is put in smaller values of λ_z for which the onset of bifurcation is bending. The same models are considered with a different value of axial stretch $\lambda_z = 1.12$. Representative results for CASE-$_{\text{I6}}$ 1 ($\bar{\alpha}_d = 40$) and CASE-$_{\text{I6}}$ 3 ($\bar{\alpha}_d = -40$) can be seen in Figure 5.10 and Figure 5.11, respectively, where average values of azimuthal and axial stresses at the cross-sections along the cylinder length just before bifurcation (bending) are shown.

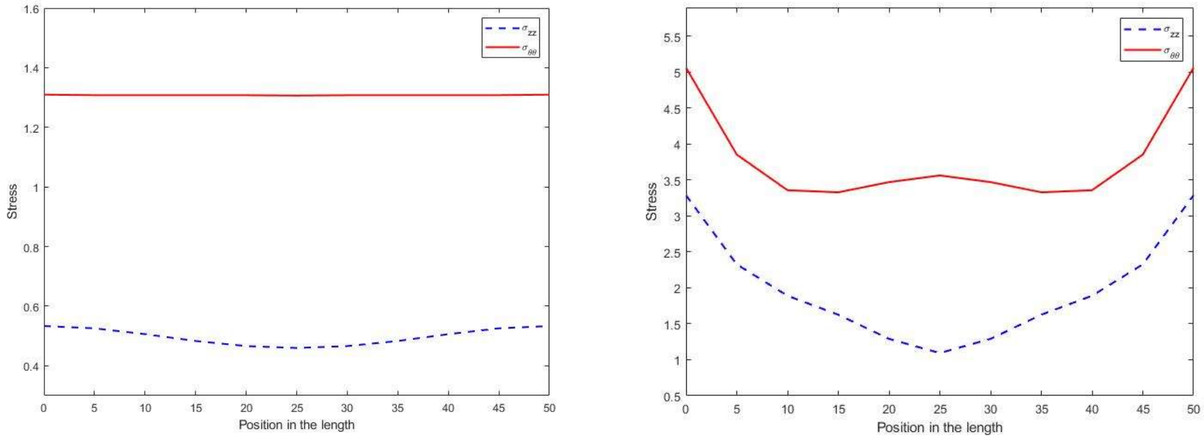

(a) Values of axial and azimuthal average stresses on each cross-section along the tube length for $\bar{\alpha}_d = 40, \bar{\alpha}_c = 0.5$ and $\lambda_z = 1.12$ just before bending bifurcation.

(b) Values of axial and azimuthal average stresses on each cross-section along the tube length for $\bar{\alpha}_d = 40, \bar{\alpha}_c = 0.5$ and $\lambda_z = 1.12$ just before bulging instability after bending bifurcation.

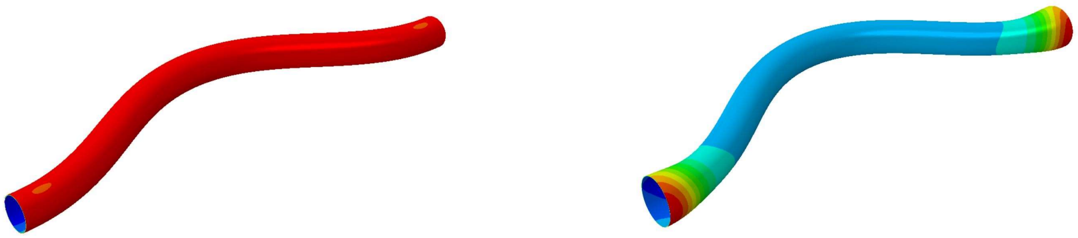

(c) Bending bifurcation mode for model associated with figure (a).

(d) Bulging instability occurring at both ends of the cylinder after bending bifurcation for model associated with figure (b).

Figure 5.10: Bifurcation and post-bifurcation behavior for smaller values of λ_z and positive axial residual stress strength.

In Figure 5.10 (a), the distribution of stresses just prior to bending is shown for the model setting $\bar{\alpha}_d = 40, \bar{\alpha}_c = 0.5$ and $\lambda_z = 1.12$. Both stresses (azimuthal and axial) show approximately constant values along the length of the tube. As it is expected, bending bifurcation occurs with the subsequent capacity of the structure to withstand higher values of pressure [21].

After bending, as pressure increases, one-sided bulges develop (with irregular shape) at both ends of the cylinder. Maximum values of azimuthal and axial stress are expected at those locations prior to bulging. This performance is consistent with the behavior previously discussed when the onset of bifurcation is bulging.

On the other hand, for the model presented in Figure 5.11 (a) with $\bar{\alpha}_d = -40$, $\bar{\alpha}_c = 0.5$ and $\lambda_z = 1.12$ the irregularly-shaped bulge after the bending bifurcation develops at the middle of the cylinder and, accordingly, maximum values of stresses occur at that location. Nevertheless, it will be shown later that these two models (CASE-I6 1 and CASE-I6 3) present similar global behavior from a structural standpoint with respect to the loading conditions associated with bifurcation (except for the occurrence of either a single-bulge or multi-bulge events along the post-bifurcation behavior at different altitudes of the cylinder). This occurs because these two cases have the same value of $\bar{\alpha}_c$, which is the important coefficient to establish the pressure associated with the onset of bulging. The bifurcation and post-bifurcation behaviour for these two models is depicted in Figure 5.10 (c)-(d), and Figure 5.11 (c)-(d). Different deformation patterns along the loading history associated with bending bifurcation mode for CASE-I6 3 for $\lambda_z = 1$ is shown in Figure 5.12.

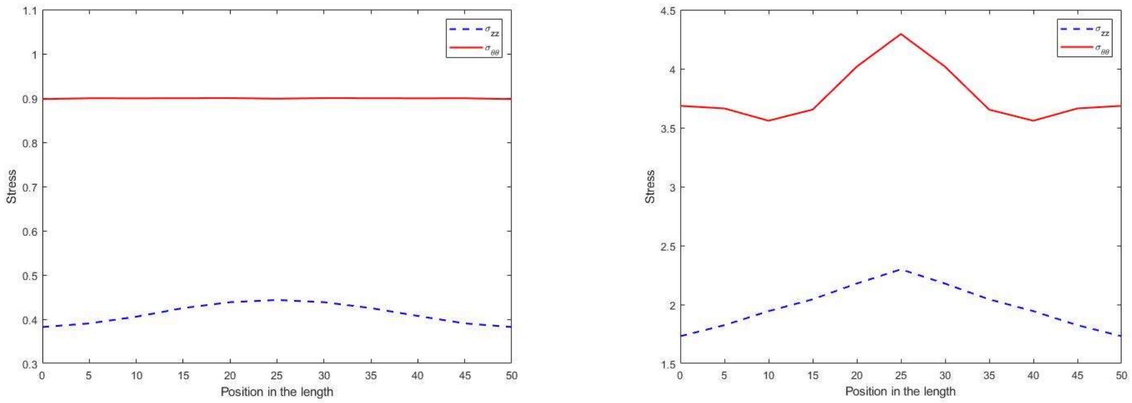

(a) Values of axial and azimuthal average stresses on each cross-section along the tube length for $\bar{\alpha}_d = -40, \bar{\alpha}_c = 0.5$ and $\lambda_z = 1.12$ just before bending bifurcation.

(b) Values of axial and azimuthal average stresses on each cross-section along the tube length for $\bar{\alpha}_d = -40, \bar{\alpha}_c = 0.5$ and $\lambda_z = 1.12$ just before bulging instability after bending bifurcation.

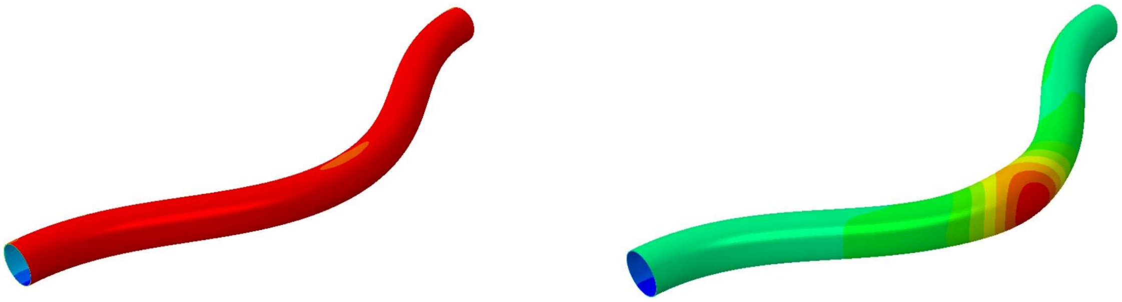

(c) Bending bifurcation mode for model associated with figure (a).

(d) Bulging instability occurring at the middle of the cylinder after bending bifurcation for model associated with figure (b).

Figure 5.11: Bifurcation and post-bifurcation behavior for smaller values of λ_z and negative axial residual stress strength.

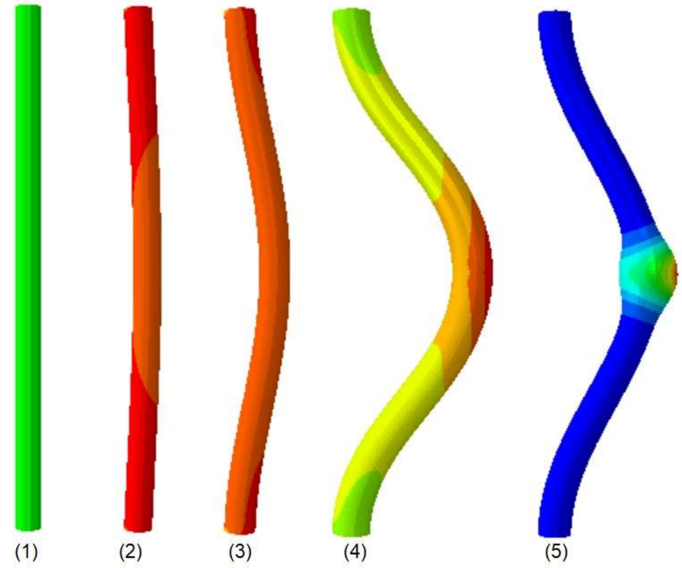

Figure 5.12: History of configurations associated with bending for $\bar{\alpha}_d = -40$, $\bar{\alpha}_c = 0.5$, and $\lambda_z = 1.0$. The order of the numbers in this figure is the same as the ones given in Figure 5.7.

Bulges are found either at the center of the tube or at both ends of the tube and this location depends on the value of $\bar{\alpha}_d$. The stresses distribution as loading is applied for a given residual stress field is subtle but, in passing, it is worthy to mention the following. The residual stress components that depend on Z are the shearing stress component σ_{0R} , the axial stress component σ_{0ZZ} and the azimuthal stress component $\sigma_{0\Theta\Theta}$. Without loss of generality, let's consider $\bar{\alpha}_c = 0.5$. The influence of $\bar{\alpha}_d$ over these stress components is as follows. All values depending on $\bar{\alpha}_d$ are small compared to values depending on $\bar{\alpha}_c$. In addition, for $Z = 0$, $L/2$ and L the component σ_{0RZ}, where the bulges appear, is zero. This completes the attention of the component σ_{0RZ}, which is plotted in Figure 5.1.

On the other hand, the distribution of σ_{0ZZ} along the length of the cylinder shows its maximum, in absolute value, at the middle of the tube while it is zero at both ends. It is worthy to mention that at the middle of the tube for non-positive $\bar{\alpha}_d$ and values of R close to B, σ_{0ZZ} is positive (traction) while for values of R close to A, σ_{0ZZ} is negative (compression). Under these circumstances, the bulge is captured at the center of the tube. This middle bulge location also occurs for $\bar{\alpha}_d = 0$, i.e. when there is no dependence on Z, which was analyzed in ([16], [21]). Conversely, at the middle of the tube, for sufficiently large positive values of $\bar{\alpha}_d$ and values of R close to B, σ_{0ZZ} is negative (compression), while for values of R close to A, σ_{0Z} is positive (traction). Under these circumstances, bulges are captured at both ends of the tube.

The analysis carried out has focused on the deformed configurations associated with bifurcation modes and their relationship with the constitutive coefficients of the residual stress field. Next, an effort to establish the general loading conditions associated with the bifurcation modes for the different cases of Table 5.1 will be done. Firstly, let's put the attention on capturing just bulging bifurcation mode, which means that azimuthal displacements are restricted along the length of the tube during the numerical simulations.

Results for these analyses are summarized in Figure 5.13, which shows the values of (normalized) inflation pressure vs axial stretch at the onset of bulging bifurcation. For a particular value of λ_z, there are quantitative differences among these 8 cases that include residual stresses and the one with no residual stress, CASE-$_{\text{I6}}$ 7 in Table 5.1. In general, the value of the pressure associated with bulging bifurcation decreases by increasing the axial stretch λ_z. It follows that as the values of axial stretch increase the pressure values associated with bifurcation decrease more rapidly in the models affected by the non-planar residual stress (from cases 1 through 6) than the pressure values associated with bulging for models with a planar residual stress field or no residual stress field (cases 7 through 9).

In addition, it is important to mention that the sign of $\bar{\alpha}_d$ does not have a considerable effect on the loading conditions associated with bulging bifurcation. For that reason CASES-$_{\text{I6}}$ 1 and 3 are indistinguishable as well as CASES-$_{\text{I6}}$ 2 and 4, and so are CASES-$_{\text{I6}}$ 5 and 6. However, for models with a positive value of $\bar{\alpha}_c$

(tensile hoop residual stress in the outer wall of the cylinder) bulging bifurcation occurs at lower pressure values than the ones associated for models with a negative value of $\bar{\alpha}_c$ (compressive hoop residual stress in the outer wall of the cylinder).

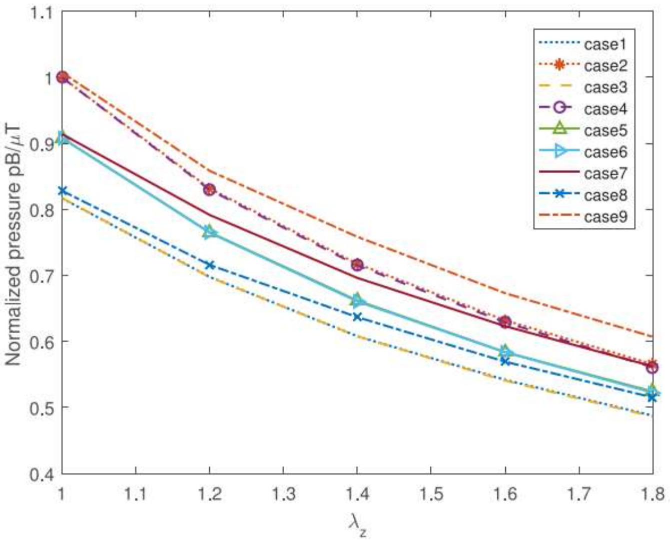

Figure 5.13: Values of normalized inflation pressure against axial stretch at the onset of bulging bifurcation for the nine material models in Table 5.1 considering $f = 0$ (I_6). For cases affected by $\bar{\alpha}_d$ (1 – 6) the values of bifurcation pressure decrease more rapidly as λ_z increases than for the cases where $\bar{\alpha}_d = 0$. The sign of $\bar{\alpha}_d$ does not have a considerable effect on the loading conditions associated with bifurcation.

Corresponding simulations in which a general incremental displacement field given by equation (3-29) (azimuthal displacements are not restricted along the tube length) is considered, and results are shown in Figure 5.14. For clarity and since the sign of $\bar{\alpha}_d$ does not have a considerable effect on the bifurcation pressures the cases with negatives values of this parameter are not shown (they are like the positive ones). For reference, the profile of normalized pressure against the axial stretch obtained for the model with no residual stress (CASE-$_{\text{I6}}$ 7 with $\bar{\alpha}_d = \bar{\alpha}_c = 0$) is shown and it is equal to that presented in Figure 5.13. A simple comparison of Figure 5.13 with Figure 5.14, gives a broader picture of the effect of residual stresses on bifurcation. On the one hand, differing from results shown in Figure 5.13, the onset of bifurcation for sufficiently small values of λ_z (approximately 1.2 > $\lambda_z \geq 1$) does not correspond to bulging phenomena. Numerical calculations show that the onset of bifurcation for this domain of axial stretch corresponds to bending mode ($m = 1$), as it has been coherently exposed in Figure 5.7, Figure 5.10 (d) and Figure 5.11 (d). On the other hand, for values outside of that domain of λ_z, Figure 5.13 and Figure 5.14 are identical.

By increasing λ_z, greater axial stresses σ_{zz} are generated on the cylinder, stimulating the onset of bulging bifurcation instead of bending bifurcation. This behavior of the axial stress component as λ_z increases is also visualized comparing the values of stresses of Figure 5.9 (a), which is obtained for $\lambda_z = 1.4$, with the values of stresses of Figure 5.10 (a) and (b), which are obtained for $\lambda_z = 1.12$, and, similarly, comparing Figure 5.9 (b), with Figure 5.11 (a) and (b). The maximum values of stress along the length of the tube correspond to σ_{zz} for $\lambda_z = 1.4$ while that is not the case for $\lambda_z = 1.12$.

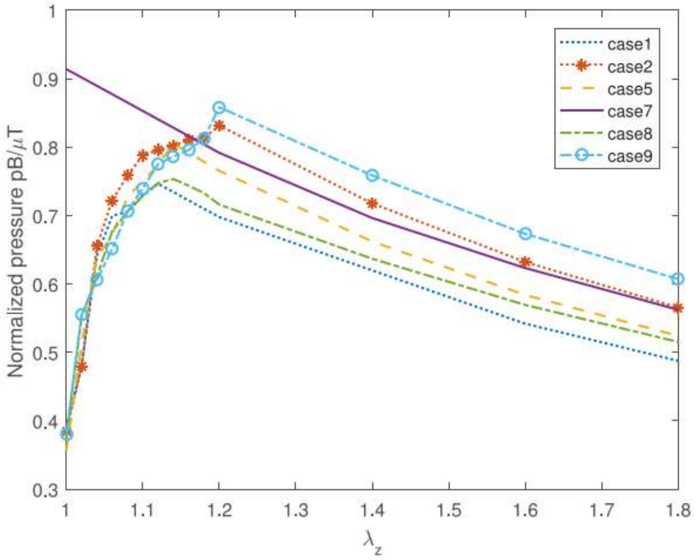

Figure 5.14: Normalized inflation pressure vs axial stretches at bifurcation for the constitutive models presented in Table 5.1 considering I6 invariant. Regarding the three-dimensional residual stress fields, only the cases with positive values of $\bar{\alpha}_d$ are presented as the corresponding negative ones are similar (see Figure 5.13). It is appreciated that for values of, approximately, $\lambda_z \leq 1.2$, the onset of bifurcation is bending with a buckling mode m=1, while for $\lambda_z > 1.2$ the onset of bifurcation is bulging.

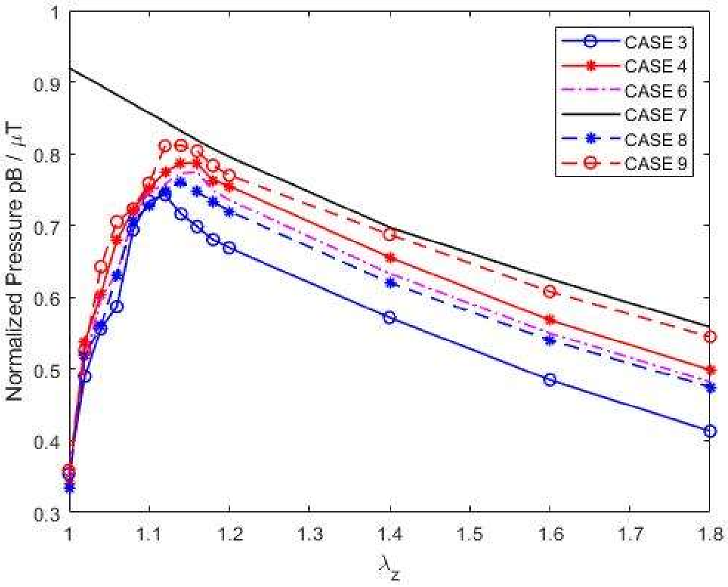

Figure 5.15: Normalized inflation pressure vs axial stretches at bifurcation for the constitutive models presented in Table 5.1 considering I5 invariant. Regarding the three-dimensional residual stress fields, only the cases with non-positive values of $\bar{\alpha}_d$ are presented as the corresponding positive ones are similar (see Figure 5.13). It is appreciated that for values of, approximately, $\lambda_z < 1.2$, the onset of bifurcation is bending with a buckling mode m=1, while for $\lambda_z \geq 1.2$ the onset of bifurcation is bulging.

In Figure 5.15 the normalized inflation pressures at bifurcation against axial stretches applied are presented for the cases of Table 5.1 considering the invariant I_5. In general, the same effects as the previously discussed from Figure 5.14 relating to the values of the residual stress coefficients $\bar{\alpha}_d$ and $\bar{\alpha}_c$ are depicted. However, it should be pointed out that by considering the invariant I_5 the pressure values obtained at bifurcation are lower than the ones extracted when considering the invariant I_6.

So far, the effect of the axial residual stress on the bulge location in the tube, the residual stress field effect on the bifurcation pressures and the effect of the magnitude of the applied axial stretch on the bifurcation mode have been analyzed and described. This gives a wide picture of the behavior of the considered models at bifurcation. It is important to mention that bulging is always catastrophic and propagation of the bulge (or bulges depending on the value of $\bar{\alpha}_d$) is radial and would be related to a rupture of the tube since it grows with a decrease in the capacity of supporting inflation pressure (see [12], [14] and references therein).

When bulging gives the onset of bifurcation the qualitative behavior of history of configurations is given in Figure 5.8 with an axisymmetric bulge. Stemming from the previous comprehensive analysis and in line with an application-devised perspective, it is possible to identify that after the first bending bifurcation mode, which is predicted to occur for small values of λ_z, the structure along the post-bifurcation regime is able to withstand higher values of internal pressure until the occurrence of bulging bifurcation, leading to a decay in the response to the external loading. A continuous stiffness degradation becomes active after this bulging bifurcation.

The decay in the tube response was represented by the region after point B in Figure 5.4, and in the region after the maximum point of the dashed line in Figure 5.6. Also, it is recalled that this post-bifurcation behavior is described, for example, by Figure 5.10 (d) and Figure 5.11 (d), which show that they are non-azimuthally symmetric bulges. The bulges or abnormal enlargements appear towards one side of the cylinder showing an irregular shape, which is consistent with the development of abdominal aortic aneurysms (AAA). Furthermore, bulge propagates radially in its subsequent post-bifurcation behavior, which would be associated with an aneurysm rupture.

In Figure 5.16 for CASE-$_{\mathrm{I6}}$ 1 with $\bar{\alpha}_d = 40$ and $\bar{\alpha}_c = 0.5$ several simulations are carried out, each of them with a specific value of axial stretch in the range $\lambda_z = [1, 1.8]$. For each value of axial stretch, two simulations are run, one model with azimuthal displacements restricted along the tube length and another model without this restriction. From the first set of simulations, normalized inflation pressure values at the onset of bifurcation (which is bulging for all values of λ_z as bending is not allowed) are represented by the solid line (just bulging) in Figure 5.16. From the second set of simulations (models without azimuthal displacements restricted) both, normalized inflation pressure values at bending bifurcation and at bulging occurring after bending, for values of $\lambda_z = [1, 1.18]$ are represented by the dashed line and the dot dashed line, respectively (bending and bent bulge). For this second set of simulations, normalized inflation pressure values at bifurcation for greater values of axial stretch (which is bulging) are also plot.

It should be noted that the pressure values associated with the onset of this irregular bulge on models with sufficiently small values of λ_z are lower than the values of pressure associated with bulging bifurcation on similar models when azimuthal displacements are restricted (when bending bifurcation is not allowed). It follows that a delayed aneurysm formation is propitiated if bending is not allowed to occur. For sufficiently large values of λ_z results shown in Figure 5.16 indicate a transition from bending to bulging bifurcation. The transition zone is different for each case in Table 5.1, with values of λ_z between 1.14 to 1.20, approximately, but it is not ruled out that this zone can be further limited by running simulations with much more refined meshes, which would require more computational time and capabilities.

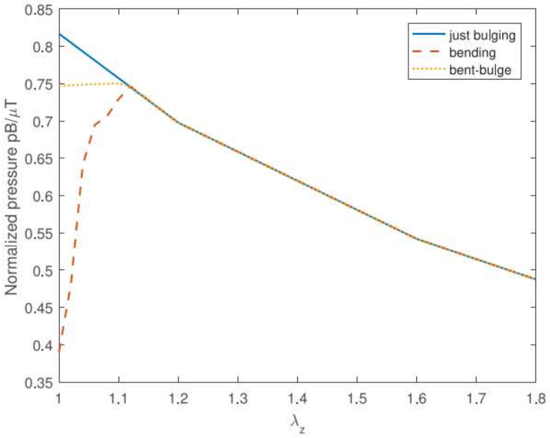

Figure 5.16: Normalized inflation pressure at bifurcation against axial stretch for the case with $\bar{\alpha}_d = 40$ and $\bar{\alpha}_c = 0.5$, from two sets of simulations with $\lambda_z = [1, 1.8]$: (a) one set with azimuthal displacements restricted along the tube length (just bulging) and (b) another set without this restriction (bending and bent-bulge).

To complement the present analysis, Figure 5.17 depicts different deformed configurations for CASE-I6 2 with $\lambda_z = 1.18$, which is close to a transition between bending to bulging bifurcation. In these plots, it is possible to observe that bending bifurcation shows little development with an almost concomitant occurrence of bending and bulging bifurcations (at very similar pressure values). It follows that the deflection of the cylinder due to bending is very small, compared with others with smaller values of axial stretch as shown in Figure 5.12 for $\lambda_z = 1$.

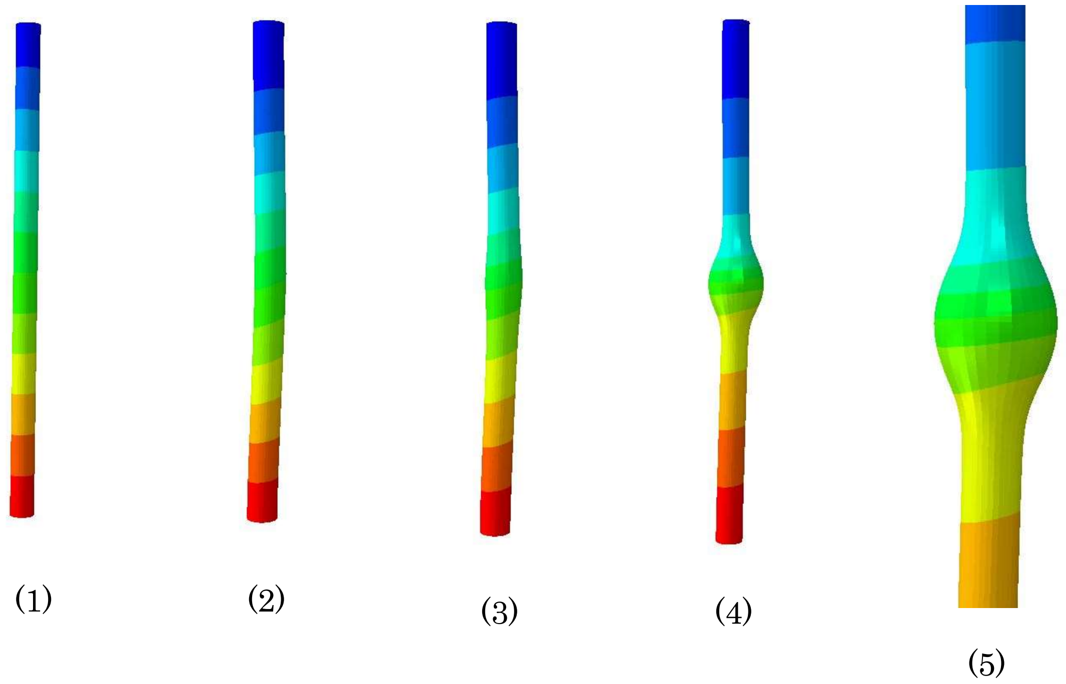

Figure 5.17: History of configurations associated with bending for CASE-I6 2 ($\bar{\alpha}_d = -40$ and $\bar{\alpha}_c = 0.5$) for $\lambda_z = 1.18$. (1) is the beginning of inflation, (2) is the onset of bending bifurcation, (3) is the initiation of bulging after bending, (4) shows further development of the non-azimuthally symmetric bulge and (5) is a widened picture of it.

6. Conclusions

The current investigation develops a nonlinear FE-based methodology for boundary value problems (BVP) that includes residually stressed tubes subjected to combined uniform internal pressure and axial loading. This numerical technique has been implemented into the FE code ABAQUS via the use of the user-defined capabilities UMAT and SDVINI that account for the definition of the material model and the initial stress field using state dependent variables, respectively.

From a material point of view, a Neo-Hookean strain energy function has been used to define the constitutive model, which is affected by either, a two or a three-dimensional residual stress field (in equilibrium) in the absence of external loads. Bending and bulging bifurcations have been captured depending on the axial stretch. In a parallel analysis to the one established for cylindrical membranes, a framework for the numerical results in terms of the azimuthal ($\sigma_{\theta\theta}$) and axial (σ_{zz}) stresses has been established. Since in this work tubes with thickness are considered, average values of stresses at the cross sections are computed. From this condition, it can be concluded that:

- For sufficiently small values of axial stretch, bending bifurcation has been captured. Under this condition the maximum stress inside the tube is clearly not σ_{zz}. One-sided bulges (with an irregular shape) appear during the post-bending analysis. This behaviour is consistent with the development of abdominal aortic aneurysms (AAA). It follows that delayed aneurysm formation is possible if bending is not allowed to occur. These results have been captured for the models with a 2D residual stress field (see [21]), as well as for the models with a 3D residual stress field (see [136]), which shows that the results from both cases are consistent and that the implemented methodology is sufficiently robust.

- Results show that as the axial stretch increases the stress σ_{zz} inside the tube also increases and triggers bulging as the onset of bifurcation. For the models at hand, in all simulations the bulge in subsequent motion (after bulging bifurcation) propagates radially, which would be related to an aneurysm rupture (see [21] and [136]).

Concerning the analysis of the effect of the 3D residual stress field on bifurcation and post-bifurcation behavior, a comparison has been made with the corresponding results from the case in which there is no residual stress. The numerical calculations have shown that the magnitude of the axial component of the residual stress, which is ruled by the non-dimensional parameter $\bar{\alpha}_d$ affects the location of the bulge along the length of the tube [136]. On the one hand, positive values of $\bar{\alpha}_d$, led to the prediction of bulging effects which take place at the ends of the tube regardless of the value of the axial stretch. Conversely, negative values of $\bar{\alpha}_d$ are associated with the development of a bulge at the middle of the tube, in line with cases with planar residual stresses [21] or no residual stress since in these cases there is no dependence on the axial length of the tube. It follows that considering a 3D residual stress field (with a non-zero axial component) the position of the bulge along the length of the tube is captured [136].

Furthermore, by analyzing various models it has been shown that the inflation pressure associated with bifurcation is qualitatively affected by both the axial stretch and the residual stress field ([21], [136]). As the axial stretch increases, the inflation pressure associated with bifurcation decreases more rapidly for cases with a non-planar residual stress field in the strain energy function of the material than for cases without this residual stress field.

From a Finite Element approach bulging and bending instabilities have been captured for thick-walled circular cylindrical tubes including the effects of planar and three-dimensional residual stress fields, incorporated in the strain energy potential characterizing the response of the hyperelastic material. Hybrid formulation with three-dimensional continuum solid elements have been used for correctly accounting for the material incompressibility. The corresponding post-bifurcation behavior of the tubes has also been captured and analyzed in the context of AAA. This post-bifurcation behavior has been followed exploiting the capacity of the Modified-Riks method already integrated in Abaqus. The following aspects have been conducted ([21], [136]):

- Systematic study of the axial stretch of the tubes on inflation tests within the continuum theory of (axially) residually stressed models.

- Development of a finite strain residually stressed constitutive model that considers axial stress components able to capture bifurcation modes such as bulging and bending and its potential application to aneurysms formation.

- Contribution to fill the literature gap between scientific analysis and professional practice using commercial finite element codes, which provides progress to both engineering analysis and design and scientific world.

The development and use of numerical procedures to solve bifurcation and post-bifurcation problems is by itself a framework that needs to be studied to open new possibilities and perspectives in both scientific and professional practice since it is an important source of expansion and progress to engineering analysis and design.

References

[1] D. L. Logan, *A First Course in the Finite Element Method*, 4th ed., Ontario, CA: Nelson, 2007

[2] T. J. R. Hughes, *The Finite Element Method. Linear static and dynamic finite element analysis*, New Jersey: Prentice-Hall Inc., 1987

[3] D. M. Haughton and R. W. Ogden, "Bifurcation Of Inflated Circular Cylinders Of Elastic Material Under Axial Loading-I. Membrane Theory For Thin-Walled Tubes," *Journal of the Mechanics and Physics of Solids,* vol. 27, *(3),* pp. 179–212, 1979. DOI: 10.1016/0022-5096(79)90001-2

[4] J. Merodio and D. M. Haughton, "Bifurcation of thick-walled cylindrical shells and the mechanical response of arterial tissue affected by Marfan's syndrome," *Mech. Res. Commun.,* vol. 37, *(1),* pp. 1–6, 2010. Available: https://www.sciencedirect.com/science/article/pii/S0093641309001530. DOI: 10.1016/j.mechrescom.2009.10.006

[5] R. W. Ogden, *Non-Linear Elastic Deformations,* 1st ed., New York: Dover Publications, 1997

[6] R. W. Ogden, *Nonlinear Elasticity with Application to Material Modelling,* Warsaw: Institute of Fundamental and Technological Research, 2003

[7] N. T. Nam, J. Merodio, R. W. Ogden and P. C. Vinh, "The effect of initial stress on the propagation of surface waves in a layered half-space," *International Journal of Solids and Structures,* vol. 88-89, pp. 88-100, 2016. DOI: 10.1016/j.ijsolstr.2016.03.019

[8] G. Chagnon, M. Rebouah and D. Favier, "Hyperelastic Energy Densities for Soft Biological Tissues: A Review," *J Elast,* vol. 120, *(2),* pp. 129-160, 2015. DOI: 10.1007/s10659-014-9508-z

[9] H. Demirkoparan and J. Merodio, "Bulging bifurcation of inflated circular cylinders of doubly fiber-reinforced hyperelastic material under axial loading and swelling," *Mathematics and Mechanics of Solids,* vol. 22, *(4),* pp. 666–682, 2017. Available: https://doi.org/10.1177/1081286515600045. DOI: 10.1177/1081286515600045

[10] T. Ahamed, L. Dorfmann and R. W. Ogden, "Modelling of residually stressed materials with application to AAA," *Journal of the Mechanical Behavior of Biomedical Materials,* vol. 61, pp. 221, 2016. DOI: 10.1016/j.jmbbm.2016.01.012

[11] G. A. Holzapfel and R. W. Ogden, "Modelling the layer-specific three-dimensional residual stresses in arteries, with an application to the human aorta," *Journal of the Royal Society*, vol. 7, *(46)*, 2009. DOI: https://doi.org/10.1098/rsif.2009.0357

[12] H. Demirkoparan and J. Merodio, "Swelling and axial propagation of bulging with application to aneurysm propagation in arteries," *Mathematics and Mechanics of Solids,* vol. 25, *(7),* pp. 1459–1471, 2020. Available: https://journals.sagepub.com/doi/full/10.1177/1081286517717127. DOI: 10.1177/1081286517717127

[13] A. A. Alhayani, J. A. Giraldo, J. Rodríguez and J. Merodio, "Computational modelling of bulging of inflated cylindrical shells applicable to aneurysm formation and propagation in arterial wall tissue," *Finite Elements in Analysis and Design,* vol. 73, pp. 20, 2013. DOI: 10.1016/j.finel.2013.05.001

[14] A. A. Alhayani, J. Rodríguez and J. Merodio, "Competition between radial expansion and axial propagation in bulging of inflated cylinders with application to aneurysms propagation in arterial wall tissue," *International Journal of Engineering Science,* vol. 85, pp. 74–89, 2014. Available:

https://dx.doi.org/10.1016/j.ijengsci.2014.08.008. DOI: 10.1016/j.ijengsci.2014.08.008

[15] N. K. Jha, J. Reinoso, H. Dehghani and J. Merodio, "Constitutive modeling framework for residually stressed viscoelastic solids at finite strains," *Mechanics Research Communications,* vol. 95, pp. 79, 2019. DOI: 10.1016/j.mechrescom.2019.01.003

[16] A. Font, N. K. Jha, H. Dehghani, J. Reinoso and J. Merodio, "Modelling of residually stressed, extended and inflated cylinders with application to aneurysms," *Mechanics Research Communications,* vol. 111, 2020. DOI: 10.1016/j.mechrescom.2020.103643

[17] J. Rodríguez and J. Merodio, "A new derivation of the bifurcation conditions of inflated cylindrical membranes of elastic material under axial loading. Application to aneurysm formation," *Mechanics Research Communications,* vol. 38, *(3),* pp. 203, 2011. DOI: 10.1016/j.mechrescom.2011.02.004

[18] Y. B. Fu, G. A. Rogerson and Y. T. Zhang, "Initiation of aneurysms as a mechanical bifurcation phenomenon," *International Journal of Non-Linear Mechanics,* vol. 47, *(2),* pp. 179, 2011. DOI: 10.1016/j.ijnonlinmec.2011.05.001

[19] Y. B. Fu, J. L. Liu and G. S. Francisco, "Localized bulging in an inflated cylindrical tube of arbitrary thickness – the effect of bending stiffness," *Journal of the Mechanics and Physics of Solids,* vol. 90, pp. 45, 2016. DOI: 10.1016/j.jmps.2016.02.027

[20] P. N. Watton, N. A. Hill and M. Heil, "A mathematical model for the growth of the abdominal aortic aneurysm," *Biomech Model Mechanobiol,* vol. 3, *(2),* pp. 98, 2004. DOI: 10.1007/s10237-004-0052-9

[21] H. Dehghani, D. Desena-Galarza, N. K. Jha, J. Reinoso and J. Merodio, "Bifurcation and post-bifurcation of an inflated and extended residually-stressed circular cylindrical tube with application to aneurysms initiation and propagation

in arterial wall tissue," *Finite Elements in Analysis and Design,* vol. 161, pp. 51-60, 2019. DOI: 10.1016/j.finel.2019.04.004

[22] Y. C. Fung, *Biomechanics: Mechanical Properties of Living Tissues*, 2. ed., New York: Springer-Verlag, 1993

[23] H. Dehghani, R. Penta and J. Merodio, "The role of porosity and solid matrix compressibility on the mechanical behavior of poroelastic tissues," *Mater. Res. Express,* vol. 6, *(3),* 2018. DOI: 10.1088/2053-1591/aaf5b9

[24] J. Marchena-Menéndez, A. Ramírez-Torres, R. Penta, R. Rodríguez-Ramos and J. Merodio, "Macroscopic thermal profile of heterogeneous cancerous breasts. A three-dimensional multiscale analysis," *Int. J. Eng. Sci.,* vol. 144, pp. 103135, 2019. DOI: 10.1016/j.ijengsci.2019.103135

[25] R. Penta and D. Ambrosi, "The role of the microvascular tortuosity in tumor transport phenomena," *J. Theor. Biol.,* vol. 364, pp. 80–97, 2015. DOI: 10.1016/j.jtbi.2014.08.007

[26] H. Topol and T. J. Pence, "Homeostatic collagen remodeling: enzymatic strain stabilization and large strain softening in pressurized thick-walled cylindrical vessels," *Mech Soft Mater,* vol. 6, *(1),* 2024. DOI: 10.1007/s42558-024-00062-3

[27] H. Topol, H. Nazari, M. Stoffel, B. Markert, J. Lacalle and J. Merodio, "Instabilities of an inflated and extended doubly fiber-reinforced cylindrical membrane under damage processes and different natural configurations of its constituents with application to abnormal artery dilation," *Thin-Walled Structures,* vol. 197, pp. 111562, 2024. DOI: 10.1016/j.tws.2024.111562

[28] S. García, J. García and D. González, *Cardiología y Cirugía Cardiovascular. Manual de Medicina y Cirugía.* 11th ed., Madrid: Grupo CTO, 2019. Available: https://www.grupocto.shop/

[29] “Abdominal Aortic Aneurysm”, Cleveland Clinic. https://my.clevelandclinic.org/ (accessed Aug. 15th, 2024)

[30] G. A. Holzapfel, T. C. Gasser and R. W. Ogden, "A new constitutive framework for arterial wall mechanics and a comparative study of material models," *Journal of Elasticity,* vol. 61*,* pp. 1–48, 2000. DOI: https://doi.org/10.1023/A:1010835316564

[31] “Abdominal aortic aneurysm”, NHS. https://www.nhs.uk/ (accessed Aug. 15th, 2024)

[32] J. D. Humphrey, "Vascular Adaptation and Mechanical Homeostasis at Tissue, Cellular, and Sub-cellular Levels," *Cell Biochem Biophys,* vol. 50, *(2),* pp. 53, 2007. DOI: 10.1007/s12013-007-9002-3

[33] C. J. Cyron, R. C. Aydin and J. D. Humphrey, "A homogenized constrained mixture (and mechanical analog) model for growth and remodeling of soft tissue," *Biomech Model Mechanobiol,* vol. 15, *(6),* pp. 1389, 2016. DOI: 10.1007/s10237-016-0770-9

[34] A. Ghavamian, S. J. Mousavi and S. Avril, "Computational Study of Growth and Remodeling in Ascending Thoracic Aortic Aneurysms Considering Variations of Smooth Muscle Cell Basal Tone," *Front. Bioeng. Biotechnol.,* vol. 8, 2020. DOI: 10.3389/fbioe.2020.587376

[35] A. Grytsan, T. S. E. Eriksson, P. N. Watton and T. C. Gasser, "Growth Description for Vessel Wall Adaptation: A Thick-Walled Mixture Model of Abdominal Aortic Aneurysm Evolution," *Materials,* vol. 10, *(9),* pp. 994, 2017. DOI: 10.3390/ma10090994

[36] S. J. Mousavi, S. Farzaneh and S. Avril, "Patient-specific predictions of aneurysm growth and remodeling in the ascending thoracic aorta using the homogenized constrained mixture model," *Biomech Model Mechanobiol,* vol. 18, *(6),* pp. 1895-1913, 2019. DOI: 10.1007/s10237-019-01184-8

[37] Y. B. Fu, S. P. Pearce and K. K. Liu, "Post-bifurcation analysis of a thin-walled hyperelastic tube under inflation," *International Journal of Non-Linear Mechanics,* vol. 43, *(8),* pp. 697, 2008. DOI: 10.1016/j.ijnonlinmec.2008.03.003

[38] N. K. Jha, J. Reinoso, H. Dehghani and J. Merodio, "A computational model for fiber-reinforced composites: hyperelastic constitutive formulation including residual stresses and damage," *Comput Mech,* vol. 63, *(5),* pp. 931-948, 2019. DOI: 10.1007/s00466-018-1630-5

[39] Y. Du, M. Destrade and W. Chen, "Influence of Initial Residual Stress on Growth and Pattern Creation for a Layered Aorta," *Sci Rep,* vol. 9, *(1),* 2019. DOI: 10.1038/s41598-019-44694-2

[40] J. Merodio and R. W. Ogden, "Extension, inflation and torsion of a residually stressed circular cylindrical tube," *Continuum Mech. Thermodyn.,* vol. 28, *(1-2),* pp. 157, 2015. DOI: 10.1007/s00161-015-0411-z

[41] J. Rodríguez and J. Merodio, "Helical buckling and postbuckling of pre-stressed cylindrical tubes under finite torsion," *Finite Elements in Analysis and Design,* vol. 112, pp. 1, 2015. DOI: 10.1016/j.finel.2015.12.003

[42] N. K. Jha, J. Merodio and J. Reinoso, "A general non-local constitutive relation for residually stressed solids," *Mechanics Research Communications,* vol. 101, 2019. DOI: 10.1016/j.mechrescom.2019.103421

[43] A. Hoger, "On the Residual Stress Possible in an Elastic Body with Material Symmetry," *Archive for Rational Mechanics and Analysis,* vol. 88, *(3),* pp. 271–289, 1985. Available: https://doi.org/10.1007/BF00752113. DOI: 10.1007/BF00752113

[44] SIMULIA Abaqus 6.14, "Abaqus Documentation," 2014

[45] J. Merodio, R. W. Ogden and J. Rodríguez, "The influence of residual stress on finite deformation elastic response," *International Journal of Non-Linear Mechanics,* vol. 56, pp. 43, 2013. DOI: 10.1016/j.ijnonlinmec.2013.02.010

[46] M. Shams, M. Destrade and R. W. Ogden, "Initial stresses in elastic solids: Constitutive laws and acoustoelasticity," *Wave Motion,* vol. 48, *(7),* pp. 552–567, 2011. Available: https://dx.doi.org/10.1016/j.wavemoti.2011.04.004. DOI: 10.1016/j.wavemoti.2011.04.004

[47] R. W. Ogden and G. A. Holzapfel, *Biomechanics of Soft Tissue in Cardiovascular Systems*, 1st ed., Wien: Springer Vienna, 2003

[48] R. N. Vaishnav and J. Vossoughi, "Estimation of residual strains in aortic segments," in *Biomedical Engineering II*, C. W. Hall, Ed. 1983, Available: https://www.sciencedirect.com/science/article/pii/B9780080301457500787. DOI: 10.1016/B978-0-08-030145-7.50078-7

[49] M. Destrade, I. Lusetti, R. Mangan and T. Sigaeva, "Wrinkles in the opening angle method," *Int. J. Solids Structures,* vol. 122-123, pp. 189–195, 2017. Available: https://www.sciencedirect.com/science/article/pii/S0020768317302822. DOI: 10.1016/j.ijsolstr.2017.06.016

[50] A. Hoger, "The constitutive equation for finite deformations of a transversely isotropic hyperelastic material with residual stress," *Journal of Elasticity,* vol. 33, *(2),* pp. 107–118, 1993. DOI: 10.1007/BF00705801

[51] A. Hoger, "The elasticity tensor of a transversely isotropic hyperelastic material with residual stress," *Journal of Elasticity,* vol. 42, *(2),* pp. 115–132, 1996. DOI: 10.1007/BF00040956

[52] B. E. Johnson and A. Hoger, "The use of a virtual configuration in formulating constitutive equations for residually stressed elastic materials," *Journal of Elasticity,* vol. 41, *(3),* pp. 177–215, 1995. . DOI: 10.1007/BF00041874

[53] D. Balzani, J. Schröder and D. Gross, "Numerical simulation of residual stresses in arterial walls," *Computational Materials Science,* vol. 39, *(1),* pp. 117, 2007. . DOI: 10.1016/j.commatsci.2005.11.014

[54] J. Merodio and R. W. Ogden, "Finite deformation elasticity theory," in *Constitutive Modelling of Solid Continua*, Switzerland: Springer Cham, 2020, ch. 2, pp. 17–52

[55] A. Valverde-González, J. Reinoso, N. K. Jha, J. Merodio and M. Paggi, " A phase field approach to fracture for hyperelastic and visco-hyperelastic materials

applied to pre-stressed cylindrical structures," *Mechanics of Advanced Materials and Structures,* vol. 31, *(4),* pp. 749–768, 2024. Available: https://www.tandfonline.com/doi/abs/10.1080/15376494.2022.2121452. DOI: 10.1080/15376494.2022.2121452

[56] M. Shahzad, A. Kamran, M. Z. Siddiqui and M. Farhan, "Mechanical Characterization and FE Modelling of a Hyperelastic Material," *Materials Research,* vol. 18, 2015. . DOI: 10.1590/1516-1439.320414

[57] R. Bustamante and J. Merodio, "On simple constitutive restrictions for transversely isotropic nonlinearly elastic materials and isotropic magneto-sensitive elastomers," *J Eng Math,* vol. 68, *(1),* pp. 15, 2009. . DOI: 10.1007/s10665-009-9358-z

[58] J. Merodio and R. W. Ogden, "The influence of the invariant I_8 on the stress–deformation and ellipticity characteristics of doubly fiber-reinforced non-linearly elastic solids," *International Journal of Non-Linear Mechanics,* vol. 41, *(4),* pp. 556, 2006, doi: 10.1016/j.ijnonlinmec.2006.02.001

[59] J. Merodio and R. W. Ogden, "On tensile instabilities and ellipticity loss in fiber-reinforced incompressible non-linearly elastic solids," 2005. Available: http://eprints.gla.ac.uk/13162

[60] J. Merodio and R. W. Ogden, "Material instabilities in fiber-reinforced nonlinearly elastic solids under plane deformation," *Archives of Mechanics,* vol. 54, *(5-6),* pp. 525–552, 2002. Available: https://am.ippt.pan.pl/am/article/view/v54p525

[61] S. E. Bechtel and R. L. Lowe, *Fundamentals of Continuum Mechanics With Applications to Mechanical, Thermomechanical, and Smart Materials,* Academic Press, 2015, Available: https://ebookcentral.proquest.com/lib/[SITE_ID]/detail.action?docID=5754518, DOI: 10.1016/C2011-0-06151-3

[62] A. Wineman, "Some results for generalized neo-Hookean elastic materials," *Int. J. Non-Linear Mech.,* vol. 40, *(2),* pp. 271–279, 2005. Available: https://www.sciencedirect.com/science/article/pii/S0020746204000587. DOI: 10.1016/j.ijnonlinmec.2004.05.007

[63] D. Emery and Y. Fu, "Localised bifurcation in soft cylindrical tubes under axial stretching and surface tension," *International Journal of Solids and Structures,* vol. 219-220, pp. 23, 2021. DOI: 10.1016/j.ijsolstr.2021.02.007

[64] M. J. Al-Chlaihawi, H. Topol, H. Demirkoparan and J. Merodio, "On prismatic and bending bifurcations of fiber-reinforced elastic membranes under swelling with application to aortic aneurysms," *Mathematics and Mechanics of Solids,* vol. 28, *(1),* pp. 108, 2021. DOI: 10.1177/10812865211058767

[65] A. Melnikov, R. W. Ogden, L. Dorfmann and J. Merodio, "Bifurcation analysis of elastic residually-stressed circular cylindrical tubes," *International Journal of Solids and Structures,* vol. 226-227, 2021. DOI: 10.1016/j.ijsolstr.2021.111062

[66] M. A. Biot, *Mechanics of Incremental Deformations,* 1965, Available: https://hal.science/hal-01352219

[67] A. Melnikov and R. W. Ogden, “Bifurcation of finitely deformed thick-walled electroelastic cylindrical tubes subject to a radial electric field,” *Z. Angew. Math. Phys.*, vol. 69, no. 3, May 2018, DOI: https://doi.org/10.1007/s00033-018-0954-5

[68] A. Melnikov, J. Merodio, R. Bustamante and L. Dorfmann, "Bifurcation analysis of residually stressed neo-Hookean and Ogden electroelastic tubes," *Phil. Trans. R. Soc. A,* vol. 380, no. 2234, August 2022. Available: https://royalsocietypublishing.org/doi/full/10.1098/rsta.2021.0331. DOI: 10.1098/rsta.2021.0331

[69] N. K. Jha, S. Moradalizadeh, J. Reinoso, H. Topol and J. Merodio, "On the helical buckling of anisotropic tubes with application to arteries," *Mechanics Research Communications,* vol. 128, pp. 104067, 2023. Available:

https://dx.doi.org/10.1016/j.mechrescom.2023.104067. DOI: 10.1016/j.mechrescom.2023.104067

[70] H. Topol, N. K. Jha, H. Demirkoparan, M. Stoffel and J. Merodio, "Bulging of inflated membranes made of fiber reinforced materials with different natural configurations," *European Journal of Mechanics, A, Solids,* vol. 96, pp. 104670, 2022. Available: https://dx.doi.org/10.1016/j.euromechsol.2022.104670. DOI: 10.1016/j.euromechsol.2022.104670

[71] H. Topol, M. J. Al-Chlaihawi, H. Demirkoparan and J. Merodio, "Bifurcation of Fiber-Reinforced Cylindrical Membranes under Extension, Inflation, and Swelling," *Journal of Applied and Computational Mechanics,* vol. 9, *(1),* pp. 113–128, 2023. Available: https://doaj.org/article/01e2dc820cfa4e9bbfc7c60a6612f490. DOI: 10.22055/jacm.2022.40949.3677

[72] H. Topol, H. Asghari, M. Stoffel, B. Markert and J. Merodio, "Post-bifurcation of inflated fibrous cylindrical membranes under different fiber configurations," *European Journal of Mechanics, A, Solids,* vol. 101, pp. 105065, 2023. Available: https://dx.doi.org/10.1016/j.euromechsol.2023.105065. DOI: 10.1016/j.euromechsol.2023.105065

[73] D. M. Haughton and J. Merodio, "The elasticity of arterial tissue affected by Marfan's syndrome," *Mechanics Research Communications,* vol. 36, *(6),* pp. 659–668, 2009. Available: https://dx.doi.org/10.1016/j.mechrescom.2009.04.002. DOI: 10.1016/j.mechrescom.2009.04.002

[74] S. S. Hayreh, G. E. Servais and P. S. Virdi, "Retinal Arteriolar Changes in Malignant Arterial Hypertension," *Ophthalmologica (Basel),* vol. 198, *(4),* pp. 178–196, Jan 1, 1989

[75] Z. S. Jackson, D. Dajnowiec, A. I. Gotlieb and B. L. Langille, "Partial Off-Loading of Longitudinal Tension Induces Arterial Tortuosity," *Atvb,* vol. 25, *(5),* pp. 957, 2024. DOI: 10.1161/01.atv.0000161277.46464.11

[76] N. C. B. B. Taarnhøj *et al*, "Straight versus tortuous retinal arteries in relation to blood pressure and genetics," *British Journal of Ophthalmology,* vol. 92, *(8),* pp. 1055–1060, 2008. Available: http://dx.doi.org/10.1136/bjo.2007.134593. DOI: 10.1136/bjo.2007.134593

[77] G. A. Cabral-Pacheco *et al*, "The Roles of Matrix Metalloproteinases and Their Inhibitors in Human Diseases," *Int. J. Mol. Sci.,* vol. 21, *(24),* 2020. DOI: 10.3390/ijms21249739

[78] A. Fortier, V. Gullapalli and R. A. Mirshams, "Review of biomechanical studies of arteries and their effect on stent performance," *IJC Heart & Vessels,* vol. 4, pp. 12, 2014. DOI: 10.1016/j.ijchv.2014.04.007

[79] A. H. Corneliussen and R. T. Shield, "Finite deformation of elastic membranes with application to the stability of an inflated and extended tube," *Archive for Rational Mechanics and Analysis,* vol. 7, *(1),* pp. 273–304, 1961. Available: https://doi.org/10.1007/BF00250766. DOI: 10.1007/BF00250766

[80] G. A. Holzapfel, G. Sommer, M. Auer, P. Regitnig and R. W. Ogden, "Layer-Specific 3D Residual Deformations of Human Aortas with Non-Atherosclerotic Intimal Thickening," *Ann. Biomed. Eng.,* vol. 35, *(4),* pp. 530, 2007, DOI: 10.1007/s10439-006-9252-z

[81] I. C. Noyan and J. B. Cohen, Residual Stress: Measurement by Diffraction and Interpretation, 1st ed., New York: Springer, 2013. DOI: https://doi.org/10.1007/978-1-4613-9570-6

[82] L. Dorfmann and R. W. Ogden, "The effect of residual stress on the stability of a circular cylindrical tube," *J Eng Math,* vol. 127, *(1),* 2021. Available: https://link.springer.com/article/10.1007/s10665-021-10097-4. DOI: 10.1007/s10665-021-10097-4

[83] H. Asghari, H. Topol, B. Markert and J. Merodio, "Application of sensitivity analysis in extension, inflation, and torsion of residually stressed circular

cylindrical tubes," *Probabilistic Engineering Mechanics,* vol. 73, pp. 103469, 2023. Available: https://dx.doi.org/10.1016/j.probengmech.2023.103469. DOI: 10.1016/j.probengmech.2023.103469

[84] M. H. B. M. Shariff, R. Bustamante and J. Merodio, "Nonlinear electro-elastic bodies with residual stresses: spectral formulation," *Quarterly Journal of Mechanics and Applied Mathematics,* vol. 71, *(4),* pp. 485–504, 2018. DOI: 10.1093/qjmam/hby015

[85] M. H. B. M. Shariff, R. Bustamante and J. Merodio, "A nonlinear constitutive model for a two preferred direction electro-elastic body with residual stresses," *International Journal of Non-Linear Mechanics,* vol. 119, pp. 103352, 2020. Available: https://dx.doi.org/10.1016/j.ijnonlinmec.2019.103352. DOI: 10.1016/j.ijnonlinmec.2019.103352

[86] M. H. B. M. Shariff, R. Bustamante and J. Merodio, "A nonlinear electro-elastic model with residual stresses and a preferred direction," *Mathematics and Mechanics of Solids,* vol. 25, *(3),* pp. 838–865, 2020. Available: https://journals.sagepub.com/doi/full/10.1177/1081286519891769. DOI: 10.1177/1081286519891769

[87] M. H. B. M. Shariff and J. Merodio, "Residually Stressed Fiber Reinforced Solids: A Spectral Approach," *Materials,* vol. 13, *(18),* pp. 4076, 2020. DOI: https://doi.org/10.3390/ma13184076

[88] SIMULIA Abaqus 6.14, "Abaqus User Subroutines Reference Guide," 2014

[89] N. Vasios, "Nonlinear Analysis of Structures. The Arc Length Method: Formulation, Implementation and Applications," Harvard Scholar Library, 2015, accessed on: May 15th, 2024. [Online]. Available: https://scholar.harvard.edu/files/vasios/files/ArcLength.pdf

[90] P. W. Alford, A. W. Feinberg, S. P. Sheehy and K. K. Parker, "Biohybrid thin films for measuring contractility in engineered cardiovascular muscle,"

Biomaterials, vol. 31, *(13),* pp. 3613, 2010. . DOI: 10.1016/j.biomaterials.2010.01.079

[91] A. A. Alhayani, J. Rodríguez and J. Merodio, "Numerical analysis of neck and bulge propagation in anisotropic tubes subject to axial loading and internal pressure," *Finite Elements in Analysis and Design,* vol. 90, pp. 11–19, 2014. Available: https://dx.doi.org/10.1016/j.finel.2014.06.003. DOI: 10.1016/j.finel.2014.06.003

[92] J. Merodio and R. W. Ogden, "Basic equations of continuum mechanics," in *Constitutive Modelling of Solid Continua*, Switzerland: Springer Cham, 2020, Ch. 1, pp. 1–16

[93] J. Merodio and R. W. Ogden, "Mechanical response of fiber-reinforced incompressible non-linearly elastic solids," *International Journal of Non-Linear Mechanics*, vol. 40, *(2),* pp. 213–227, 2005. Available: https://dx.doi.org/10.1016/j.ijnonlinmec.2004.05.003. DOI: 10.1016/j.ijnonlinmec.2004.05.003

[94] J. Merodio and R. W. Ogden, "Instabilities and loss of ellipticity in fiber-reinforced compressible non-linearly elastic solids under plane deformation," *International Journal of Solids and Structures,* vol. 40, *(18),* pp. 4707–4727, 2003. Available: https://dx.doi.org/10.1016/S0020-7683(03)00309-3. DOI: 10.1016/S0020-7683(03)00309-3

[95] J. Merodio and R. W. Ogden, "A Note on Strong Ellipticity for Transversely Isotropic Linearly Elastic Solids," *Quarterly Journal of Mechanics and Applied Mathematics,* vol. 56, *(4),* pp. 589–591, 2003. Available: https://api.istex.fr/ark:/67375/HXZ-NK4KSPRG-3/fulltext.pdf. DOI: 10.1093/qjmam/56.4.589

[96] J. Merodio and T. J. Pence, "Kink surfaces in a directionally reinforced neo-hookean material under plane deformation: II. Kink band stability and maximally dissipative band broadening," *Journal of Elasticity,* vol. 62, *(2),* pp. 145–170, 2001. DOI: 10.1023/A:1011693326593

[97] J. Merodio and T. J. Pence, "Kink surfaces in a directionally reinforced neo-Hookean material under plane deformation: I. Mechanical equilibrium," *Journal of Elasticity,* vol. 62, *(2),* pp. 119–144, 2001. DOI: 10.1023/A:1011625509754

[98] J. Merodio and J. M. Goicolea, "On thermodynamically consistent constitutive equations for fiber-reinforced nonlinearly viscoelastic solids with application to biomechanics," *Mechanics Research Communications,* vol. 34, *(7),* pp. 561–571, 2007. Available: https://dx.doi.org/10.1016/j.mechrescom.2007.08.006. DOI: 10.1016/j.mechrescom.2007.08.006

[99] J. Merodio, G. Saccomandi and I. Sgura, "The rectilinear shear of fiber-reinforced incompressible non-linearly elastic solids," *International Journal of Non-Linear Mechanics,* vol. 42, *(2),* pp. 342–354, 2007. Available: https://dx.doi.org/10.1016/j.ijnonlinmec.2006.11.002. DOI: 10.1016/j.ijnonlinmec.2006.11.002

[100] J. Merodio, "On the Failure of Ellipticity for Compressible Isotropic Nonlinearly Elastic Materials," *AIP Conference Proceedings,* vol. 1023, pp. 103–106, 2008. DOI: 10.1063/1.2958159

[101] J. Merodio, "On constitutive equations for fiber-reinforced nonlinearly viscoelastic solids," *Mechanics Research Communications,* vol. 33, *(6),* pp. 764–770, 2006. Available: https://dx.doi.org/10.1016/j.mechrescom.2006.03.009. DOI: 10.1016/j.mechrescom.2006.03.009

[102] J. Merodio, "Equilibrium Shocks in a Directionally Reinforced Neo-Hookean Material Under Plane Deformation", ProQuest Dissertations & Theses, 1999

[103] A. Melnikov and J. Merodio, “Stability Analysis of an Inflated, Axially Extended, Residually Stressed Circular Cylindrical Tube,” *Journal of Applied and Computational Mechanics*, vol. 9, *(3)*, pp. 834-847, 2023. Available: https://jacm.scu.ac.ir/article_18023_1f70696b40b51870207c1f496e03e401.pdf. DOI: 10.22055/jacm.2023.42359.3915

[104] P. Mascheroni, R. Penta and J. Merodio, "The impact of vascular volume fraction and compressibility of the interstitial matrix on vascularised poroelastic tissues," *Biomech Model Mechanobiol,* vol. 22, *(6),* pp. 1901–1917, 2023.

Available: https://link.springer.com/article/10.1007/s10237-023-01742-1. DOI: 10.1007/s10237-023-01742-1

[105] M. E. Lindsay and H. C. Dietz, "Lessons on the pathogenesis of aneurysm from heritable conditions," *Nature,* vol. 473, *(7347),* pp. 308–316, 2011. Available: https://link.springer.com/article/10.1038/nature10145. DOI: 10.1038/nature10145

[106] S. Kyriakides and Y. C. Chang, “The initiation and propagation of a localized instability in an inflated elastic tube,” *International Journal of Solids and Structures*, vol. 27, *(9)*, pp. 1085-1111, 1991. DOI: https://doi.org/10.1016/0020-7683(91)90113-T

[107] F. Kassianidis, R. W. Ogden, J. Merodio and T. J. Pence, “Azimuthal shear of a transversely isotropic elastic solid,” *Mathematics and Mechanics of Solids*, vol. 13, *(8)*, pp. 690-724, 2008. DOI: https://doi.org/10.1177/108128650707983

[108] H. Hatze, "The meaning of the term ‘biomechanics’," *Journal of Biomechanics,* vol. 7, *(2),* pp. 189–190, 1974. Available: https://dx.doi.org/10.1016/0021-9290(74)90060-8. DOI: 10.1016/0021-9290(74)90060-8

[109] D. Guinovart-Sanjuán *et al*, "Effective properties of regular elastic laminated shell composite," *Composites. Part B, Engineering,* vol. 87, pp. 12–20, 2016. Available: https://dx.doi.org/10.1016/j.compositesb.2015.09.051. DOI: 10.1016/j.compositesb.2015.09.051

[110] M. E. Hamdaoui, J. Merodio and R. W. Ogden, "Two-phase piecewise homogeneous plane deformations of a fibre-reinforced neo-Hookean material with application to fibre kinking and splitting," *Journal of the Mechanics and Physics of Solids,* vol. 143, pp. 104091, 2020. Available: https://dx.doi.org/10.1016/j.jmps.2020.104091. DOI: 10.1016/j.jmps.2020.104091

[111] M. E. Hamdaoui, J. Merodio and R. W. Ogden, "Deformation induced loss of ellipticity in an anisotropic circular cylindrical tube," *J Eng Math,* vol. 109, *(1),* pp.

31–45, 2018. Available: https://link.springer.com/article/10.1007/s10665-017-9904-z. DOI: 10.1007/s10665-017-9904-z

[112] M. E. Hamdaoui, J. Merodio and R. W. Ogden, "Loss of ellipticity in the combined helical, axial and radial elastic deformations of a fibre-reinforced circular cylindrical tube," *International Journal of Solids and Structures,* vol. 63, pp. 99–108, 2015. Available: https://dx.doi.org/10.1016/j.ijsolstr.2015.02.043. DOI: 10.1016/j.ijsolstr.2015.02.043

[113] M. E. Hamdaoui, J. Merodio, R. W. Ogden and J. Rodríguez, "Finite elastic deformations of transversely isotropic circular cylindrical tubes," *International Journal of Solids and Structures,* vol. 51, *(5),* pp. 1188–1196, 2014. Available: https://dx.doi.org/10.1016/j.ijsolstr.2013.12.019. DOI: 10.1016/j.ijsolstr.2013.12.019

[114] M. E. Hamdaoui and J. Merodio, "Azimuthal shear of doubly fibre-reinforced, non-linearly elastic cylindrical tubes," *J Eng Math,* vol. 95, *(1),* pp. 347–357, 2015. Available: https://link.springer.com/article/10.1007/s10665-014-9729-y. DOI: 10.1007/s10665-014-9729-y

[115] A. Dorfmann, J. Merodio and R. W. Ogden, "Non-smooth solutions in the azimuthal shear of an anisotropic nonlinearly elastic material," *Journal of Engineering Mathematics*, vol. 68, pp. 27-36, August 2009. DOI: https://doi.org/10.1007/s10665-009-9318-7

[116] M. Destrade and J. Merodio, "Compression Instabilities Of Tissues With Localized Strain Softening," *International Journal of Applied Mechanics,* vol. 3, *(1),* pp. 69–83, 2011. Available: http://www.worldscientific.com/doi/abs/10.1142/S1758825111000877. DOI: 10.1142/S1758825111000877

[117] H. Dehghani, I. Noll, R. Penta, A. Menzel and J. Merodio, "The role of microscale solid matrix compressibility on the mechanical behaviour of poroelastic materials," *European Journal of Mechanics - A/Solids,* vol. 83, pp. 103996, 2020. Available: https://dx.doi.org/10.1016/j.euromechsol.2020.103996. DOI: 10.1016/j.euromechsol.2020.103996

[118] O. L. Cruz-González *et al*, "A hierarchical asymptotic homogenization approach for viscoelastic composites," *Mechanics of Advanced Materials and Structures,* vol. 28, *(21),* pp. 2190–2201, 2021. Available: https://www.tandfonline.com/doi/abs/10.1080/15376494.2020.1722872. DOI: 10.1080/15376494.2020.1722872

[119] R. Bustamante and J. Merodio, "On weak formulations and their second variation in nonlinear electroelasticity," *Mechanics Research Communications,* vol. 46, pp. 15–19, 2012. Available: https://dx.doi.org/10.1016/j.mechrescom.2012.08.001. DOI: 10.1016/j.mechrescom.2012.08.001

[120] R. Bustamante and J. Merodio, "Constitutive structure in coupled non-linear electro-elasticity: Invariant descriptions and constitutive restrictions," *International Journal of Non-Linear Mechanics,* vol. 46, *(10),* pp. 1315–1323, 2011. Available: https://dx.doi.org/10.1016/j.ijnonlinmec.2011.06.010. DOI: 10.1016/j.ijnonlinmec.2011.06.010

[121] M. Braun, *Differential Equations and Their Applications.* (3rd ed.) New York, NY: Springer Nature, 2013

[122] H. Asghari, H. Topol, B. Markert and J. Merodio, "Application of the extended Fourier amplitude sensitivity testing (FAST) method to inflated, axial stretched, and residually stressed cylinders," *Appl. Math. Mech. - Engl. Ed,* vol. 44, *(12),* pp. 2139–2162, 2023. Available: https://link.springer.com/article/10.1007/s10483-023-3060-6. DOI: 10.1007/s10483-023-3060-6

[123] M. H. B. M. Shariff, J. Merodio and R. Bustamante, "Nonlinear elastic constitutive relations of residually stressed composites with stiff curved fibres," *Appl. Math. Mech. - Engl. Ed,* vol. 43, *(10),* pp. 1515–1530, 2022. Available: https://link.springer.com/article/10.1007/s10483-022-2910-7. DOI: 10.1007/s10483-022-2910-7

[124] M. H. B. M. Shariff, J. Merodio and R. Bustamante, "A non-second-gradient model for nonlinear elastic bodies with fibre stiffness," *Sci Rep,* vol. 13, *(1),* pp.

6562, 2023. Available: https://link.springer.com/article/10.1038/s41598-023-33670-6. DOI: 10.1038/s41598-023-33670-6

[125] T. Sigaeva, G. Sommer, G. A. Holzapfel and E. S. Di Martino, "Anisotropic residual stresses in arteries," *J. R. Soc. Interface,* vol. 16, *(151),* pp. 20190029, 2019. Available: https://royalsocietypublishing.org/doi/full/10.1098/rsif.2019.0029. DOI: 10.1098/rsif.2019.0029

[126] K. P. Soldatos, M. H. B. M. Shariff and J. Merodio, "On the constitution of polar fiber-reinforced materials, "*Mechanics of Advanced Materials and Structures,* vol. 28, *(21),* pp. 2255–2266, 2021. Available: https://www.tandfonline.com/doi/abs/10.1080/15376494.2020.1729449. DOI: 10.1080/15376494.2020.1729449

[127] H. Topol, M. Al-Chlaihawi, H. Demirkoparan and J. Merodio, "Bulging initiation and propagation in fiber-reinforced swellable Mooney–Rivlin membranes," *J Eng Math,* vol. 128, *(1),* 2021. Available: https://link.springer.com/article/10.1007/s10665-021-10123-5. DOI: 10.1007/s10665-021-10123-5

[128] P. C. Vinh, J. Merodio, T. T. T. Hue and N. T. Nam, "Non-principal Rayleigh waves in deformed transversely isotropic incompressible non-linearly elastic solids," *IMA Journal of Applied Mathematics,* vol. 79, *(5),* pp. 915–928, 2014. DOI: 10.1093/imamat/hxu023

[129] P. C. Vinh and J. Merodio, "Wave velocity formulas to evaluate elastic constants of soft biological tissues," *Journal of Mechanics of Materials and Structures,* vol. 8, *(1),* pp. 51–64, 2013. Available: http://msp.org/jomms/2013/8-1/jomms-v8-n1-p04-s.pdf. DOI: 10.2140/jomms.2013.8.51

[130] P. C. Vinh and J. Merodio, "On acoustoelasticity and the elastic constants of soft biological tissues," *Journal of Mechanics of Materials and Structures,* vol. 8, *(5-7),* pp. 359–367, 2013. Available: http://msp.org/jomms/2013/8-5/jomms-v8-n5-p05-s.pdf. DOI: 10.2140/jomms.2013.8.359

[131] P. C. Vinh, V. T. N. Anh, J. Merodio and L. T. Hue, "Explicit transfer matrices of pre-stressed elastic layers," *International Journal of Non-Linear Mechanics,* vol.

106, pp. 288–296, 2018. Available: https://dx.doi.org/10.1016/j.ijnonlinmec.2018.05.011. DOI: 10.1016/j.ijnonlinmec.2018.05.011

[132] F. Valdés-Ravelo *Et Al*, "Mathematical Modeling Of The Interplay Between Stress And Anisotropic Growth Of Avascular Tumors," *Journal of Mechanics in Medicine and Biology,* vol. 18, *(1),* pp. 1850006, 2018. DOI: 10.1142/S0219519418500069

[133] R. W. Ogden and R. Hill, "Large deformation isotropic elasticity – on the correlation of theory and experiment for incompressible rubberlike solids," *Proceedings of the Royal Society of London. A Mathematical and Physical Sciences,* vol. 326, *(1567),* pp. 565–584, 1997. Available: https://doi.org/10.1098/rspa.1972.0026. DOI: 10.1098/rspa.1972.0026

[134] H. Topol, A. Font, A. Melnikov, J. Lacalle, M. Stoffel and J. Merodio, "On the inflation, bulging/necking bifurcation and post-bifurcation of a cylindrical membrane under limited extensibility of its constituents," *Mathematics and Mechanics of Solids,* pp. 10812865231214262, Available: https://doi.org/10.1177/10812865231214262. DOI: 10.1177/10812865231214262

[135] O. L. Cruz-González *et al*, "An approach for modeling non-ageing linear viscoelastic composites with general periodicity," *Composite Structures,* vol. 223, 2019. DOI: 10.1016/j.compstruct.2019.110927

[136] D. Desena-Galarza*,* H. Dehghani, N. K. Jha, J. Reinoso and J. Merodio, "Computational bifurcation analysis for hyperelastic residually stressed tubes under combined inflation and extension and aneurysms in arterial tissue," *Finite Elements in Analysis and Design,* vol. 197, pp. 103636, 2021. DOI: 10.1016/j.finel.2021.103636

[137] O. C. Zienkiewicz and R. L. Taylor, *The Finite Element Method*, 5th ed., Oxford, UK: Butterworth-Heinemann, 2000

[138] E. C. Sanfeliu, "Numerical Modelling of the Growth and Remodeling Phenomena in Biological Tissues," *Thesis dissertation*, 2016. Available:

https://upcommons.upc.edu/handle/2117/108955. DOI: 10.5821/dissertation-2117-108955

[139] D. Martonová, M. Peirlinck, K. Linka, G. A. Holzapfel, S. Leyendecker, E. Kuhl, "Automated model discovery for human cardiac tissue: Discovering the best model and parameters," *Comp. Meth. In App. Mech. And Eng.*, vol. 428, pp. 117078, 2024. DOI: 10.1101/2024.02.27.582427

[140] Y. C. Fung, K. Fronek and P. Patitucci, "Pseudoelasticity of arteries and the choice of its mathematical expression," *Heart and circulatory physiology*, vol. 237, *(5)*, pp. 620-631, 1979. DOI: https://doi.org/10.1152/ajpheart.1979.237.5.H620

[141] C. Liu, Y. Du, K. Li, Z. Han and C. Lü, "Growth and morphogenesis of an everted tubular biological tissue," *Proc. R. Soc. A.,* vol. 480, *(2283),* 2024. DOI: 10.1098/rspa.2023.0816

[142] R. Martinez, C. A. Fierro, P. K. Shireman and H. C. Han, "Mechanical Buckling of Veins Under Internal Pressure," *Ann Biomed Eng,* vol. 38, *(4),* pp. 1345, 2011. DOI: 10.1007/s10439-010-9929-1

[143] S. Song and H. Jin, "Identifying Constitutive Parameters for Complex Hyperelastic Materials using Physics-Informed Neural Networks," *Soft Matter*, vol. 20, pp. 5915-5926, 2023. DOI: https://doi.org/10.1039/D4SM00001C

[144] G. A. Holzapfel, G. Sommer, C. T. Gasser and P. Regitnig, "Determination of layer-specific mechanical properties of human coronary arteries with nonatherosclerotic intimal thickening and related constitutive modeling," *Heart and Circulatory Physiology*, vol. 289, *(5)*, pp. 2048-2058, 2005. Available: https://journals.physiology.org/doi/full/10.1152/ajpheart.00934.2004?checkFormatAccess=true. DOI: https://doi.org/10.1152/ajpheart.00934.2004

[145] T. Jin and I. Stanciulescu, "Computational modeling of the arterial wall based on layer-specific histological data," *Biomechanics and Modeling in Mechanobiol.,* vol. 15, *(6),* pp. 1479-1494, 2016. DOI: 10.1007/s10237-016-0778-1

[146] A. Van Der Horst, C. N. Van Den Broek, F. N. Van De Vosse and M. C. M. Rutten, "The fiber orientation in the coronary arterial wall at physiological loading

evaluated with a two-fiber constitutive model," *Biomechanics and Modeling in Mechanobiol.,* vol. 11, *(3-4),* pp. 533-542, 2011. Available: https://link.springer.com/article/10.1007/s10237-011-0331-1. DOI: 10.1007/s10237-011-0331-1

[147] M. J. Uddin, M. Z. I. Bangalee and M. Ferdows, "Numerical computation of pulsatile hemodynamics and diagnostic concern of coronary bifurcated artery flow for Newtonian and non-Newtonian fluid," *Heliyon,* vol. 9, *(7),* 2023. DOI: 10.1016/j.heliyon.2023.e17533

[148] M. Destrade, “Incremental Equations for Soft Fibrous Materials,” in *Nonlinear Mechanics of Soft Fibrous Materials*, L. Dorfmann and R. W. Ogden (eds), Vienna: Springer, 2015, ch. 5, pp. 233-267

[149] J. Jagos, D. Schwarz, S. Polzer and J. Bursa, "Effect of aortic bifurcation geometry on pressure and peak wall stress in abdominal aorta: Fluid-structure interaction study," *Medical Engineering & Physics,* vol. 118, 2023. DOI: 10.1016/j.medengphy.2023.104014

[150] P. W. Alford, J. D. Humphrey and L. A. Taber, "Growth and remodeling in a thick-walled artery model: effects of spatial variations in wall constituents," *Biomechanics and Modeling Mechanobiol.,* vol. 7, *(4),* pp. 245-262, 2008. DOI: 10.1007/s10237-007-0101-2

[151] G. A. Holzapfel, “Determination of material models for arterial walls from uniaxial extension tests and histological structure," *Journal of Theoretical Biology,* vol. 238, *(2),* pp. 290-302, 2006. DOI: 10.1016/j.jtbi.2005.05.006

[152] G. A. Holzapfel, T. C. Gasser and R. W. Ogden, "Comparison of a Multi-Layer Structural Model for Arterial Walls With a Fung-Type Model, and Issues of Material Stability," *Journal of Biomechanical Engineering,* vol. 126, *(2),* pp. 264, 2004. DOI: 10.1115/1.1695572

[153] G. A. Holzapfel, G. Sommer and P. Regitnig, "Anisotropic Mechanical Properties of Tissue Components in Human Atherosclerotic Plaques," *Journal of Biomechanical Engineering,* vol. 126, *(5),* pp. 657-665, 2004. DOI: 10.1115/1.1800557

[154] G. A. Holzapfel, T. C. Gasser and M. Stadler, "A structural model for the viscoelastic behavior of arterial walls: Continuum formulation and finite element analysis," *European Journal of Mechanics – A/Solids*, Vol. 21, *(3)*, pp. 441-463, 2002. DOI: https://doi.org/10.1016/S0997-7538(01)01206-2

[155] S. Moradalizadeh, H. Topol, H. Demirkoparan, A. Melnikov, B. Markert and J. Merodio, "Remarks on bifurcation of an inflated and extended swellable isotropic tube," *Mathematics and Mechanics of Solids*, vol. 29, *(3)*, pp. 474-493, 2024. DOI: https://doi.org/10.1177/10812865231190845

[156] M.H.B.M. Shariff, R. Bustamante and J. Merodio, "A generalized strain model for spectral rate-dependent constitutive equation of transversely isotropic electro-viscoelastic solids," *J. Mech. Phys. Solids*, vol. 192, 2024. DOI: https://doi.org/10.1016/j.jmps.2024.105838

[157] H. Asghari, L. Miller, R. Penta and J. Merodio, "On an isotropic porous solid cylinder: the analytical solution and sensitivity analysis of the pressure," *Applied Mathematics and Mechanics*, vol. 45, *(9)*, pp. 1499-1522, 2024. DOI: https://doi.org/10.1007/s10483-024-3144-7

[158] H. Asghari, H. Topol, J. Lacalle and J. Merodio, "Sensitivity analysis of fibrous thick-walled tubes with mechano-sensitive remodeling fibers in homeostasis," *Acta Mechanica*, vol. 235, *(9)*, pp. 5727-5745, 2024. DOI: https://doi.org/10.1007/s00707-024-04017-7

[159] M. J. Al-Chlaihawi, D. Desena-Galarza, H. Topol and J. Merodio, "Computational modeling of a residually stressed thick-walled cylinder under the combined action of axial extension and inflation," submitted, 2024.

[160] J. Merodio and A. Rosato, *General Overview of Continuum Mechanics*, vol. I ed., EOLSS Publications, 2011

[161] D. Balzani, P. Neff, J. Schöder and G. A. Holzapfel, "A polyconvex framework for soft biological tissues. Adjustment to experimental data," *Int. J. Solids Str.*, vol. 43, *(20)*, pp. 6052-6070, 2006. DOI: https://doi.org/10.1016/j.ijsolstr.2005.07.048

[162] R. W. Ogden, "Incremental elastic motions superimposed on a finite deformation in the presence of an electromagnetic field," *Int. J. Non-Linear Mech.*, vol. 44, *(5)*, pp. 570-580, 2009. DOI: https://doi.org/10.1016/j.ijnonlinmec.2008.11.017

[163] R. W. Ogden and P. Chadwick, "On the deformation of solid and tubular cylinders of incompressible isotropic elastic material," *J. Mech. And Phys. Solids*, vol. 20, *(2)*, pp. 77-90, 1972. DOI: https://doi.org/10.1016/0022-5096(72)90032-4

[164] M. Zidi and M. Cheref, "Finite deformations of a hyperelastic, compressible and fibre reinforced tube," *European Journal of Mechanics – A/Solids*, vol. 21, *(6)*, pp. 971-980, 2002. DOI: https://doi.org/10.1016/S0997-7538(02)01239-1

[165] M. H. B. M. Shariff, R. Bustamante and J. Merodio, "On the spectral analysis of residual stress in finite elasticity," *IMA Journal of Applied Mathematics*, vol. 82, *(3)*, pp. 656-680, 2017. DOI: 10.1093/imamat/hxx007

[166] M. H. B. M. Shariff, R. Bustamante and J. Merodio, "Rate type constitutive equations for fiber reinforced nonlinearly vicoelastic solids using spectral invariants," *Mechanics Research Communications*, vol. 84, pp. 60-64, 2017. DOI: https://doi.org/10.1016/j.mechrescom.2017.06.010

[167] M. H. B. M. Shariff and J. Merodio, "Residually stressed two fibre solids: A spectral approach," *International Journal of Engineering Science*, vol. 148, pp. 103205, 2020. DOI: https://doi.org/10.1016/j.ijengsci.2019.103205

[168] M. H. B. M. Shariff, R. Bustamante and J. Merodio, "A nonlinear spectral rate-dependent constitutive equation for electro-viscoelastic solids," *Zeitschrift für angewandte Mathematik und Physik*, vol. 71, *(126)*, 2020. DOI: https://doi.org/10.1007/s00033-020-01353-1

[169] R. Rodríguez-Ramos *et al*, "Multiscale Homogenization for Linear Mechanics", in *Constitutive Modelling of Solid Continua*, J. Merodio and R. W. Ogden (eds.), vol. 262. Springer, Cham. DOI: https://doi.org/10.1007/978-3-030-31547-4_12

[170] R. Penta, A. Ramírez-Torres, J. Merodio and R. Rodríguez-Ramos, “Effective balance equations for elastic composites subject to inhomogeneous potentials,” *Continuum Mechanics and Thermodynamics*, vol. 30, pp. 145-163, 2018. DOI: https://doi.org/10.1007/s00161-017-0590-x

[171] M. E. Hamdaoui and J. Merodio, “A note on finite elastic deformations of fiber-reinforced non-linearly elastic tubes,” *Arch. Mech.*, vol. 67, *(1)*, pp. 95-109, 2015

Annex A

Some Python and MATLAB scripts have been coded and used to extract and manipulate the numerical results to produce adequate and specifical plots shown along this document. As too many Abaqus simulations have been carried out and from each simulation a big amount of data needs to be extracted, Python scripts were coded to reduce the post-processing time. Some of this coding that have been produced, for example, regarding the extraction of the LPF curves and the azimuthal and axial stresses from the Abaqus output databases for generating plots such as Figure 4.17, Figure 5.9 and Figure 5.15 is presented. Also, corresponding MATLAB scripts taking as inputs the data extracted by means of the Python scripts are shown. Is by the MATLAB code that the extracted data is manipulated and plotted. The aim objective is to illustrate the capabilities of the mixing of Abaqus with programming languages as Python and MATLAB environment. As too many code lines have been developed, just a few will be presented for simplicity.

Illustration of Python Coding for Azimuthal and Axial Stress Components Extraction (part of the coding)

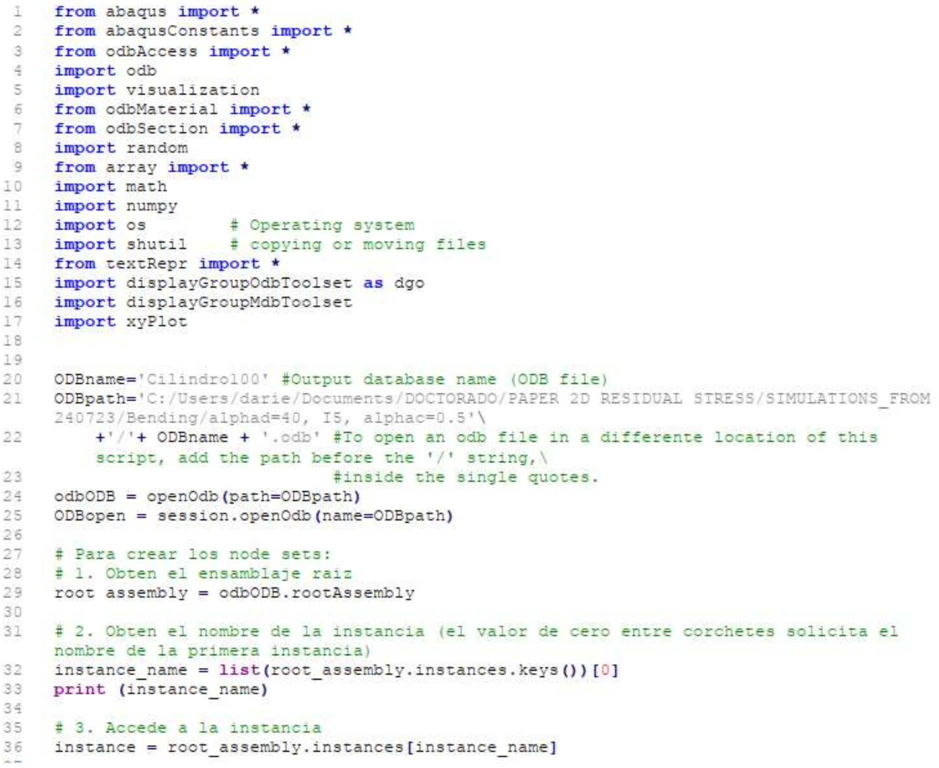

```python
from abaqus import *
from abaqusConstants import *
from odbAccess import *
import odb
import visualization
from odbMaterial import *
from odbSection import *
import random
from array import *
import math
import numpy
import os         # Operating system
import shutil     # copying or moving files
from textRepr import *
import displayGroupOdbToolset as dgo
import displayGroupMdbToolset
import xyPlot


ODBname='Cilindro100' #Output database name (ODB file)
ODBpath='C:/Users/darie/Documents/DOCTORADO/PAPER 2D RESIDUAL STRESS/SIMULATIONS_FROM
240723/Bending/alphad=40, I5, alphac=0.5'\
    +'/'+ ODBname + '.odb' #To open an odb file in a differente location of this
    script, add the path before the '/' string,\
                       #inside the single quotes.
odbODB = openOdb(path=ODBpath)
ODBopen = session.openOdb(name=ODBpath)

# Para crear los node sets:
# 1. Obten el ensamblaje raiz
root assembly = odbODB.rootAssembly

# 2. Obten el nombre de la instancia (el valor de cero entre corchetes solicita el
nombre de la primera instancia)
instance_name = list(root_assembly.instances.keys())[0]
print (instance_name)

# 3. Accede a la instancia
instance = root_assembly.instances[instance_name]
```

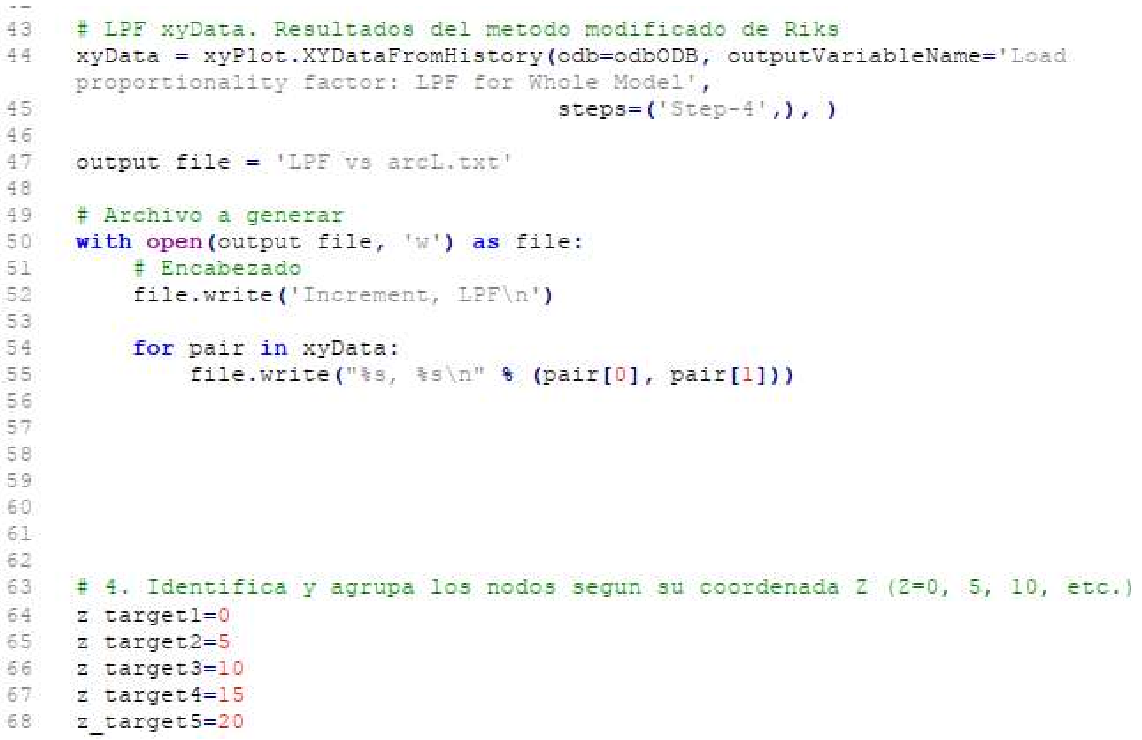

```python
# LPF xyData. Resultados del metodo modificado de Riks
xyData = xyPlot.XYDataFromHistory(odb=odbODB, outputVariableName='Load
proportionality factor: LPF for Whole Model',
                                   steps=('Step-4',), )

output file = 'LPF vs arcL.txt'

# Archivo a generar
with open(output file, 'w') as file:
    # Encabezado
    file.write('Increment, LPF\n')

    for pair in xyData:
        file.write("%s, %s\n" % (pair[0], pair[1]))







# 4. Identifica y agrupa los nodos segun su coordenada Z (Z=0, 5, 10, etc.)
z target1=0
z target2=5
z target3=10
z target4=15
z_target5=20
```

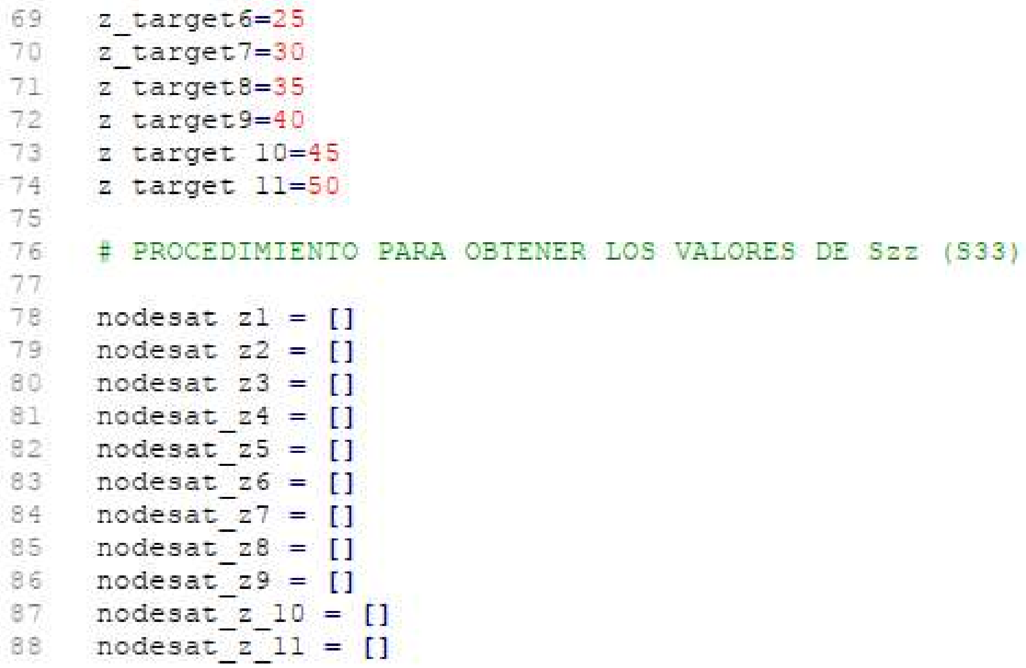

```
z_target6=25
z_target7=30
z_target8=35
z_target9=40
z_target_10=45
z_target_11=50

# PROCEDIMIENTO PARA OBTENER LOS VALORES DE Szz (S33)

nodesat_z1 = []
nodesat_z2 = []
nodesat_z3 = []
nodesat_z4 = []
nodesat_z5 = []
nodesat_z6 = []
nodesat_z7 = []
nodesat_z8 = []
nodesat_z9 = []
nodesat_z_10 = []
nodesat_z_11 = []
```

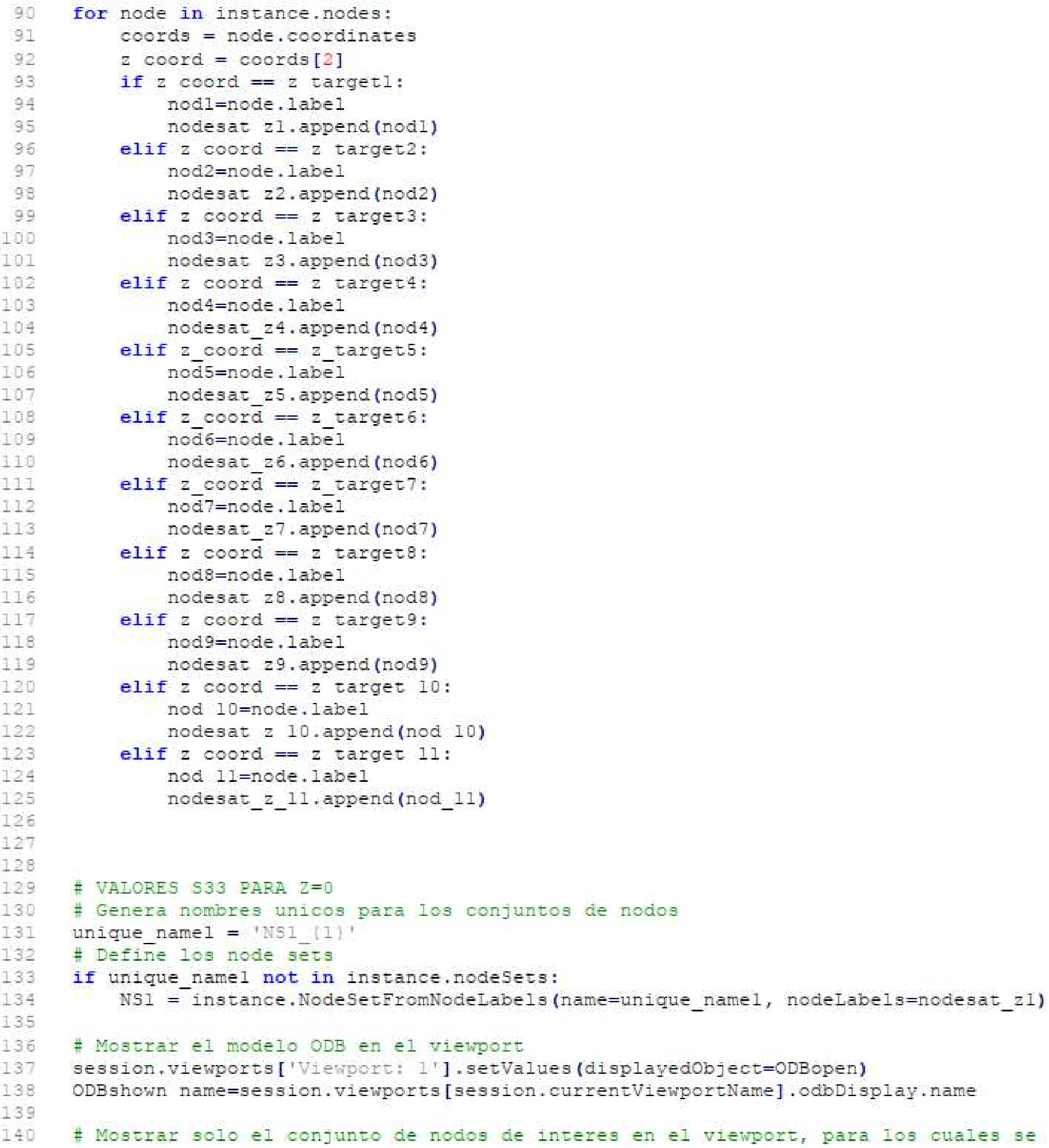

```
for node in instance.nodes:
    coords = node.coordinates
    z_coord = coords[2]
    if z_coord == z_target1:
        nod1=node.label
        nodesat_z1.append(nod1)
    elif z_coord == z_target2:
        nod2=node.label
        nodesat_z2.append(nod2)
    elif z_coord == z_target3:
        nod3=node.label
        nodesat_z3.append(nod3)
    elif z_coord == z_target4:
        nod4=node.label
        nodesat_z4.append(nod4)
    elif z_coord == z_target5:
        nod5=node.label
        nodesat_z5.append(nod5)
    elif z_coord == z_target6:
        nod6=node.label
        nodesat_z6.append(nod6)
    elif z_coord == z_target7:
        nod7=node.label
        nodesat_z7.append(nod7)
    elif z_coord == z_target8:
        nod8=node.label
        nodesat_z8.append(nod8)
    elif z_coord == z_target9:
        nod9=node.label
        nodesat_z9.append(nod9)
    elif z_coord == z_target_10:
        nod_10=node.label
        nodesat_z_10.append(nod_10)
    elif z_coord == z_target_11:
        nod_11=node.label
        nodesat_z_11.append(nod_11)



# VALORES S33 PARA Z=0
# Genera nombres unicos para los conjuntos de nodos
unique_name1 = 'NS1_{1}'
# Define los node sets
if unique_name1 not in instance.nodeSets:
    NS1 = instance.NodeSetFromNodeLabels(name=unique_name1, nodeLabels=nodesat_z1)

# Mostrar el modelo ODB en el viewport
session.viewports['Viewport: 1'].setValues(displayedObject=ODBopen)
ODBshown_name=session.viewports[session.currentViewportName].odbDisplay.name

# Mostrar solo el conjunto de nodos de interes en el viewport, para los cuales se
```

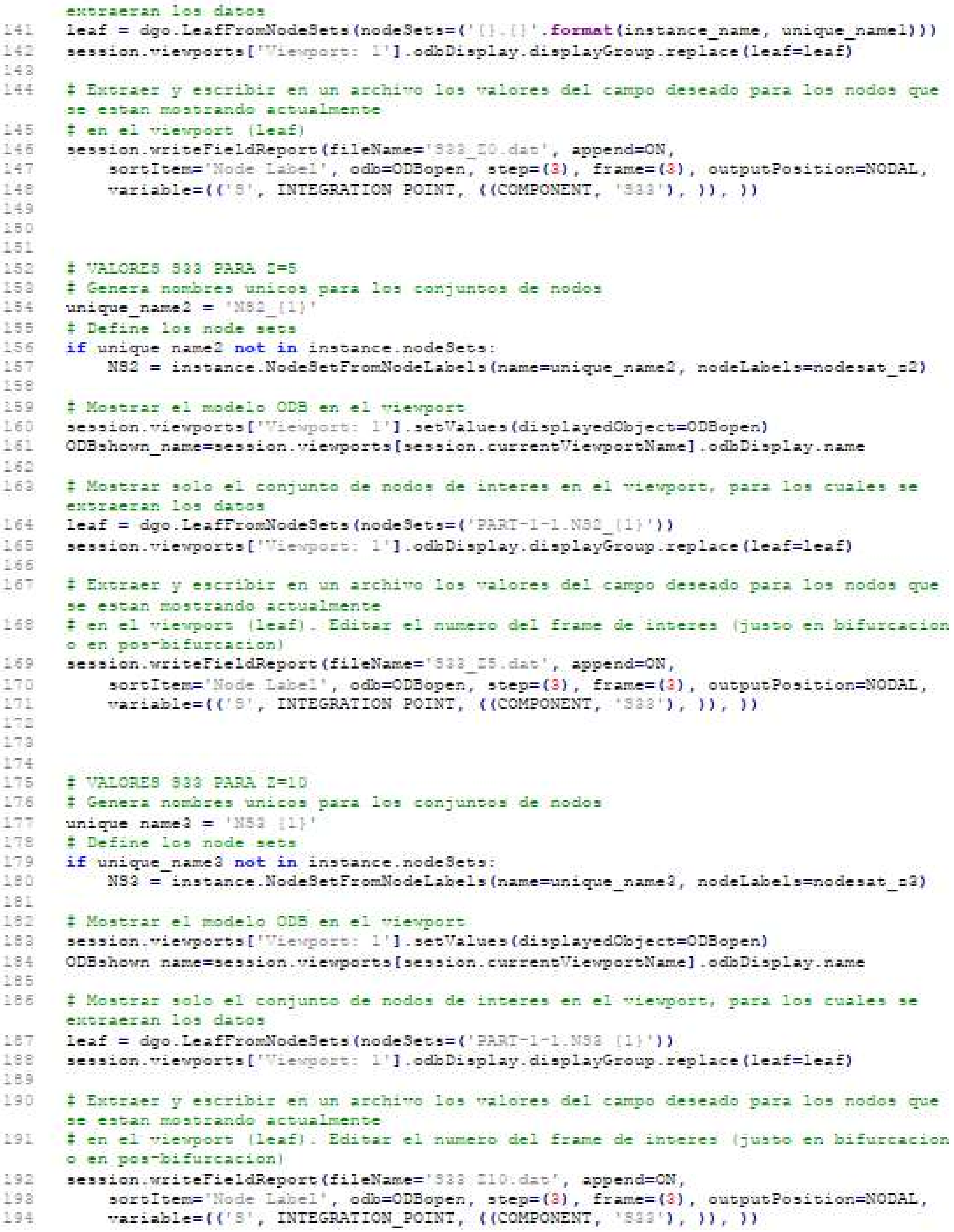

```
extraeran los datos
leaf = dgo.LeafFromNodeSets(nodeSets=('{}.{}'.format(instance_name, unique_name1)))
session.viewports['Viewport: 1'].odbDisplay.displayGroup.replace(leaf=leaf)

# Extraer y escribir en un archivo los valores del campo deseado para los nodos que
se estan mostrando actualmente
# en el viewport (leaf)
session.writeFieldReport(fileName='S33_Z0.dat', append=ON,
    sortItem='Node Label', odb=ODBopen, step=(3), frame=(3), outputPosition=NODAL,
    variable=(('S', INTEGRATION_POINT, ((COMPONENT, 'S33'), )), ))



# VALORES S33 PARA Z=5
# Genera nombres unicos para los conjuntos de nodos
unique_name2 = 'NS2_{1}'
# Define los node sets
if unique_name2 not in instance.nodeSets:
    NS2 = instance.NodeSetFromNodeLabels(name=unique_name2, nodeLabels=nodesat_z2)

# Mostrar el modelo ODB en el viewport
session.viewports['Viewport: 1'].setValues(displayedObject=ODBopen)
ODBshown_name=session.viewports[session.currentViewportName].odbDisplay.name

# Mostrar solo el conjunto de nodos de interes en el viewport, para los cuales se
extraeran los datos
leaf = dgo.LeafFromNodeSets(nodeSets=('PART-1-1.NS2_{1}'))
session.viewports['Viewport: 1'].odbDisplay.displayGroup.replace(leaf=leaf)

# Extraer y escribir en un archivo los valores del campo deseado para los nodos que
se estan mostrando actualmente
# en el viewport (leaf). Editar el numero del frame de interes (justo en bifurcacion
o en pos-bifurcacion)
session.writeFieldReport(fileName='S33_Z5.dat', append=ON,
    sortItem='Node Label', odb=ODBopen, step=(3), frame=(3), outputPosition=NODAL,
    variable=(('S', INTEGRATION_POINT, ((COMPONENT, 'S33'), )), ))



# VALORES S33 PARA Z=10
# Genera nombres unicos para los conjuntos de nodos
unique_name3 = 'NS3_{1}'
# Define los node sets
if unique_name3 not in instance.nodeSets:
    NS3 = instance.NodeSetFromNodeLabels(name=unique_name3, nodeLabels=nodesat_z3)

# Mostrar el modelo ODB en el viewport
session.viewports['Viewport: 1'].setValues(displayedObject=ODBopen)
ODBshown_name=session.viewports[session.currentViewportName].odbDisplay.name

# Mostrar solo el conjunto de nodos de interes en el viewport, para los cuales se
extraeran los datos
leaf = dgo.LeafFromNodeSets(nodeSets=('PART-1-1.NS3_{1}'))
session.viewports['Viewport: 1'].odbDisplay.displayGroup.replace(leaf=leaf)

# Extraer y escribir en un archivo los valores del campo deseado para los nodos que
se estan mostrando actualmente
# en el viewport (leaf). Editar el numero del frame de interes (justo en bifurcacion
o en pos-bifurcacion)
session.writeFieldReport(fileName='S33_Z10.dat', append=ON,
    sortItem='Node Label', odb=ODBopen, step=(3), frame=(3), outputPosition=NODAL,
    variable=(('S', INTEGRATION_POINT, ((COMPONENT, 'S33'), )), ))
```

Illustration of MATLAB Coding For Plots Generation

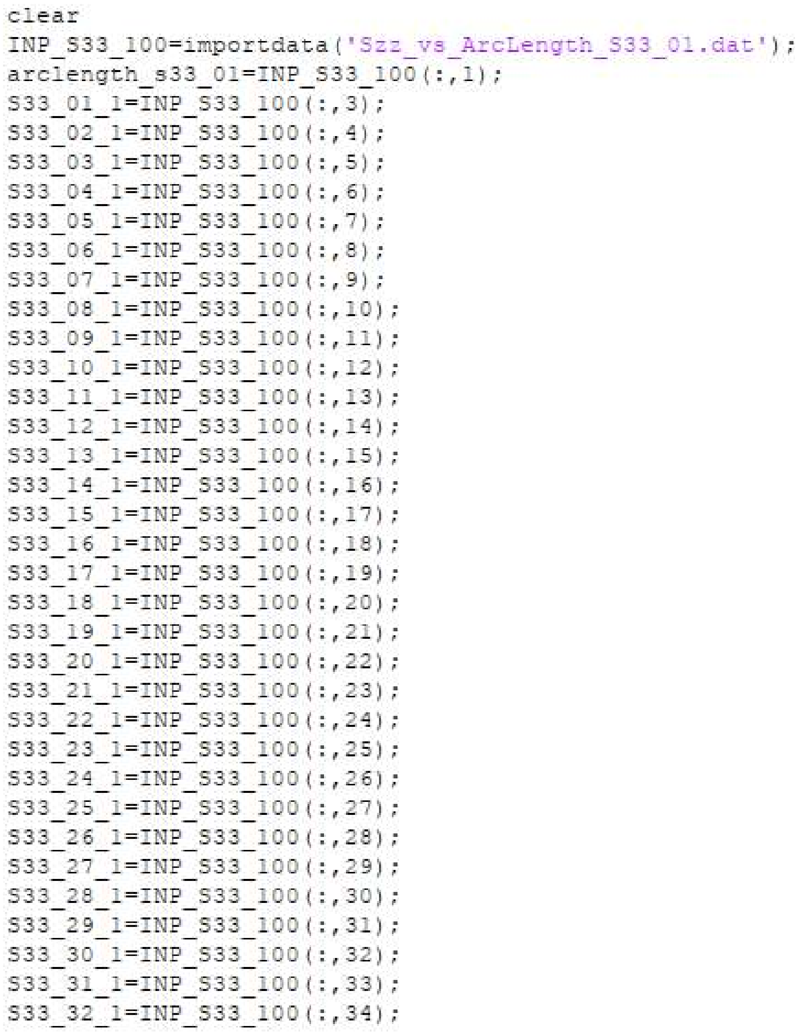

```
clear
INP_S33_100=importdata('Szz_vs_ArcLength_S33_01.dat');
arclength_s33_01=INP_S33_100(:,1);
S33_01_1=INP_S33_100(:,3);
S33_02_1=INP_S33_100(:,4);
S33_03_1=INP_S33_100(:,5);
S33_04_1=INP_S33_100(:,6);
S33_05_1=INP_S33_100(:,7);
S33_06_1=INP_S33_100(:,8);
S33_07_1=INP_S33_100(:,9);
S33_08_1=INP_S33_100(:,10);
S33_09_1=INP_S33_100(:,11);
S33_10_1=INP_S33_100(:,12);
S33_11_1=INP_S33_100(:,13);
S33_12_1=INP_S33_100(:,14);
S33_13_1=INP_S33_100(:,15);
S33_14_1=INP_S33_100(:,16);
S33_15_1=INP_S33_100(:,17);
S33_16_1=INP_S33_100(:,18);
S33_17_1=INP_S33_100(:,19);
S33_18_1=INP_S33_100(:,20);
S33_19_1=INP_S33_100(:,21);
S33_20_1=INP_S33_100(:,22);
S33_21_1=INP_S33_100(:,23);
S33_22_1=INP_S33_100(:,24);
S33_23_1=INP_S33_100(:,25);
S33_24_1=INP_S33_100(:,26);
S33_25_1=INP_S33_100(:,27);
S33_26_1=INP_S33_100(:,28);
S33_27_1=INP_S33_100(:,29);
S33_28_1=INP_S33_100(:,30);
S33_29_1=INP_S33_100(:,31);
S33_30_1=INP_S33_100(:,32);
S33_31_1=INP_S33_100(:,33);
S33_32_1=INP_S33_100(:,34);
```

1

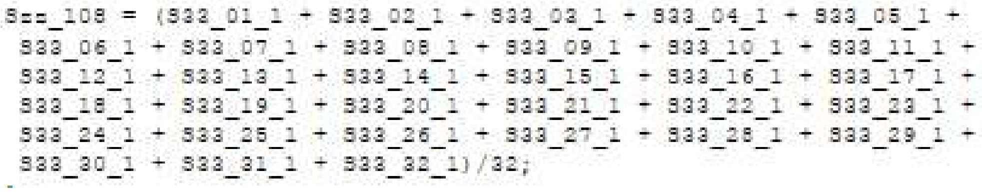

```
Szz_108 = (S33_01_1 + S33_02_1 + S33_03_1 + S33_04_1 + S33_05_1 +
 S33_06_1 + S33_07_1 + S33_08_1 + S33_09_1 + S33_10_1 + S33_11_1 +
 S33_12_1 + S33_13_1 + S33_14_1 + S33_15_1 + S33_16_1 + S33_17_1 +
 S33_18_1 + S33_19_1 + S33_20_1 + S33_21_1 + S33_22_1 + S33_23_1 +
 S33_24_1 + S33_25_1 + S33_26_1 + S33_27_1 + S33_28_1 + S33_29_1 +
 S33_30_1 + S33_31_1 + S33_32_1)/32;
```

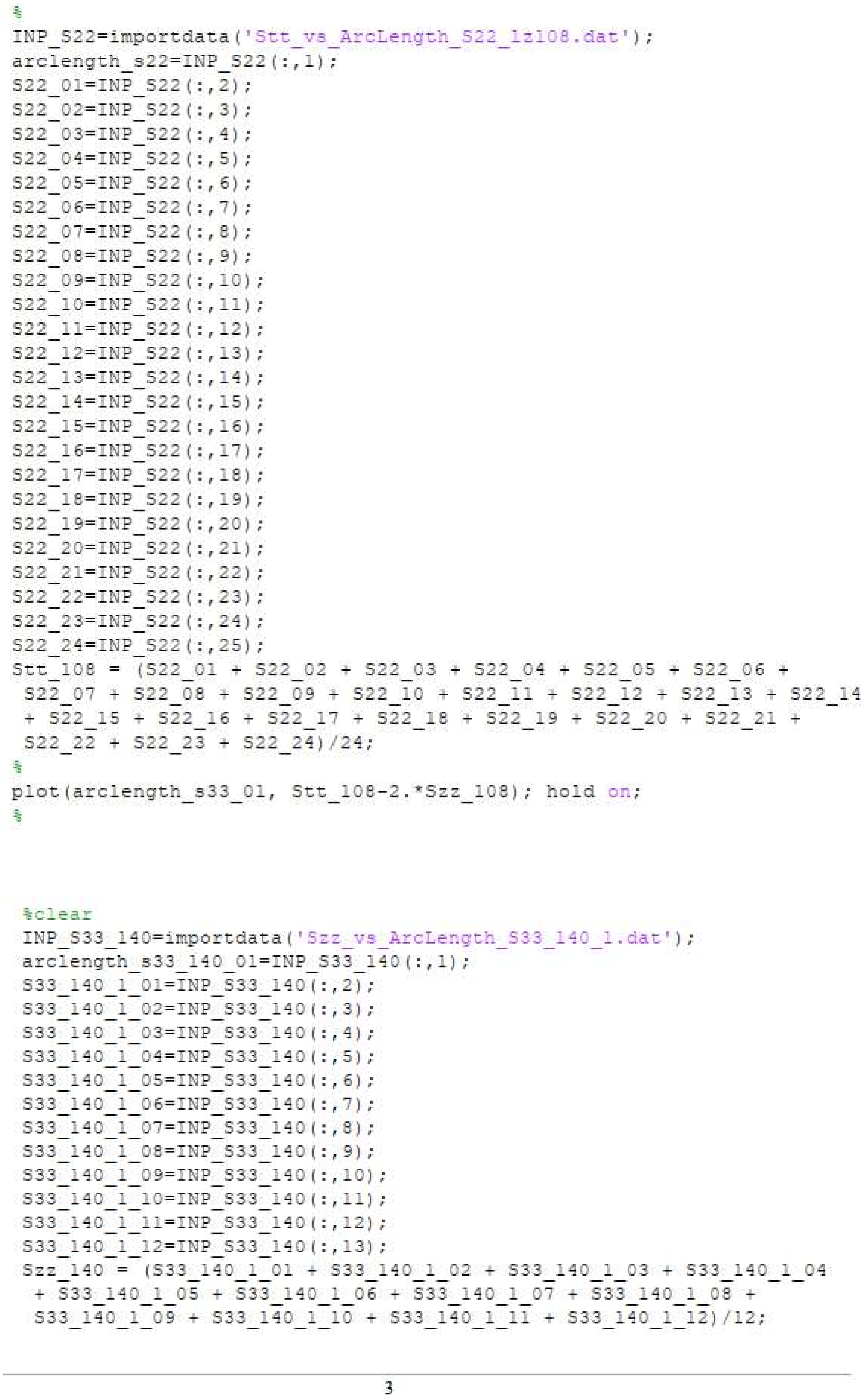

```
%
INP_S22=importdata('Stt_vs_ArcLength_S22_lz108.dat');
arclength_s22=INP_S22(:,1);
S22_01=INP_S22(:,2);
S22_02=INP_S22(:,3);
S22_03=INP_S22(:,4);
S22_04=INP_S22(:,5);
S22_05=INP_S22(:,6);
S22_06=INP_S22(:,7);
S22_07=INP_S22(:,8);
S22_08=INP_S22(:,9);
S22_09=INP_S22(:,10);
S22_10=INP_S22(:,11);
S22_11=INP_S22(:,12);
S22_12=INP_S22(:,13);
S22_13=INP_S22(:,14);
S22_14=INP_S22(:,15);
S22_15=INP_S22(:,16);
S22_16=INP_S22(:,17);
S22_17=INP_S22(:,18);
S22_18=INP_S22(:,19);
S22_19=INP_S22(:,20);
S22_20=INP_S22(:,21);
S22_21=INP_S22(:,22);
S22_22=INP_S22(:,23);
S22_23=INP_S22(:,24);
S22_24=INP_S22(:,25);
Stt_108 = (S22_01 + S22_02 + S22_03 + S22_04 + S22_05 + S22_06 +
 S22_07 + S22_08 + S22_09 + S22_10 + S22_11 + S22_12 + S22_13 + S22_14
 + S22_15 + S22_16 + S22_17 + S22_18 + S22_19 + S22_20 + S22_21 +
 S22_22 + S22_23 + S22_24)/24;
%
plot(arclength_s33_01, Stt_108-2.*Szz_108); hold on;
%



 %clear
 INP_S33_140=importdata('Szz_vs_ArcLength_S33_140_1.dat');
 arclength_s33_140_01=INP_S33_140(:,1);
 S33_140_1_01=INP_S33_140(:,2);
 S33_140_1_02=INP_S33_140(:,3);
 S33_140_1_03=INP_S33_140(:,4);
 S33_140_1_04=INP_S33_140(:,5);
 S33_140_1_05=INP_S33_140(:,6);
 S33_140_1_06=INP_S33_140(:,7);
 S33_140_1_07=INP_S33_140(:,8);
 S33_140_1_08=INP_S33_140(:,9);
 S33_140_1_09=INP_S33_140(:,10);
 S33_140_1_10=INP_S33_140(:,11);
 S33_140_1_11=INP_S33_140(:,12);
 S33_140_1_12=INP_S33_140(:,13);
 Szz_140 = (S33_140_1_01 + S33_140_1_02 + S33_140_1_03 + S33_140_1_04
  + S33_140_1_05 + S33_140_1_06 + S33_140_1_07 + S33_140_1_08 +
  S33_140_1_09 + S33_140_1_10 + S33_140_1_11 + S33_140_1_12)/12;
```

3

```
%
INP_S22_140=importdata('Stt_vs_ArcLength_S22_140.dat');
arclength_s22_140=INP_S22_140(:,1);
S22_140_01=INP_S22_140(:,2);
S22_140_02=INP_S22_140(:,3);
S22_140_03=INP_S22_140(:,4);
S22_140_04=INP_S22_140(:,5);
S22_140_05=INP_S22_140(:,6);
S22_140_06=INP_S22_140(:,7);
S22_140_07=INP_S22_140(:,8);
S22_140_08=INP_S22_140(:,9);
S22_140_09=INP_S22_140(:,10);
S22_140_10=INP_S22_140(:,11);
S22_140_11=INP_S22_140(:,12);
S22_140_12=INP_S22_140(:,13);
S22_140 = (S22_140_01 + S22_140_02 + S22_140_03 + S22_140_04 +
 S22_140_05 + S22_140_06 + S22_140_07 + S22_140_08 + S22_140_09 +
 S22_140_10 + S22_140_11 + S22_140_12)/12;
%
INP_S11_140=importdata('Stt_vs_ArcLength_S11_140.dat');
arclength_s11_140=INP_S11_140(:,1);
S11_140_01=INP_S11_140(:,2);
S11_140_02=INP_S11_140(:,3);
S11_140_03=INP_S11_140(:,4);
S11_140_04=INP_S11_140(:,5);
S11_140_05=INP_S11_140(:,6);
S11_140_06=INP_S11_140(:,7);
S11_140_07=INP_S11_140(:,8);
S11_140_08=INP_S11_140(:,9);
S11_140_09=INP_S11_140(:,10);
S11_140_10=INP_S11_140(:,11);
S11_140_11=INP_S11_140(:,12);
S11_140_12=INP_S11_140(:,13);
S11_140 = (S11_140_01 + S11_140_02 + S11_140_03 + S11_140_04 +
 S11_140_05 + S11_140_06 + S11_140_07 + S11_140_08 + S11_140_09 +
 S11_140_10 + S11_140_11 + S11_140_12)/12;
%
Stt_140 = (S11_140 + S22_140)/2;
%
plot(arclength_s11_140, Stt_140-2.*Szz_140,'--r'); legend('Model with
 \lambda_z=1.08','Model with \lambda_z=1.40');
xlabel('Arc Length'); ylabel('\sigma_{\theta\theta} - 2\sigma_{zz}');
 axis([0 0.5 -4.5 5]);
```

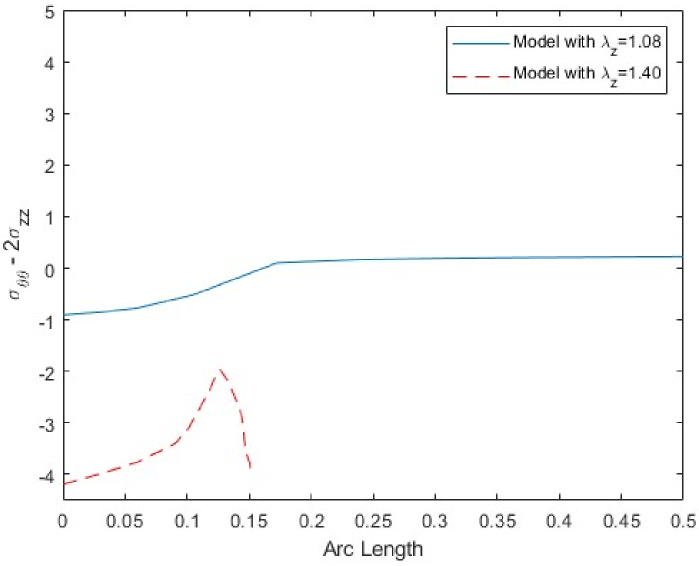

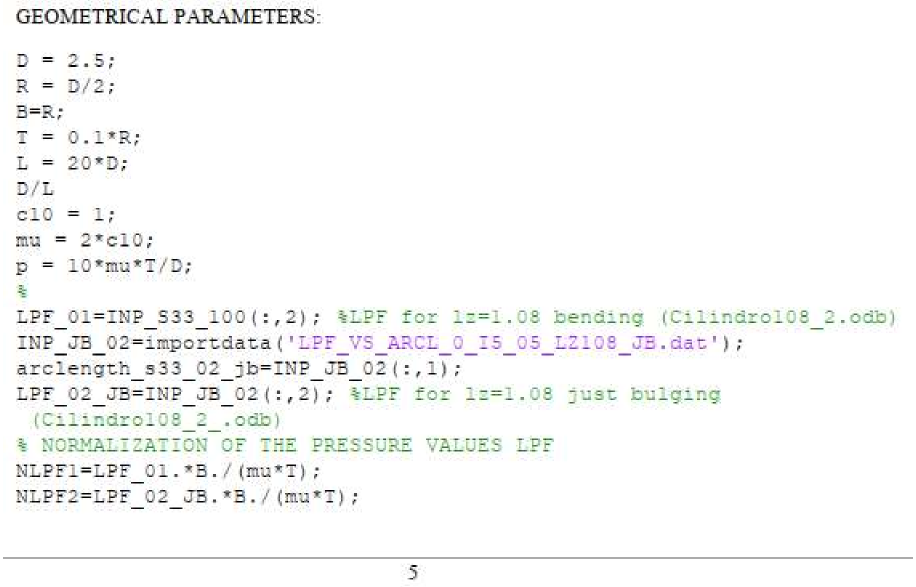

GEOMETRICAL PARAMETERS:

```
D = 2.5;
R = D/2;
B=R;
T = 0.1*R;
L = 20*D;
D/L
c10 = 1;
mu = 2*c10;
p = 10*mu*T/D;
%
LPF_01=INP_S33_100(:,2); %LPF for lz=1.08 bending (Cilindro108_2.odb)
INP_JB_02=importdata('LPF_VS_ARCL_0_I5_05_LZ108_JB.dat');
arclength_s33_02_jb=INP_JB_02(:,1);
LPF_02_JB=INP_JB_02(:,2); %LPF for lz=1.08 just bulging
 (Cilindro108_2_.odb)
% NORMALIZATION OF THE PRESSURE VALUES LPF
NLPF1=LPF_01.*B./(mu*T);
NLPF2=LPF_02_JB.*B./(mu*T);
```

5

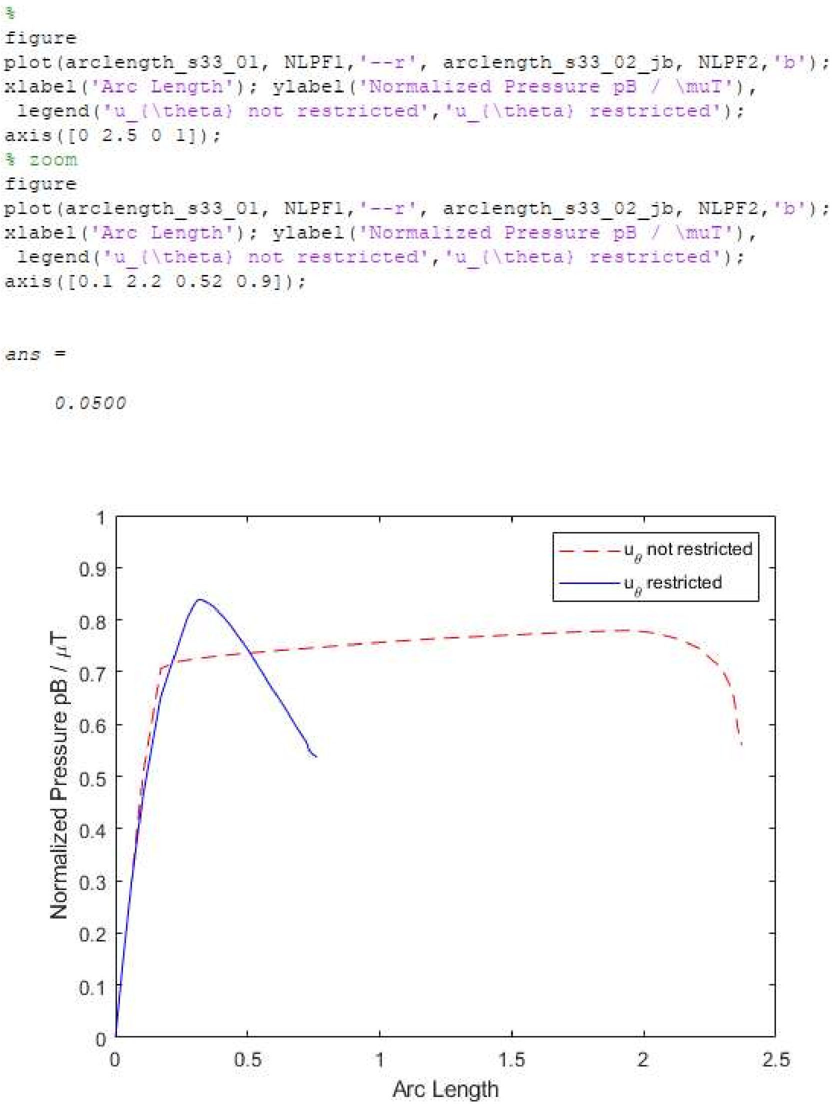

```
%
figure
plot(arclength_s33_01, NLPF1,'--r', arclength_s33_02_jb, NLPF2,'b');
xlabel('Arc Length'); ylabel('Normalized Pressure pB / \muT'),
 legend('u_{\theta} not restricted','u_{\theta} restricted');
axis([0 2.5 0 1]);
% zoom
figure
plot(arclength_s33_01, NLPF1,'--r', arclength_s33_02_jb, NLPF2,'b');
xlabel('Arc Length'); ylabel('Normalized Pressure pB / \muT'),
 legend('u_{\theta} not restricted','u_{\theta} restricted');
axis([0.1 2.2 0.52 0.9]);
```

```
ans =

    0.0500
```